Solar Power System for 3D Printing on Lunar Surface for In-Situ Resource Utilization

By

Rohit Prashant Gaikwad

A thesis submitted to the Faculty of Graduate and Postdoctoral Affairs in partial fulfillment of the requirements for the degree of

Master of Applied Science

in

Mechanical Engineering

Carleton University
Ottawa, Ontario

Abstract

This thesis aims to study the development of a 3D printing system that will utilize solar radiation to heat and melt printing materials on the lunar surface as part of a lunar in-situ resource utilization infrastructure. A Fresnel lens is employed to concentrate solar radiation onto an optical waveguide system. Electronic components, such as Arduino and RepRap Arduino Mega Polulu Shield, are used to control the 3D printing machine. The unique characteristics of optical fibers are examined, focusing on the principles of total internal reflection and core-cladding boundary. This research contributes to the overall understanding of in-situ resource utilization (ISRU) on the lunar surface.

Keywords: In-situ resource utilization, solar concentrator, 3D printing, optic fiber, Fresnel lens

Acknowledgements

I would like to express my heartfelt gratitude to everyone who assisted me in completing this thesis report.

I would want to convey my profound appreciation to Mr. Alex Ellery for his guidance, advice, support, and supervision during all the stages of my graduate program. A special thanks to Mr. Alex Proctor for guiding and assisting me with the machine shop equipment and tools. Furthermore, I would also like to acknowledge with much appreciation the crucial role of the staff, who gave the permission to use necessary raw materials and consumable supplies.

I would specifically like to thank LUMATEC Industries in particular for sponsoring the fiber optic cable used in this topic's study and research. Additionally, I am grateful to all of my professors for providing me with information and financial services during my studies at Carleton University.

As a final note, let me thank the examining committee members for agreeing to judge this project, and I hope that this report is an accurate representation of all of the work completed and will satisfy any auditors.

Table of Contents

List of Tables

List of Figure

Chapter 1: Introduction

The development of sustainable manufacturing methods for space exploration is a crucial step towards the colonization of the moon. This requires innovative and cost-effective manufacturing techniques that can utilize local resources on the moon. One of the potential solutions to this problem is 3D printing, which can use In Situ Resource Utilization (ISRU) to create structures and equipment from materials available on the lunar surface. However, most existing 3D printing techniques rely on traditional energy sources, which are not feasible on the moon. Therefore, this study explores the feasibility of using solar energy as a power source for 3D printing on the moon, specifically for printing high-fidelity aluminum metal structures using a solar concentrator-based selective sintering/melting approach.

Hypothesis: A selective solar sintering / melter for high-fidelity 3D printing of aluminum metal may be based on solar concentrator coupling to fiber-optic for heat transmission to any bounded location of a 2D plane. The research builds upon Markus Kayser's approach of a solar concentrator-based 3D printer, aiming to develop a solar concentrator version of selective laser sintering/melting (SLS/SLM) for high-fidelity printing. The first step in this process involves utilizing a Fresnel lens to concentrate solar radiation onto an optical waveguide system, which is subsequently used to melt materials. The distinct characteristics of the optical fibers will also be studied, including the principles of total internal reflection and core-cladding boundary. Electronic components, such as Arduino and RepRap Arduino Mega Polulu Shield, will be utilized to control the 3D printing machine. The successful establishment of a sustainable lunar base is a vital step towards exploring and colonizing the moon. One of the key challenges in this pursuit is the requirement of reliable and cost-effective methods for manufacturing equipment and structures on the lunar surface. The In Situ Resource Utilization (ISRU) approach aims to utilize local resources on the moon, such as regolith, to develop a self-sustaining ecosystem. 3D printing, coupled with the use of solar power, is a promising technology for manufacturing and energy production, respectively. This study explores the feasibility of developing a solar-powered 3D printer capable of printing metal and polymer by building on the idea that it is possible to melt aluminum on a silicone substrate.

This report is divided into five chapters. The first chapter is the introduction, which outlines the hypothesis and the motivation behind the research. The second chapter focuses on the background of space exploration and in situ resource utilization, presenting the area of application. It also explores the concept of replicating machines and rapid prototyping with their deployment on the lunar surface. The third chapter details the apparatus and methodology used for the research consisting of 3D printer design specifications, the Fresnel lens design specifications, and the optical fiber specifications. The experimental results and discussions are outlined in the fourth chapter. Finally, the conclusion and future works are presented in the fifth chapter.

Chapter 2: Literature review

2.1 ISRU

2.1.1 Introduction

ISRU (In-Situ Resource Utilization) capabilities in the context of space exploration include various hardware and operations for harnessing and utilizing resources. These resources include assessing and mapping physical, chemical, mineral, and water resources [1]; extracting, transferring, preparing, and processing resources [2]; and converting resources into products that could be used immediately or as feedstock for manufacturing and construction (such as propellants, life support materials, gases, and fuel) [2]. Potential ISRU-based solutions aim to increase sustainability, decrease life cycle costs [2], reduce launch mass, and/or the number of launchers required [3], and enable the reuse of capabilities of landers and transportation systems, resulting in significant cost savings.

2.1.2 Lunar regolith (Moon soil)

Since the scope of the research deals with ISRU of lunar minerals for 3D printing, it is essential to understand the physical properties of lunar regolith. The physical properties of lunar regolith are mainly the result of mechanical disintegration of basaltic and anorthositic rocks [1], caused by continual meteoric impacts and bombardment by micrometeoroids over billions of years. The process is primarily mechanical weathering, in which particles are ground into increasingly finer sizes over time [4]. This situation fundamentally differs from terrestrial dirt formation, which is mediated by the presence of molecular oxygen (O_2), humidity, atmospheric wind, and a robust array of contributing biological processes..

Lunar soil typically refers to only the finer fraction of lunar regolith, which is composed of grain particles ranging from 10 nm to 1mm in diameter [5]. Lunar soil is made up of various types of particles such as rock fragments, mono-mineral fragments, and various glasses such as agglutinate particles, volcanic and impact spherules [4]. The agglutinates formed at the lunar surface by micrometeorite impacts, which cause small-scale melting that fuses adjacent materials with tiny specks of elemental iron embedded in the glassy shell of each dust particle [6]. While some material from external sources may contribute to the composition, the majority of the soil at any given location reflects the local bedrock.

The chemistry of lunar regolith and soil differs significantly from that of terrestrial materials in two ways. First, the Moon is extremely arid, resulting in the absence of minerals containing water, such as clay, mica, and amphiboles on its surface [7]. Second, unlike the Earth's crust, the Moon's regolith and crust are chemically reduced rather than being heavily oxidized. This is partly due to the constant bombardment of protons from the solar wind on the lunar surface. These differences between Earth's soil and lunar soil make it difficult for plants to grow on the Moon [8]. Therefore, colonizing the Moon and other long-term space missions may require expensive and challenging efforts to provide food, such as bringing in Earth soil, chemically treating lunar soil to remove heavy metals and oxidize iron atoms, and carefully reproducing strains of plants that are adapted to the hostile lunar regolith [8]. A total of 381.7 kg of rock and regolith samples were collected from six different sites on the lunar surface during various Apollo missions [9]. Oxygen is the most abundant chemical element in both Earth and Moon rocks, accounting for 41-45% of the Moon. The chemical composition of lunar dust varies depending on where you look on the moon. The concentration of SiO_2 in lunar regolith is relatively high compared to other elements, but it is mostly present in the silicate minerals anorthite, pyroxene, and olivine, with quartz being rare on the Moon [10]. Anorthite is a mineral that belongs to the plagioclase feldspar group. Its chemical formula is $CaAl_2Si_2O_8$, which means it consists of

Mission	Apollo 16	Luna 20	Apollo 14	Apollo 17	Apollo 15	Apollo 12	Apollo 11	Luna 16	Luna 24
Sample	**64501**	**22001**	**14163**	**76501**	**15271**	**12033**	**10084**	**21000**	**24999**
SiO_2	45.2	*	47.4	42.8	46.3	47.0	41.3	*	*
TiO_2	0.4	0.5	1.6	3.3	1.4	2.5	7.3	3.3	1.0
Al_2O_3	27.6	22.9	17.5	18.2	16.2	13.8	13.6	14.9	11.1
Cr_2O_3	0.1	0.2	0.2	0.3	0.4	0.4	0.3	0.3	0.4
FeO	4.4	7.4	10.4	11.1	12.9	15.1	16.0	16.4	20.3
MnO	0.1	0.1	0.1	0.1	0.2	0.2	0.2	0.2	0.3
MgO	4.7	8.9	10.1	11.9	11.1	9.5	8.3	8.3	10.4
CaO	16.6	14.2	11.3	12.3	11.1	10.6	12.3	11.8	10.7
Na_2O	0.4	0.3	0.7	0.4	0.5	0.7	0.4	0.4	0.3
K_2O	0.1	0.1	0.6	0.1	0.2	0.4	0.2	0.1	0.0
Total	99.6	*	99.9	100.5	100.2	100.1	99.9	*	*

Table 1 Major chemical constituents of lunar dust [11]. *No Si exists from the data sets of lunar samples [12]

calcium (Ca), aluminum (Al), silicon (Si), and oxygen (O). Pyroxene is a group of rock-forming inosilicate minerals with the general chemical formula $(Mg,Fe)SiO_3$. The exact chemical composition can vary depending on the specific type of pyroxene. For example, augite, one of the most common pyroxene minerals, has the chemical formula $(Ca,Na)(Mg,Fe,Al,Ti)(Si,Al)_2O_6$. Olivine is a group of minerals that have a similar chemical composition. The general formula for olivine is $(Mg^{2+},Fe^{2+})_2SiO_4$, where Mg represents magnesium, Fe represents iron. Olivine can have different amounts of magnesium and iron, resulting in variations in its properties. From Table 1, The composition of SiO_2 in the samples collected from lunar surfaces is approximately 50%, followed by Al_2O_3 at 15%, CaO at around 10%, MgO at 10%, and TiO_2 at 5%. [13]. Iron, along with sodium, potassium, chromium, and zirconium, is also present in the samples, ranging from 5-15%. Some free iron naturally alloyed with nickel and cobalt is also found in the regolith (0.5% by weight) [14]. It is also observed from Table 1 that the presence of Si was absent in a few sample collections. This is due to the non-uniform distribution of SiO_2 on the Moon, which varies according to the location and depth of regolith. One major factor contributing to this variation is meteorite impacts, which excavate materials from the subsurface and expose different layers of regolith with varying compositions. From the mission samples, the presence of titanium was established, and its alloys can be utilized for lightweight aerospace components.

2.1.3 ISRU exploration techniques

In 2009, the Indian spacecraft Chandrayaan-1 used its spectrometer to find water molecules on the Moon. The spacecraft was equipped with a terrain mapping camera, which is a CMOS (complementary metal-oxide semiconductor) camera to produce high-resolution map of the Moon [15]. Chandrayaan-1 mapped the entire lunar surface and provided detailed information on the Moon's topography, mineral composition, and geological history. Another instrument utilized on the Chandrayaan-1 spacecraft was the Moon Impact Probe (MIP) [16] developed by the Indian Space Research Organization (ISRO). MIP is an impact probe that includes a C-band radar altimeter to measure the probe's altitude, a video imaging system to acquire images of the lunar surface, and a mass spectrometer to measure the constituents of the lunar atmosphere [17]. Apart from these, the major discovery made by Chandrayaan-1 was the evidence of water molecules in the lunar soil, which were thought to be embedded in a glassy bead formed by the intense heat of meteorite impacts [18]. Water is an essential resource that can help humans prosper in new lands and enable further space exploration. It serves not only as a consumable for humans but also as a critical component in ISRU technologies for obtaining hydrogen and oxygen through electrolysis. Studies indicate that water ice and other volatile compounds are present in the permanently shadowed craters on the Moon. Measurements taken by the lunar prospector [19] and the Lunar Exploration Neutron Detector (LEND) on the Lunar Reconnaissance Orbiter (LRO) [20] show that the polar regions of the Moon have a high concentration of epithermal hydrogen. These are hydrogen atoms that have been implanted into the lunar regolith by solar winds, a stream of charged particles that flow from the sun. According to temperature maps created by the Diviner Radiometer aboard the LRO, water remains stable at the surface in the polar craters or behind a shallow overburden no deeper than one meter in the areas surrounding these craters [21].

2.1.4 Resource extraction techniques

Extraction techniques classified under mining include (i) fragmentation or breaking up the rocks by different methods such as explosive, mechanical, thermal, or chemical methods, (ii) excavation or picking up the resources using mechanical or chemical methods, and (iii) transportation or conveyance methods such as augers (screw conveyors), pneumatic conveying, magnetic conveying, pumping, vibratory conveying, belt conveyors, bucket elevators, cable cars, slurry lines, and loaders/haulers [22]. Comminution of feed material is typically the first step in most mineral processing [23]. Although centrifugal force can be used to power crushing and grinding methods such as vertical shaft impactors, it is less common in industry. Even impact crushers that use gravity as a feed mechanism require regular wear part replacement. Equipment like pressure crushers prevents rocks from discharging upwards, which could cause suspension or have a negative impact on crushing efficiency by increasing the travel time of dust. A similar effect is seen with impact crushers, where the rocks are kept from discharging upwards rather than crushing. This has increased dust formation but has no effect on the mechanism.

2.1.5 Consumable production

Oxygen is an important element to extract from lunar regolith because it is used as a component of life support systems in spacecraft and by human crews in space, as well as a key component of water, propulsion oxidizer, and plant growth. There are three main methods to extract oxygen from regolith. The first is carbothermic reduction, which is a multi-step process involving the elevated temperature reaction of oxides [24]. In this process, metallic oxide is first reduced by reacting with a carbonaceous source (such as methane) to form carbon monoxide and hydrogen. The carbon monoxide is then reduced by hydrogen to form methane and water [25], and finally, oxygen is produced by the electrolysis of water formed in the previous step. One way to extract oxygen from regolith

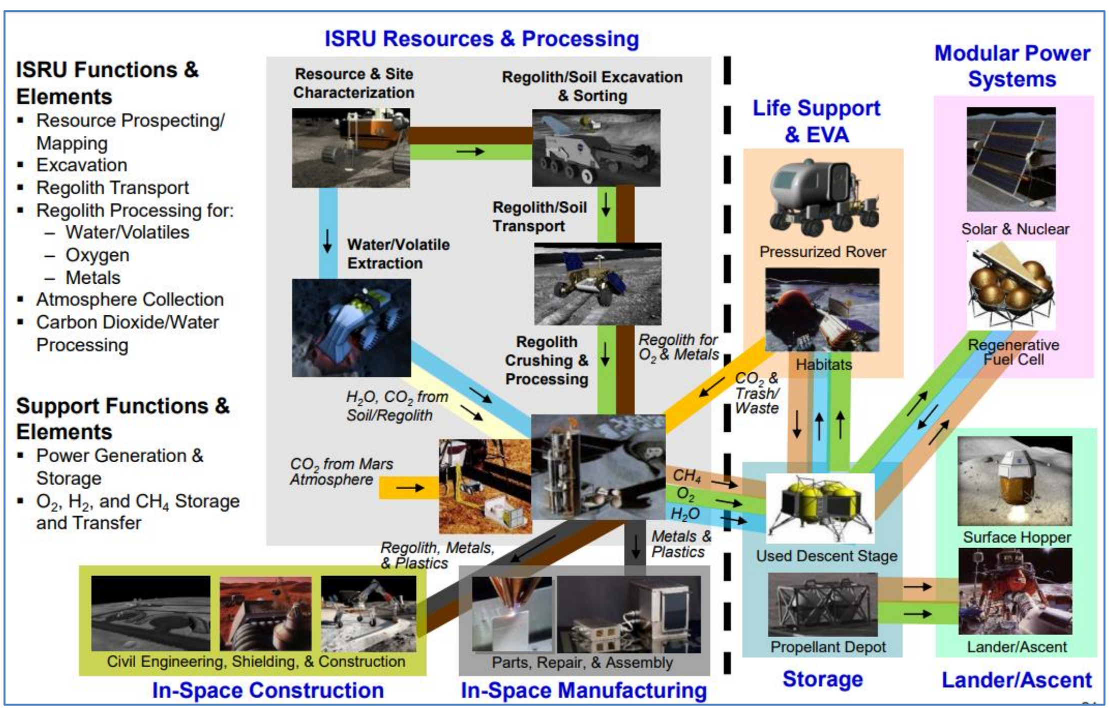

Figure 1 ISRU integrated with exploration elements [2]

is through the hydrogen reduction of regolith method, which uses hydrogen as a reducing chemical reagent to extract oxygen by a high-temperature reaction of iron oxides followed by water electrolysis [26]. This process consists of two basic steps: the first involves reducing minerals containing iron oxides (e.g., Ilmenite $FeTiO_3$) by reaction with heated pure hydrogen (at nearly 900 °C) to form water vapor, and the second involves electrolyzing the formed water after purification to separate hydrogen and oxygen [27]. Examples of projects that have evaluated this technology include PILOT (Precursor In-situ Lunar Oxygen Testbed) by Lockheed Martin Astronautics [28] and the ROxygen project by Johnson Space Center (JSC), Glenn Research Center (GRC), and Kennedy Space Center (KSC) [29]. A third method is molten regolith electrolysis, which involves dissolving naturally high-oxide lunar regolith in a molten oxide solvent that already contains liquefied regolith and produces liquid metal as the end product and oxygen as a by-product [30].

As with oxygen, metals are also crucial to sustainable space exploration, because they can be used to fabricate spacecraft parts, spare parts, and repair spacecraft if necessary. Metals can be extracted simultaneously as a co-product in hydrogen extraction technologies (carbothermic reduction [24] and molten regolith electrolysis [30]) because they involve splitting oxide molecules. Aluminum is one of the most abundant elements found on the Moon, and its presence has been extensively studied by several lunar missions. Aluminum is a crucial resource on the Moon due to its versatile properties and wide range of potential applications. The Apollo missions brought back samples of rocks and soil that contained significant amounts of aluminum. The Lunar Prospector mission also detected high levels of aluminum on the lunar surface, particularly in the form of the mineral anorthosite, which is rich in aluminum and calcium. Aluminum has various uses on the Moon, including as a structural material for building habitats and infrastructure, as a heat shield to protect spacecraft and habitats from extreme temperatures, and as a conductor for transmitting electrical signals. Additionally, aluminum could be used for manufacturing various tools and equipment, and its alloys can be used for creating lightweight and durable machinery. The availability of aluminum on the Moon could significantly reduce the cost and logistical challenges associated with transporting materials from Earth. The aluminum present in the samples is a good conductor of electricity, and atomized aluminum powder can also be used as solid rocket fuel when burned with oxygen [14]. When lunar anorthite is treated with HCl acid, it yields SiO_2 and Al_2O_3. An FFC Cambridge process can be potentially established to reduce Al_2O_3 to Al metal on the moon. The process utilizes a molten salt electrolysis technique, where a high-temperature electrolyte consisting of a mixture of molten salts is used to dissolve Al_2O_3. This electrolyte mixture is then electrolyzed using a cathode made of a liquid metal alloy, which is floated on top of the molten salt electrolyte. As the electric current passes through the electrolyte, aluminum ions are reduced at the cathode, forming a pool of molten aluminum metal that can be collected. This process has several advantages, including the fact that it does not require the use of carbon-based reductants, which can be difficult to obtain on the Moon. Additionally, the process can be operated at lower temperatures than other methods of aluminum production, which reduces energy requirements and makes it more suitable for use on the Moon where energy is at a premium [31].

2.2 In situ energy

Energy is one of the main elements of ISRU because it is fundamental to everything humans want to do in space. Moon village concepts rely heavily on on-site resource utilization for energy production. Researchers are working on the development of an electric power system on the Moon based on the direct fabrication of solar cells with basic materials (Si, Fe, TiO_2, Ca, Al, etc. [32]) collected and processed from lunar regolith and benefiting from the Moon's ultra-high vacuum environment, which allows vacuum deposition of thin film silicone [33]. The vacuum environment is used by vaporizing a target substance with an electron beam. The vapor allows for the formation of delicate layers of silicon, aluminum, and other materials. Vacuum vapor deposition can produce homogeneous layers with superior mechanical properties. This lays the groundwork for manufacturing solar cells from silicon and other materials through zone refining and thermodynamically produced epitaxial growth in the vapor phase [33]. However, such high-efficiency fabrication is incompatible with lunar production and obtaining materials

Layer	Thickness Range	Type	Source Materials	Indigenous Minerals	Fabrication Technique
Top electrode	0.1-1 micron	Metallic Ca, Ca/Fe, or Al	Lunar Ca, CaAl, Fe	Yes: Anorthite, Ilmenite	Vacuum thermal evaporation
Antireflection Coating	0.1-0.2 micron	TiO_2 or SiO_x or AlO_x	Regolith	Yes :from Ilmenite ($FeTiO_3$) Anorthite ($CaAl_2Si_2O_8$)	Vacuum Thermal Evaporation
N-type Si	0.1-0.3 micron	Si doped with As, P, or S (doping about 100-200PPM)	Lunar Si N-dopant	Yes: (Anorthite) PO_x and S are present in low quantities in minerals	Co-evaporation of Si and dopant
P- type Si	1-10 micron	Si doped with Al (20-50 PPM)	Lunar Si	Anorthite	Vacuum thermal evaporation
Bottom Electrode	1 -2 micron	Al, Ca/Fe	Lunar Al	Anorthite	Vacuum thermal evaporation
Substrate	2-5 mm	Glass mineral	Lunar soil	Yes	Solar thermal melting

Table 2 Lunar solar cell components [34]

from extraterrestrial sources will be extremely difficult. Individual components of the lunar-solar cell are highlighted in Table 2. Fabrication is possible with almost all of the required materials available. Another way to harness energy on the moon's surface is through solar cell concentrators [35]. Solar concentrators can be used to generate thermal energy for pyrochemical, electrochemical, sintering, or melting processes, such as 3D printing. A parabolic reflector horn, part of the compound parabolic reflector, directs radiation from the aperture to the absorber [36]. It has a planar entrance aperture, a completely internal reflecting profile, and an exit aperture. These components are typically used to heat working fluids because they are not suitable for high-temperature solar concentration. As an alternative to reflecting mirrors as solar concentrators, conventional refractive lenses can be used. For instance, liquid water lenses can achieve concentration ratios of 100 or higher, although this is insufficient for purposes such as lunar power generation [37]. Fresnel lens concentrators are tiny lenses that mimic traditional spherical lenses by having concentric prismatic grooves carved into them. According to its radius, each circular groove behaves as a prism to create a single focus at a slightly varied angle.

Nuclear-based high-intensity thermal sources frequently use thermal-to-electric conversion [33]. A Seebeck effect is utilized where a temperature difference between two dissimilar electrical conductors or semiconductors produces a voltage difference between them. This effect was discovered by Thomas Johann Seebeck in 1821. The Seebeck effect occurs due to the presence of charge carriers (such as electrons) in a conductor. When a temperature difference is applied to the conductor, the charge carriers on the hot side move more rapidly and have a higher kinetic energy than those on the cold side. This results in a buildup of charge carriers on the hot side and a corresponding decrease in the number of charge carriers on the cold side, leading to the creation of a potential difference across the conductor [38]. The magnitude and direction of the voltage produced by the Seebeck effect depends on the materials used in the conductors and the temperature difference between them. This effect has important applications in thermoelectric generators, which convert heat energy into electrical energy, and in temperature measurement devices, such as thermocouples. A thermopile can be created by stacking thermocouples in sequence. Solar concentrators may be used in conjunction with vacuum tube-based thermionic conversion to generate electrical energy [39].

2.3 Optical waveguide system for solar power applications

Solar energy is a readily available energy source in space. In most cases, solar energy is first converted to electrical energy and then used for various applications. However, for some applications, it is more efficient to utilize solar energy directly. Recently, researchers are developing an optical waveguide (OW) system [40] for solar power utilization in space. An example of the OW system for thermochemical material processing is given in Figure 2. In this system, solar radiation is collected by the concentrator array, which transfers the concentrated solar radiation to the OW transmission line made of low-loss optical fibers. The OW transmission line directs the concentrated solar radiation to the thermochemical receiver for the processing of lunar regolith for oxygen production.

The aforementioned system concept is based on the use of optical fibers for the transmission of solar radiation. The first theoretical study on the application of optical fibers to power transmission was conducted by Kato and Nakamura [40] [41]. Based on their analyses, Kato and Nakamura concluded that fused silica-core optical fibers can be employed in the transmission of solar radiation for photovoltaic, thermal, and lighting applications. There are several key advantages to this system, such as the ability to transmit concentrated solar power via flexible OW, the ability to scale up the system's power by increasing the number of concentrators, the ability to be autonomous, stationary, or mobile,

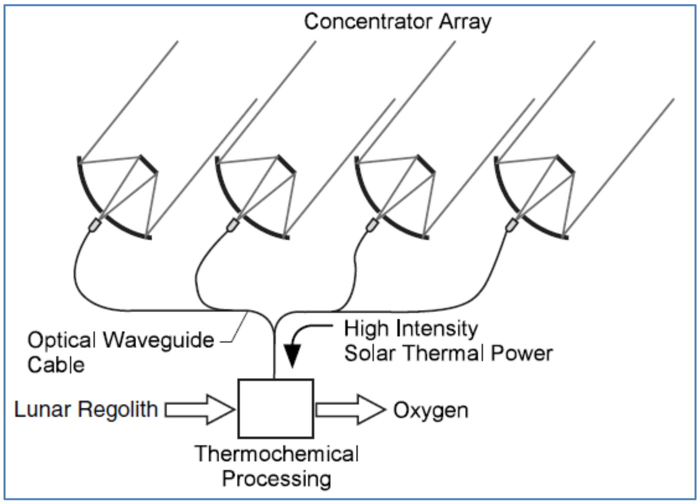

Figure 2 Optical waveguide system for thermochemical material processing [40]

and the ability to transport it to the surface of the Moon and use it for a number of applications. The experiments were successful to generate temperatures in the region of 1000°C for the sintering of Tephra [41] (figure 3) and around 1800°C for oxygen production reactor interface [40] (figure 4). Stabilization of the lunar surface can be accomplished by regolith sintering which takes place at a temperature of approximately 1000°C. NASA/KSC [42] has carried out sintering tests for stabilizing the lunar surface, and the treated samples have been thoroughly characterized. Tephra, a locally produced volcanic ash, served as the model lunar regolith in this set of tests. The ash is then spread out on a flat surface, and a solar sintering machine is used to concentrate the sun's rays onto the material. The heat from the sun melts the tephra, which then solidifies into a hard, durable material as it cools. Approximately, 540 W of solar energy was transferred to the surface of the tephra. Tephra was sintered across a small temperature range of 1,000-

1,100°C. High OH-content optical fibers with a fused silica core and polymer cladding were used for the program [43]. The fiber is covered with a Tefzel coating for protection.

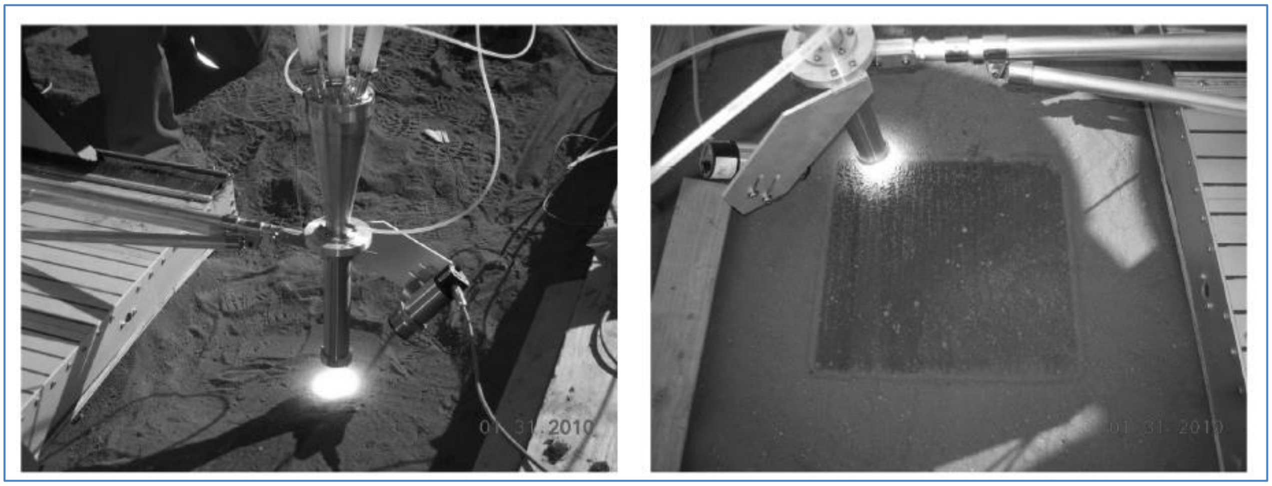

Figure 3 Solar sintering of Tephra surface [41]

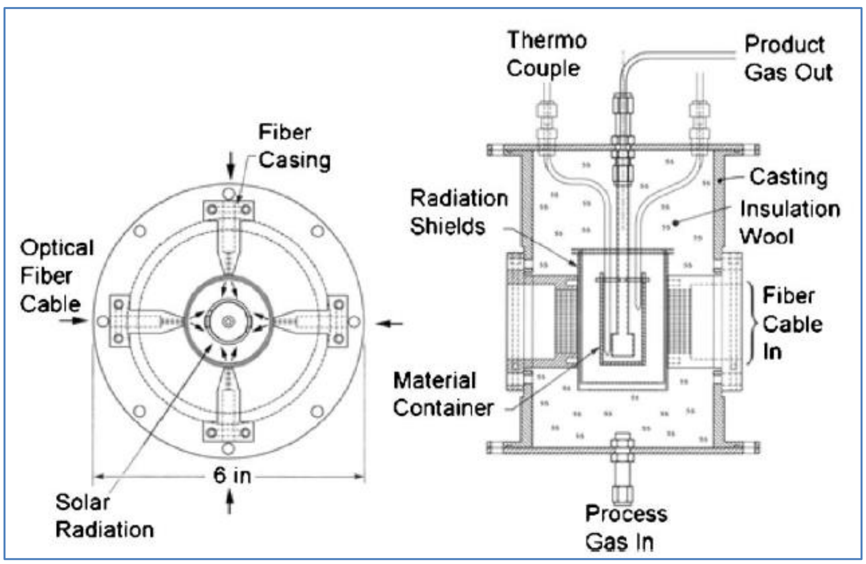

Figure 4 Solar thermal reactor [40]

Within the stainless-steel thermal reactor is a ceramic insulator. Four aluminum wedges containing optical fibers direct solar radiation radially inward onto the reactor. The reactor core is filled with a reactant gas that produces water vapor. At the reactor's outflow, the water vapor concentration is measured [40]. Despite the program's success, the researchers stated that the optical waveguide solar power system needs to be operated at temperatures below 120°C. When the total temperatures achieved exceed 1000°C, this statement becomes somewhat difficult to interpret. Similar complications were observed on applying the same principles in this thesis. The temperature range was constrained and did not exceed the operational temperatures of the optical fiber cables.

2.4 Solar sintering by Markus Kayser

In the year 2011, Markus Kayser [44] in the deserts of Morocco experimented to answer the question of energy production and material shortages by exploring the potential of desert manufacturing. The idea was to direct the beam of sunlight (1400°C to 1600°C) from the Fresnel lens to melt the silica from sand, building glass objects layer by layer. Here, the sunlight and sand are used as raw energy and material to produce glass objects using the 3D printing process. The solar-powered motors move in the x and y axis along the computer-controlled path and a new layer of sand is sprinkled on top after each passage of a light beam. The light sensors track the sun as it moves across the sky and the whole machine rotates to ensure the lens is always producing the optimum level of heat. Once all the layers are melted into place, the piece is allowed to cool and then dug out of the sandbox. The surface finish of the product was coarse and rugged [45].

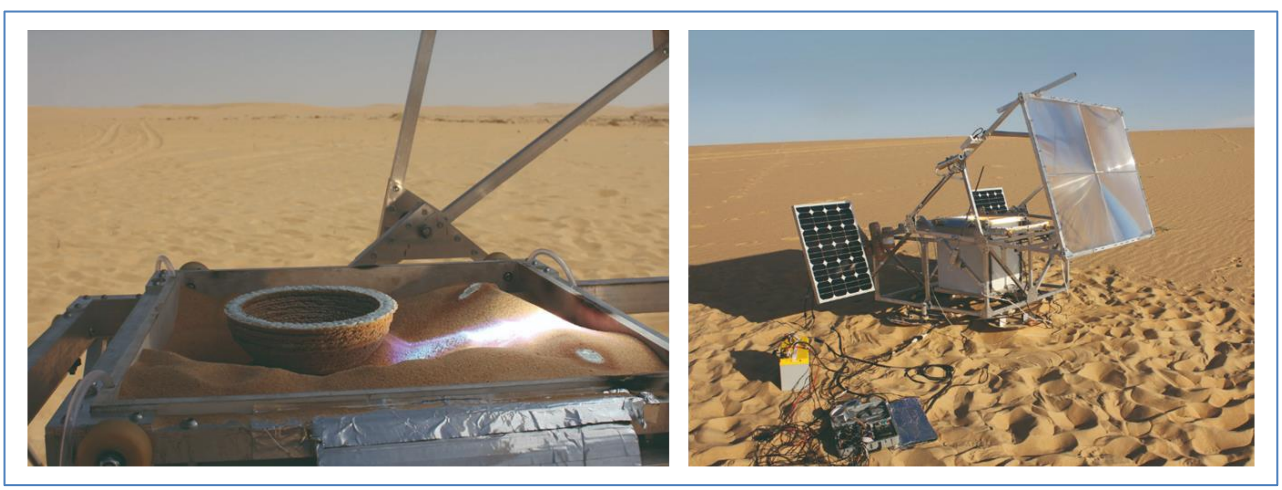

Figure 5 Solar sintering of sand using focused sunlight beam [44]

2.5 Summary

Researchers, engineers, and entrepreneurs are collaborating to develop novel ways for the efficient use of solar radiation in the generation of renewable energy. Solar concentrators can generate temperatures high enough to melt metals, and thermal energy can be used to 3D print items. These efforts will contribute to the development of space manufacturing processes. However, the idea of utilizing solar concentrators to provide thermal energy for 3D printing has not received much attention. The research conducted in this field is minimal, with few successful initiatives to highlight. The development can further lead to printing circuit boards using ISRU on the Moon. The presence of aluminum, silicon, and iron can pave the way to create circuit boards using the 3D printing technique on the Moon. The benefits range from reduced material transportation costs to customizable designs that meet suitable mission requirements, sustainability by using local resources, and reducing the reliance on Earth-based resources.

Chapter 3: 3D printing

In-situ manufacturing (ISM) is a key component of ISRU. It refers to the ability to produce the necessary tools, parts, structures, and spares in situ. It is responsible for developing manufacturing capabilities for sustainable, on-demand operations during future space missions. In contrast to launching every manufacturing material and building block from Earth, ISM offers many benefits, such as (i) cost, volume, and mass savings during launch [46]; (ii) work can be done from Earth, a station, a spacecraft, or anywhere in space by just sending CAD files and designing parts in situ [46]; (iii) producing on-demand products in lesser amounts of time [46]; (iv) ability to recycle used or obsolete parts into powder or wire feedstock for later use in manufacturing [46]; (v) more flexibility and reduced risk when fixing broken or damaged systems [46]. It is true that 3D printing is a key component of ISM [47], but it is not the only one. In fact, ISM leverages many other technology development areas such as (i) printing electronics, enabling in-space fabrication of functional electronics like electronic components, sensors, circuits, etc. [48]; (ii) multi-material 3D printing is a desirable capability for space missions because it allows for large, high-strength components, structures, and more repair capabilities; and (iii) use of additive manufacturing technologies to construct shelters and bases in space, which will provide a suitable environment for humans and robots to work efficiently [47].

The process of 3D printing is an additive manufacturing method that involves printing layers of material to create a real object from a digital file containing the 3D data for the object. The most common material for printing is plastic, but it is also possible to print metal (such as gold, silver, titanium, or aluminum), or even ceramic or concrete. There are a multitude of methods for printing an object in 3D. Even if the printing techniques are different, the principle remains the same: superimposing layers of materials according to the coordinates transmitted by a 3D computer-aided drawing file. Some of the most common 3D printing technologies are stereolithography (SLA), a process where a photosensitive resin is solidified by ultraviolet radiation [49] and Selective Laser Sintering (SLS), which includes a laser that fuses powder by sintering the material to create 3D objects layer by layer [50]. Fused Deposition Modeling (FDM) developed by Stratasys (USA) is another successful method because it is relatively inexpensive and fast. It begins with depositing a wax, polyamide, polypropylene, or ABS thread (Thermoplastic) layer by layer on a print bed until the final object is obtained [51], and finally, (iv) Multi-Jet Modeling is a method similar to what a 2D printer does with ink. For each stratum of the object to be designed, the 3D printer deposits a layer of resin (acrylate or polypropylene) [52]. The approach for the 3D printer design was based on two types of 3D printing techniques: fused deposition modeling and selective laser melting.

Fused deposition modeling (FDM) is an additive manufacturing technology that creates 3D components using a continuous thermoplastic or composite material thread in filament form. An extruder feeds the plastic filament through an extruding nozzle, where it is melted and then selectively deposited layer by layer onto the build platform in a predetermined automated path. FDM is one of the seven main types of additive manufacturing technologies [53]. Scott Crump pioneered the process in the 1980s [54] under the registered term fused deposition modeling (FDM). Stratasys Inc, a business co-founded by Scott Crump, owns the trademark fused deposition modeling (FDM) and its abbreviation FDM. The schematic below (Figure 6) shows a basic overview of an FDM printer. It is made up of two extruding nozzles on linear slides, a build platform on another linear slide, and plastic filament spool supports. There are three basic types of FDM: single extrusion, dual extrusion and multi material extrusion. Dual extrusion and multi materials are not the same. Dual extrusion refers to a 3D printer that has two separate extruder nozzles that can be used to print with two different filaments or colors at the same time. Multi-material extruders, on the other hand, are designed to print with more than two materials at once and can have multiple extruders that can print different materials simultaneously or in combination to create unique material properties. While dual extrusion is a type of multi-material printing, not all multi-material printing involves dual

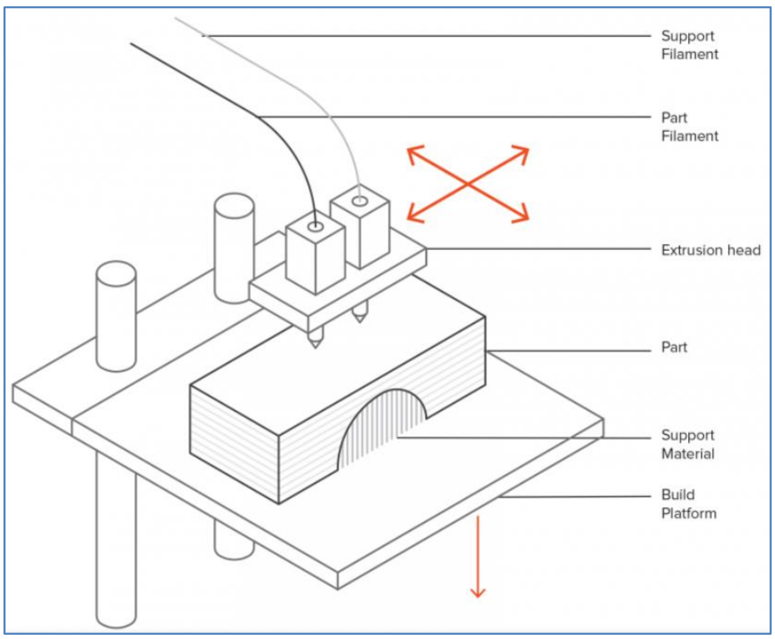

Figure 6 Overview of an FDM printer

extrusion. The extruders are called model and support extruders. As the name implies, the model extruder prints the material for the 3D shape while the support extruder prints the supports. They can either have the same material or varied materials. The movement could start from the extruders in the X-axis direction or Y-axis direction or Z-axis direction or with the build platform, depending on the type and brand of FDM printer. As the schematic illustrates, in this design, the extruder head gantry travels in X & Y while the build platform moves in Z-axis arrives. In some versions, the print head moves in X and Z while the build platform moves in Y axis direction. FDM process steps include part preparation step, FDM machine setup step, FDM printing step, FDM part removal, and post-processing.

There are different types of FDM 3D printer styles like cartesian, delta, polar, CoreXY and SCARA (Selective Compliance Articulated Robot Arm). Cartesian style 3D printers are one of the most common types of 3D printers used today. They are named after their three axes of motion: X, Y, and Z. They use a Cartesian coordinate system to control the movement of the print head, which can move along the X and Y axes, while the build plate moves along the Z axis. In Cartesian 3D printers, the print head is typically mounted on two rods or rails that move back and forth along the X axis. The build plate is mounted on a third rail that moves up and down along the Z axis. The print head can also move up and down along the Z axis to adjust the height of the print. Cartesian 3D printers are versatile and can be used to print with a wide variety of materials, including plastics, metal infused polymers, and composites [55]. They are also relatively easy to assemble and modify, which makes them popular among hobbyists and makers. However, Cartesian 3D printers can suffer from some issues, such as backlash, which can cause inaccuracies in the printed object. They also tend to be larger and heavier than other types of 3D printers, which can limit their portability. A delta style 3D printer is a type of Cartesian coordinate system used in 3D printing. It is named for its triangular shape, resembling the Greek letter Delta. Instead of a moving bed, the delta printer has a fixed bed and a movable print head that moves along three vertical columns. The print head is suspended by three arms connected to the columns, allowing it to move in all directions. The delta printer is known for its speed and accuracy, particularly in printing tall objects, due to its unique design.

However, it can be more difficult to calibrate and maintain than other types of printers [56]. A polar-style 3D printer is a type of delta-style 3D printer that uses a polar coordinate system to move the print head. In a polar-style 3D printer, the print bed is stationary, and the print head is suspended from three arms arranged in a triangular shape above the print bed. The print head moves in a circular motion, with the three arms controlling its position in the X, Y, and Z directions. The advantages of polar-style 3D printers include faster print speeds, as the print head can move in a continuous motion without stopping and starting. The design also allows for a larger build volume in a smaller overall machine size, as the triangular arm structure takes up less space than the linear rails used in Cartesian-style printers. However, polar-style printers can be more complex to calibrate and set up than other types of printers and may require more maintenance to keep the arms and joints moving smoothly [57]. CoreXY is a type of 3D printer design that uses a system of two stepper motors and belts to control the movement of the print head. The motors and belts are positioned in a way that allows for very precise and accurate movement of the print head, resulting in high-quality prints. The CoreXY design is similar to a Cartesian 3D printer, but it uses a different system of movement that allows for faster and more precise printing. CoreXY printers are often used for complex and detailed prints, such as models with intricate geometries or moving parts. They are also popular for printing larger objects due to their increased stability and accuracy. However, CoreXY printers can be more difficult to assemble and calibrate compared to other 3D printer designs [58]. SCARA (Selective Compliance Assembly Robot Arm) is a type of robotic arm that is commonly used in industrial automation and robotic applications. SCARA style 3D printers are similar to traditional SCARA robots but are specifically designed for 3D printing applications.

SCARA 3D printers have a fixed base and a vertical arm that moves in the X-Y plane. The end of the arm holds the printing nozzle, and the arm moves the nozzle over the print bed to create the 3D object. The vertical arm is driven by motors and a series of belts or gears that allow for precise movement. SCARA 3D printers are known for their speed and accuracy, and they are commonly used in high-volume manufacturing and prototyping applications. They are especially well-suited for applications that require precise, repetitive movements and for printing small to medium-sized objects. However, they are typically more expensive than other types of 3D printers and can be more complex to set up and operate [59]. Out of these, cartesian type is the most common and popular due to its simplicity, reliability, and affordability. Additionally, Cartesian printers are relatively easy to modify and upgrade, making them a good option for those who want to customize or enhance their printer which is in our case since we are modifying the extruding heads to accommodate the fiber optic cable. A few advantages of FDM are as follows. It is the most cost-effective method of manufacturing thermoplastic components and prototypes. Additionally, due to the lower cost of FDM printers and wide availability, the lead times are minimal and cheaper than other additive manufacturing processes. There is a wide range of thermoplastic materials accessible for prototyping, as well as some non-commercially viable options. Out of the available thermoplastic options, PLA (Polylactic acid), ABS (Acrylonitrile Butadiene Styrene), PETG (Polyethylene Terephthalate Glycol), Nylon, TPU (Thermoplastic Polyurethane), PC (Polycarbonate), and PVA (Polyvinyl Alcohol) are commonly utilized. Most common injection molding materials can be replicated using FDM. Furthermore, FDM technology makes complex shapes and voids that would otherwise be impractical possible. The disadvantages of FDM include the fact that it has the lowest accuracy and resolution when compared to other 3D printing methods, making it unsuitable for items with delicate details. FDM items are prone to visible layer lines, which requires post-processing to achieve a smooth finish [60]. This can also be avoided by using more thin layers of print but at the expense of printing time. The FDM technique is developed to print polymers. Thermoplastics stock can be brought to moon in order to 3D print using FDM. PLA can be derived from the biomass of fermented plant starch such as corn or sugarcane if lunar farming is established.

Selective laser melting (SLM) is an additive manufacturing approach defined by the ISO/ASTM known as powder bed fusion [53]. In SLM, a laser generally ranging from

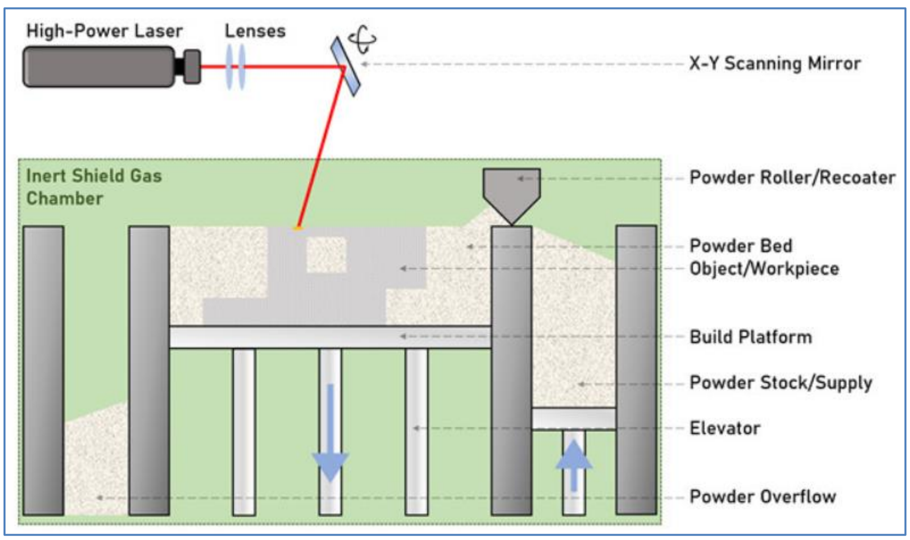

Figure 7 Functional diagram of SLM 3D printers [61]

100 watts to 1000 watts selectively melts the metal powder into a part in a layer-by-layer process. A high-powered laser is a type of fiber laser which uses optical fibers as the active pumped seed laser that is coupled to an amplifier fiber, which increases the power of the laser beam. SLM is distinct from similar powder bed fusion techniques such as selective laser sintering (SLS), where it fully melts metal, instead of sintering. Figure 7 shows the

functional components of SLM printers. We will explore this diagram and use its labels to explain how SLM printing works. After the model is uploaded onto the printer firmware, the powder stock is filled with the appropriate metal powder via a hopper or automatic cartridge. An inert gas (typically argon) [62] is pumped into the sealed build chamber to shield the metal from oxidation in the presence of the high-powered laser beam. These lasers are typically high-wattage ytterbium fiber lasers [62], which get hot enough to melt powdered metal but also create huge temperature differentials.

The printing process begins when the roller/re-coater spreads a thin layer of powder from the power stock onto the build platform. The laser is then focused and directed by a controlled X-Y scanning mirror to selectively melt the powder in the shape of the first layer. After this layer is sufficiently cooled, the build platform increments down in the Z direction while the powder stock increments up in the Z direction by the same amount. The printing process is repeated over again for each layer until the final part is encased in unused powder on the build platform. After printing, the part is removed from the build platform and is post-processed according to the part's application. Unlike other powder-bed 3D printing technologies, SLM must implement extensive support structures to prevent warping on small angles and overhangs as the part cools. These supports also function as heat sinks, wicking away heat from the laser site to prevent significant defect formation in components. SLM are beneficial as they create fully metal, high-performance parts that are highly accurate and detailed. Moreover, the range of materials in SLM is large, encompassing high-strength and specialty in metals. This includes metals like stainless steel, titanium, aluminum, cobalt-chrome, and gold too. Further it can print ceramics, polymers like nylon and PEEK and composites polymer-infused like carbon fiber. SLM speeds up metal manufacturing techniques, reducing delays in repairs, and increasing the pace of production. It also reduces material usage and waste, especially when compared to traditional manufacturing methods. The limitations of the SLM include the acceptance of single-component metals and specified materials with good flow characteristics; compromising the structural integrity due to the dislocation of parts caused by temperature gradients due to SLM being a high energy process; SLM parts need extensive support structures and requires a source of inert gas. Further, SLM parts have a rough surface finish out of print and require a lot of post-processing to take place. The main disadvantage of this approach is that it has a size constraint on parts and is very expensive, limiting it to small-batch manufacturing runs [61].

SLM can use a variety of metal powders, including titanium and aluminum, which are abundant on the moon. This is particularly useful for creating parts for lunar habitats or infrastructure, which require unique and complex designs to meet the specific requirements of the lunar environment. The SLM process can be easily automated, which reduces the number of personnel required for printing and increases the speed and efficiency of the printing process. Sintering of regolith on the Moon using parabolic mirrors is a concept that has been proposed for in-situ resource utilization (ISRU) and lunar construction purposes. Parabolic mirrors can be used to concentrate sunlight into a small focal point, generating high temperatures that are necessary for the sintering process. By directing the concentrated sunlight onto the regolith, the temperature of the regolith can be raised to the point where it becomes molten. As the regolith cools down, it solidifies and forms solid structures. The same capabilities are exhibited by Fresnel lens and are more compact and light weight compared to parabolic mirrors dishes.

3.1 3D printing in space

The ability to create spare parts in space is made possible by 3D printing technology. In this regard NASA and Made in Space (MIS) have made great strides. The Zero G 3D printer [63] from Made in Space uses molten filament deposition technology and has been specially developed to operate in a zero-gravity environment. It has enabled the production of a spare crank from the International Space Station. Previously, it was necessary to wait months for a piece or an object to arrive on board the ISS. Today, it is enough to send the plans and print them. This progress is due to Made In Space, the company that developed the first 3D printer capable of operating in zero gravity [64]. This new prototype has been available on the ISS since September 2014. Zero-G 3d printer operates in much the same way as a 3D printer on Earth would function using FFF (Fused Filament Fabrication) technology. Since there is no gravity to pull the molten plastic downward, the printer must use a different method to keep the plastic in place as it is extruded. To do this, Zero-G 3D printers use a combination of extrusion pressure, surface tension, and temperature control to control the flow of molten plastic and maintain the shape of the printed object. The printer's extruder applies pressure to the molten plastic, while the printer's heated build platform and chamber maintain the proper temperature to prevent the plastic from solidifying too quickly [63]. In addition, the printer must be designed to operate in a microgravity environment, which means that it must be able to securely hold its position without the use of gravity. This is typically accomplished using a combination of mechanical fasteners, suction cups, and magnetic clamps. Following these preliminary testing, the pieces will be returned to Earth to examine the influence of gravity on the prints and so perfect the process. The use of a single material and the absence of spare parts provides for significant space savings in the station.

In March 2016, NASA sent yet another refueling mission to the International Space Station (ISS). A high-tech 3D printer called AMF for the Additive Manufacturing Facility

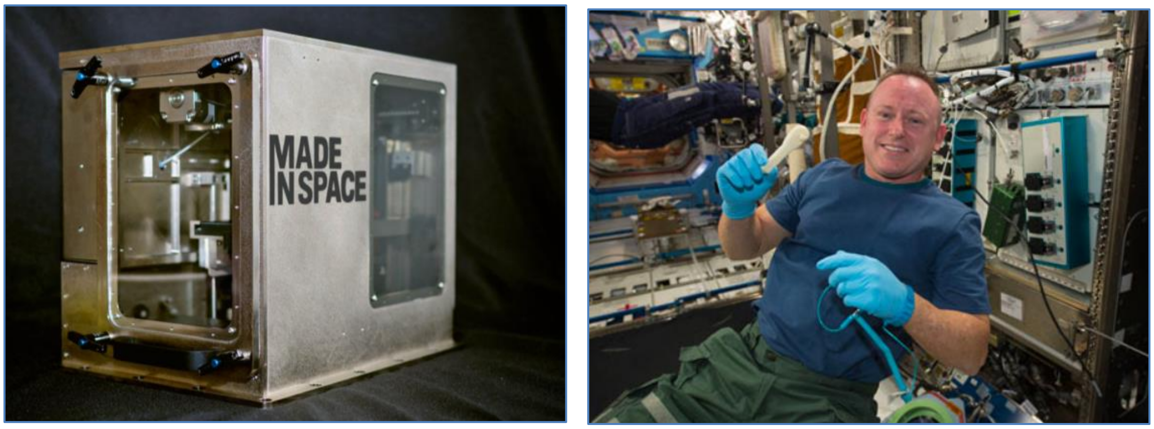

Figure 8 L: The Zero G 3D printer designed by the company Made in Space. R: The crank 3D printed in the station thanks to the Zero G printer [65].

was aboard the Cygnus spacecraft [66]. The International Space Station's (ISS) Additive Manufacturing Facility (AMF) makes use of Fused Filament Fabrication (FFF) 3D printing. A 3D item is produced using the FFF method of material extrusion printing by melting and depositing thermoplastic material layer by layer. The 3D printer is designed with a special extruder that can maintain the pressure and temperature required for extrusion in microgravity. The printer uses a closed-loop system that regulates the flow of materials and prevents it from drooping and oozing. The system consists of sensors that detect the material flow rate, pressure, and temperature, and adjust the extruder accordingly [67]. With this gadget, NASA and the US National Laboratory will be able to use the device to print components of various types from the space station, presenting an advantage for the worldwide project.

3.2 3D printing on moon

Building a base on the moon could theoretically be made much simpler by utilizing a 3D printer to construct it from the local materials [68]. The Contour Crafting technology [69] is a fast-maturing robotic building technology that offers potential for an economically viable lunar infrastructure buildup. Contour crafting is a type of 3D printing technology that is used to construct large-scale structures. It involves the use of a large-scale 3D printer that is mounted on a gantry system. The gantry is typically mounted on rails, allowing it to move along a predetermined path. The process begins with the creation of a digital model of the structure to be printed. This model is then loaded into the printer's software, which generates a set of instructions for the printer's nozzle to follow. A continuous stream of material, usually concrete or another cement-based combination, is extruded from a nozzle

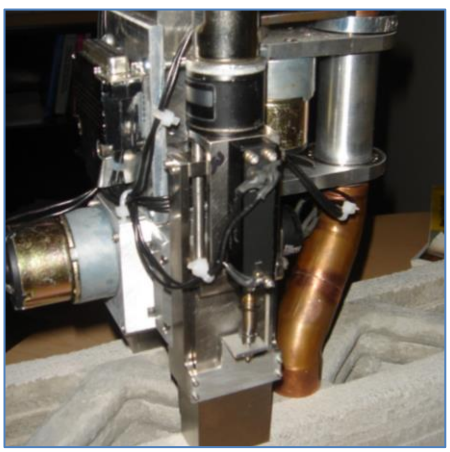

Figure 9 L: Sophisticated extrusion technology being used by Contour Crafting [49]. R: A section of the wall for the lunar base project by D-Shape [70].

as the printer moves along the gantry. A precise pattern of material is deposited by the nozzle's back-and-forth motion. Extruding the material in layers allows for top-down construction of the structure. A trowel or other instrument is used to smooth and compact each layer as it is applied. To make sure that the finished construction satisfies the required standards, the printer's software regulates the material's speed and flow rate as well as the nozzle's position [71]. It is a hybrid approach that combines an extrusion process for forming the outer rims of an object and an extrusion, pouring or injection process for filling the inner core. Once the outer rims have been formed, the inner core can be filled. One technique for filling the inner core is to employ an extruded lattice system that serves as a form of structural reinforcement [71]. The technology used in contour crafting for 3D printing is similar to FDM, but it involves layer-by-layer deposition of cement-based composites instead of filaments. This technique can be referred to as a version of FDM.

Another technology which also focuses on lunar based construction by 3D printing is D-Shape [72]. D-Shape is a large 3-dimensional printer that uses binder-jetting, a layer-by-layer printing process. Using a large gantry structure to move, the printer creates an alternative type of concrete by selectively applying a liquid binder on top of layers of powder material consisting of a cement-sand blend (sand mixture with solid magnesium oxide). Where the binder is applied, the powder material solidifies, while the remaining unbound material remains as a support for the solidified parts [70]. The process of binder jet 3D printer will require some adjustments in order to print in low gravity. This is vital since the powder could easily float away and interfere with other equipment or contaminate the environment. To address this, the printing process would need to be contained within a closed environment with a controlled atmosphere to keep the powder in place.

3.3 3D Printer design considerations and specifications

This section discusses the specifications of the proposed and designed 3D printer machine, which functions similarly to the machines currently on the market, with a few modifications to accommodate different print heads. The section describes the selection process for the 3D printer design parameters, which was based on two types of 3D printing techniques: fused deposition modelling (FDM) and selective laser melting (SLM).

As the necessity for creating a 3D printer is determined, we now need to identify and describe the functional analysis of the machine in relation to the external environment and the relationships between these elements and the system. Furthermore, since the project is conducted on Earth for lunar materials, we will add one single aspect of the element of the external lunar environment to the octopus diagram. A total of eight functional characteristics are important for the successful design and operation of the 3D printer. The very first and most important functional characteristic is the user. The user is the one deciding what part is to be printed. The print bed measurements will be the criterion for the user to print because they will limit the dimensions of the part. For our design, the print bed dimensions are 100mm in the X-axis, 100mm in the Y-axis, and 180mm in the Z-axis. Over time, the stepper motors will start to have deviations in steps from the expected positions. In general, stepper motors are known for their accuracy, with the primary source of errors associated with mechanical factors rather than the motors themselves. Typically, a 2-5% error is associated with the steps of a stepper motor [73], [74]. However, these errors can be mitigated through various techniques. Calibration, micro-stepping, using a closed feedback loop, or adjusting belt tension can help reduce inaccuracies. Manufacturers provide guidelines on belt tensioning to avoid over-tightening, which may result in skipped steps. It's worth noting that while stepper motors may experience some error over time, it doesn't significantly impact the dimensional parameters of prints, thanks to precise control at the micro-stepping level. Stepper motors have a long average lifespan, with tens of thousands of hours of continuous operation. For applications demanding higher precision, there are higher-quality stepper motors available with lower error percentages, often below 0.5%, but they tend to be more expensive. The rotational motion of a stepper motor can be converted to linear motion using a belt drive mechanism. This conversion is achieved by connecting the motor's rotating shaft to a pulley, which is typically wrapped around on one end of a belt. The other end of the belt is connected over another free moving pulley and are attached to the linear moving component, such as carriage. As the stepper motor rotates, it drives the pulley connected to the belt, causing the belt to move along its length. The linear movement of the belt is then transferred to the connected linear moving component, causing it to move in a linear direction. Here, a GT2 belt with a pitch of 2 mm and a GT2 20-tooth pulley gear is utilized. One full revolution (200 steps) will move the linear distance by 40 mm (belt pitch x pulley teeth) and 1 step of the motor will move 0.2 mm. The second functional characteristic is the computer. The computer here acts as an interface between the user and the program. The criteria for the computer system will be the computability of the system to accommodate different modules of the 3D printer. Another function will be the software or application used to run the open-source program on the computer.

The next important function of the design is the input material for 3D printing. The materials used for the trials on Earth are aluminum 6061™ filament and pellets. These are trademark products of The Virtual Foundry Company [75]. The materials are 60% to 65% metal with a binder agent, typically PLA. Post-processing is required to achieve a 90% metal product and melt the binder material. The debinding and sintering of printed parts will be carried out in a sintering furnace. The nozzle temperatures are set in the region of

205°C to 235°C. The goal is to attempt melting aluminum infused polymer filament at lower temperatures in the region of 200°C to 300°C for initial assessments. The materials used in trials are not directly linked to the materials available on the moon, and a readily available processed product on earth is used for ease and faster procurement. These materials were selected only for the trails to be carried out on earth. Since aluminum was the primary material for 3D printing, this aluminum infused polymer filament was considered. Though sintered metals have low electrical conductivity due to their porous nature and oxides forming within these pores, the level of porosity can be controlled during the sintering process. A process of infiltration can also be utilized to fill the pores with electrically conducting molten metal. This process not only provides good electrical conductivity but also properties like strength and resistance. However, the success of this process depends on the specific metals used and the conditions, like iron [76] in the case of the aluminum infiltration process. In the context of lunar resource utilization, it is worth noting the presence of water at the poles, which can potentially serve as a source of hydrogen through electrolysis. Additionally, the regolith contains a limited amount of embedded carbon in the form of volatiles such as CH4, CO2, and simple organics, although this resource is relatively scarce, measuring around 100-120 ppm by weight. Collectively, these resources offer the potential to generate syngas/water gas feedstock for polymer manufacturing, albeit in restricted quantities. A feasible alternative source of carbon is the carbonaceous (C-type) asteroids within the Near-Earth Asteroid population, accessible from lunar orbit with a relatively low delta-v. C-type asteroids predominantly consist of various carbon compounds that can undergo combustion in oxygen, yielding CO/CO2, which can further be converted to methane using hydrogen and suitable catalysts like the

Sabatier reaction. This, however, necessitates the establishment of a lunar-NEA cycling infrastructure. While the existence of buried C-type deposits on the Moon resulting from asteroid impacts remains unverified, it presents a plausible scenario supported by literature "Asteroids on the Moon: projectile survival during low velocity impacts" [77]. The option of sourcing polymer from Earth, though less ideal, is a possibility particularly envisioned for contour crafting. This method entails blending regolith with a polymer binder to 3D print outer shell structures. Exploring alternatives that eliminate the use of polymer altogether poses a significant challenge. One potential avenue is the utilization of lunar-derived glass for 3D printing, encompassing variants like lunar regolith glass, lunar basalt glass, lunar anorthite glass, and fused silica glass with added Ca and Al to reduce melting temperatures. However, it should be acknowledged that these alternatives involve higher melting points compared to polymer. For the purpose of our demonstrations, polymer has been adopted as a matrix material. It is conceivable that imported polymer, whether from C-type asteroids or Earth, could remain a crucial and indispensable component until more sustainable solutions emerge. Our current objective is to showcase the feasibility of concurrent multi-material 3D printing involving both polymer and metal within a plausible lunar context.

The lunar environment is another functional characteristic taken into account in the design of the 3D printer. The temperatures on the lunar surface can range from +123°C to -220°C [78]. An insulated chamber to maintain the temperature within the 3D printer or during 3D printing becomes necessary. Finally, the power source of heat energy and the medium to transfer the energy, which are the Fresnel lens and optical fiber, are the functional characteristics of the design. The Fresnel lens utilized may yield a focal point temperature of 920°C. The optical cable will be utilized to deliver this thermal energy from the Fresnel lens to the 3D printer.

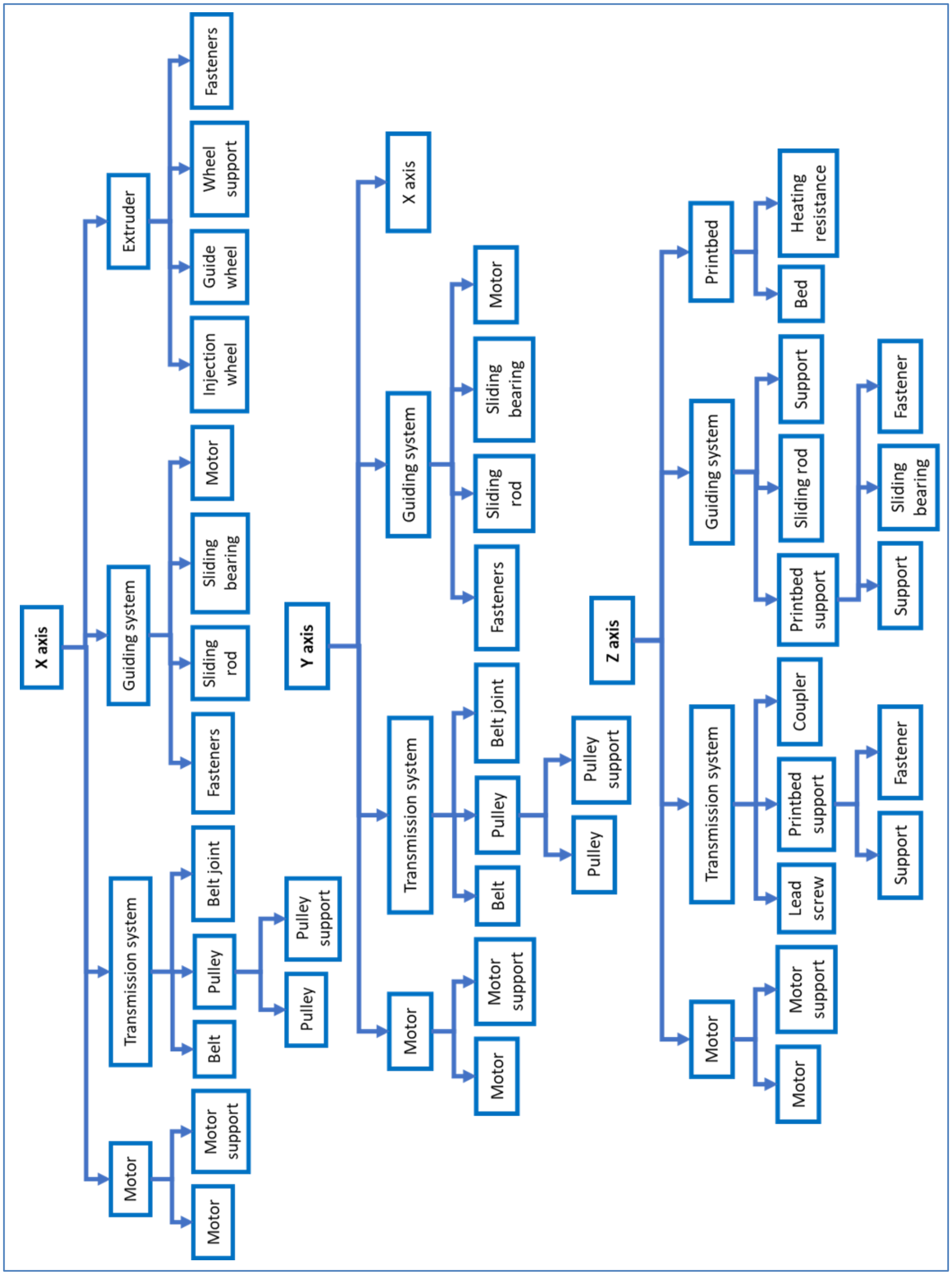

Figure 10 3D printer axes nomenclature

3.3.1 3D Printer axes nomenclature

In order to plan the machine's design, the numerous components installed on the X, Y, and Z axes are listed below and are represented in figure 10. This information also allows us to construct the machine in CAD software, determining if the various components will be purchased, manufactured, or retrieved from the prior setup. The x-axis governs the motor system, transmission system, guiding system, and extruder system. The motor and motor support constitute the motor for the x-axis. The transmission system includes the belt, pulley, and pulley support with belt joint. The fasteners, sliding rods, sliding bearings, and the axis motor are the guiding system on the x-axis. Finally, the injection wheel, guide wheel and wheel support with fasteners complete the extruder system for X-axis. The same systems are used for the motor, transmission, and guiding system, with the entire X-axis serving as one portion of the Y-axis. The transmission system for the Z-axis differs from the X-Y-axis in that a lead screw and couplers are used to help lower the heated bed for printing. In addition to the print bed, the guiding system makes use of comparable sliding rods and bearings.

3.3.2 Existing system

In the year 2017/2018, a batch of undergraduate and graduate students worked on a similar-scoped project where they designed and constructed a 3D printing machine. My research was conducted using the same framework as the earlier student's project. The following images illustrate the state of the printer when the previously built 3D printing machine was handed over to me. This is a Cartesian-style 3D printer machine. As seen in the image, the printer had X- and Y-axes defined with the required sliding mechanism, but the Z-axis (print bed) disintegrated. Along with this, the respective axis stepper motors were present with housing brackets that were 3D printed. Aluminum extruded profiles were used for the framework, with an attachment bracket on the corners. The electronic components of the printer were disconnected, but all the instruments were present in the lab. The following table 3 illustrates the useful components recovered from the old printer machine::

Component	Specification	Quantity
Aluminum extruded profile	50mm x 50mm x 450mm	4
Aluminum extruded profile	50mm x 50mm x 200mm	4
Aluminum extruded profile	50mm x 50mm x 360mm	2
Stepper motor	NEMA 17 Bi-polar 12V 0.4A	5
Sliding bearing	Diameter 8mm	4
Sliding bearing	Diameter 16mm	6
Sliding axis rod	Diameter 8mm, length 300mm	4
Sliding axis rod	Diameter 16mm, length 300mm	4
Lead screw	Diameter 8mm, length 250mm	2
Lead screw nut	Diameter 8mm	2
Lead screw coupling nut	Diameter 8mm	2
Printbed support clamps	3D printed parts	4
Timing belt	20 teeth x 900mm	2
Pulley gear	GT2 pulley with 20 teeth	4
Mechanical end switch	Longrunner with 22AWG cable	3
Sliding rod guide	Diameter 8mm	8
Jumper wires	Male to female	10

Table 3 Recovered component part list.

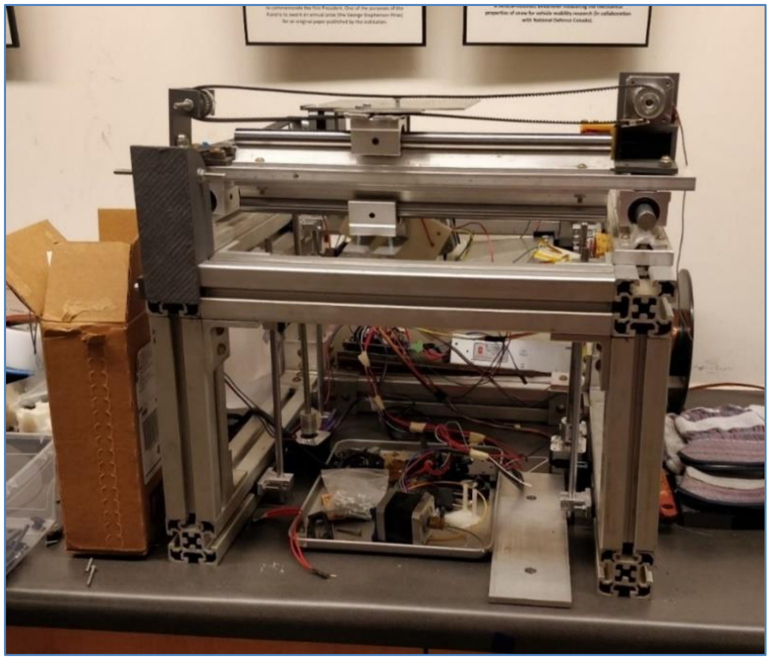

Figure 11   Old 3D printer system frame

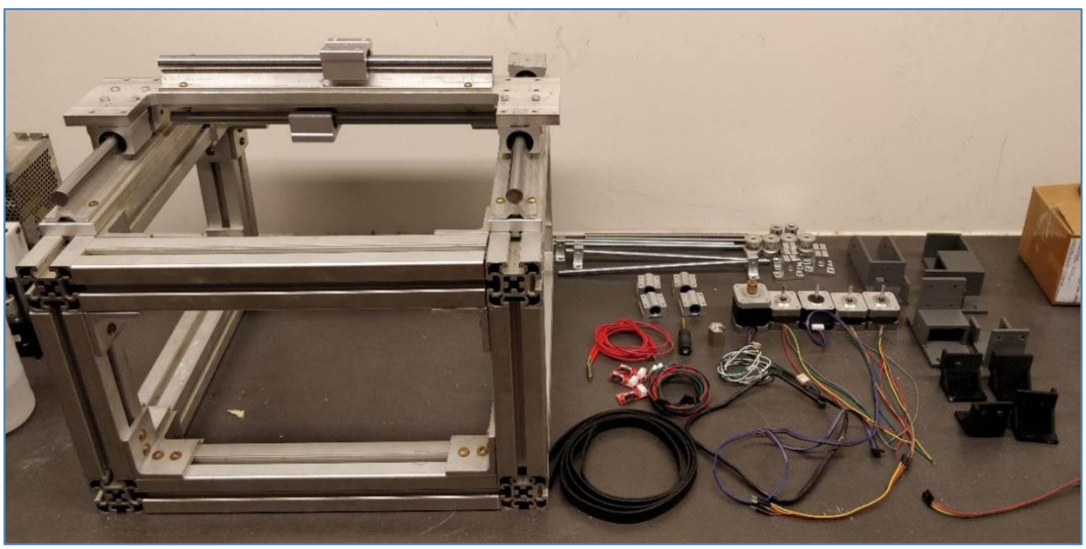

Figure 12   Recovered component parts with 3D printer frame

3.3.3 CAD design

The computer-aided design file of the previous system was not present, hence the usage of CAD software CREO 7.0 was used to create the existing model. The CAD file was made by first measuring the existing system and then drawing it in the software. Figure 11 depicts the design of the present systems' frame and sliding mechanism.

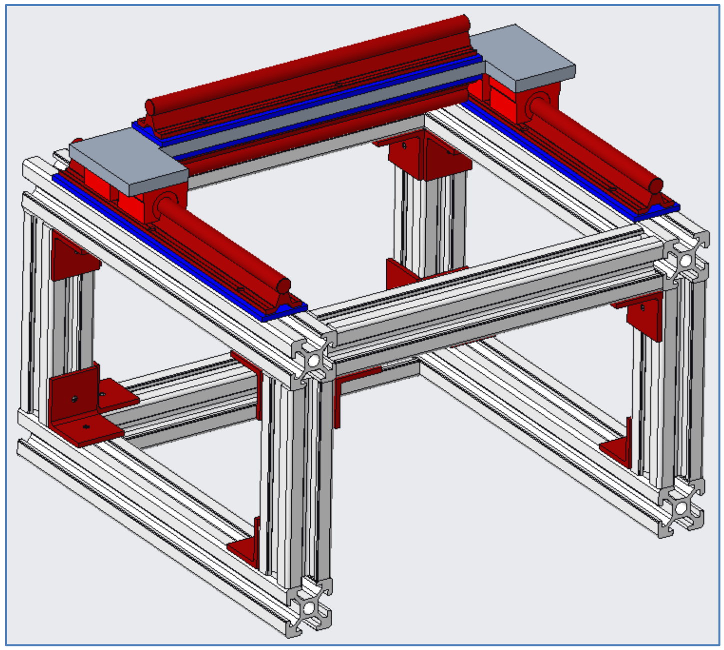

Figure 13 CAD design for the old frame

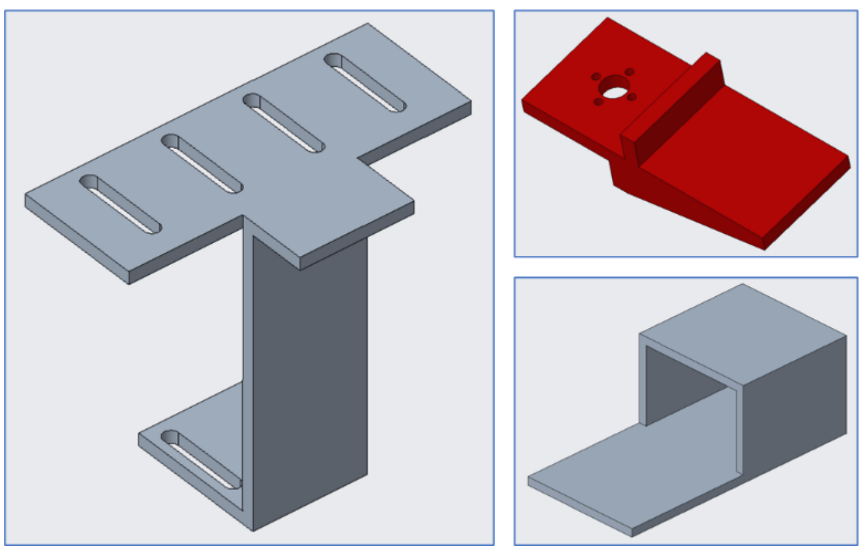

Figure 14 CAD design for new 3D printed parts

In addition to designing the model, we also designed the 3D-printed parts. A 3D printing service was available at the university library. The parts designed for 3D printing are shown above. The 3D printed parts were printed using PETG (Polyethylene Terephthalate Glycol) material. The PETG material is the most common thermoplastic polymer resin of the polyester family. PETG has lower water absorption ability and is selfextinguishing in nature. The refractive index of clear-transparent PETG typically ranges from 1.57 to 1.65 is known to have poor resistance to ultraviolet light [79]. PETG also exhibits excellent mechanical properties, creep resistance, fatigue resistance, friction resistance and dimensional stability over a wide variety of temperature ranges [80], [81].

3.3.4 Subsystem assembly

As the individual components of the final assembly were gathered, the assembly procedure was started one by one. We began constructing them according to the axes nomenclature to make the assembly easier and more efficient.

3.3.4.1 X-axis assembly

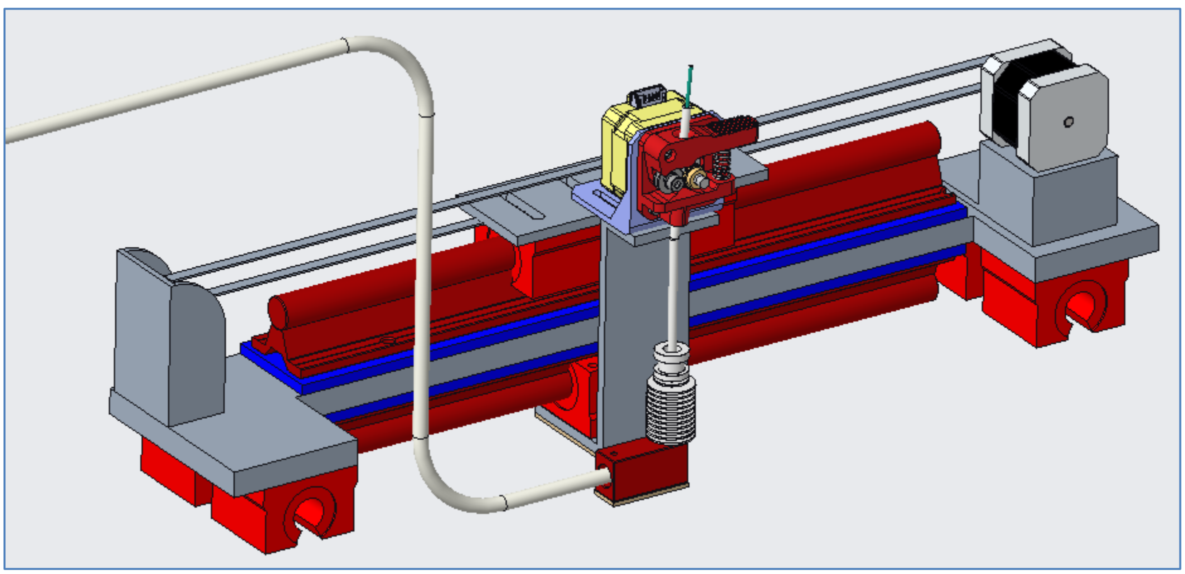

Figure 15 X-axis sub-assembly

On this axis, the print head assembly is mounted. The print head module movement across the axis is aided by one stepper motor of the order 1/16 steps and timing belt pulley system. The timing belt pulley system is affixed on the two-sliding contact bearing (16mm–one on top and one on bottom), which compels the movement of the extruder assembly with unanimous and smooth running. The print head motor assembly is mounted on a bracket that holds the timing belt pulley and 2 sliding bearings in position. This ensures the smooth movement of the extruder motor along the axis. The axis sliding bearing also holds an end stops limiter. The rotational motion of the motor is translated to linear motion with the help of a pulley and timing belt.

3.3.4.2 Print head nozzle

Two design options were considered based on the type of input raw material: (i) aluminum extrusion by a process similar to FDM (refer to Appendix B1), but this was considered not feasible. The melting temperature of aluminum is significantly higher compared to the typical operating temperature range of FDM printers. Aluminum has a melting point of around 660°C, while most FDM printers are designed to work with lower melting point thermoplastics like PLA or ABS, which melt at temperatures below 250°C. The high melting temperature of aluminum would require specialized extrusion systems and components capable of withstanding and controlling such extreme temperatures, which are not commonly available in standard FDM printers. Aluminum exhibits poor thermal properties for the FDM process. It has high thermal conductivity, which means that heat dissipates quickly, making it difficult to maintain a consistent molten state throughout the extrusion process. FDM relies on the controlled heating and cooling of the filament to ensure proper deposition and layer bonding, but with aluminum, it becomes challenging to maintain the required temperature gradient for successful extrusion. Additionally, aluminum extrusion requires a controlled and precise flow of molten metal, which is difficult to achieve with the nozzle and extrusion mechanisms typically used in FDM printers. Aluminum has different flow characteristics compared to thermoplastic filaments, making it challenging to achieve accurate and reliable extrusion. (ii) aluminum powder bed (similar to SLS or SLM), where the printhead consists of optical fiber and focuses the solar radiation rather than the laser and inscribes the bed. This approach offers advantages over traditional SLS or SLM techniques. Firstly, it reduces the cost of production, as optical fiber is cheaper to maintain than a laser. Secondly, it is more sustainable as solar energy is used instead of electricity. Thirdly, it offers greater flexibility in terms of the shape and size of the inscribed objects, as the optical fiber can be more precisely controlled than a laser. Additionally, optical fibers do not have moving parts like laser systems, which reduces the likelihood of mechanical failures and breakdowns. In order to ensure a successful 3D printing process, it is crucial to prioritize the design of the optic fiber printhead before moving onto the design of the powder bed. The printhead is responsible for focusing the solar energy to inscribe the aluminum powder bed and thus plays a critical role in the final quality and accuracy of the printed object. By focusing on the printhead design first, any potential issues or limitations can be identified and addressed early on in the design process, ultimately leading to a more efficient and effective 3D printing system. Therefore, it is essential to prioritize the design of the optic fiber-based printhead before proceeding with any of the proposed designs.

3.3.4.3 Y-axis assembly

The assembled plate of the X-axis is mounted on this axis. Along with the plate, the axis has two sliding contact bearings on each side, as well as a bracket on one side to mount the stepper motor with 1/16 step resolution and a timing belt pulley on the other. The sliding contact bearings are located beneath the X-axis plate, together with an end stop limiter. The primary role of the Y-axis is to carry the described X-axis assembly in a perpendicular direction to that of the X-axis. The rotational motion of the motor is translated to linear motion with the help of a pulley and timing belt.

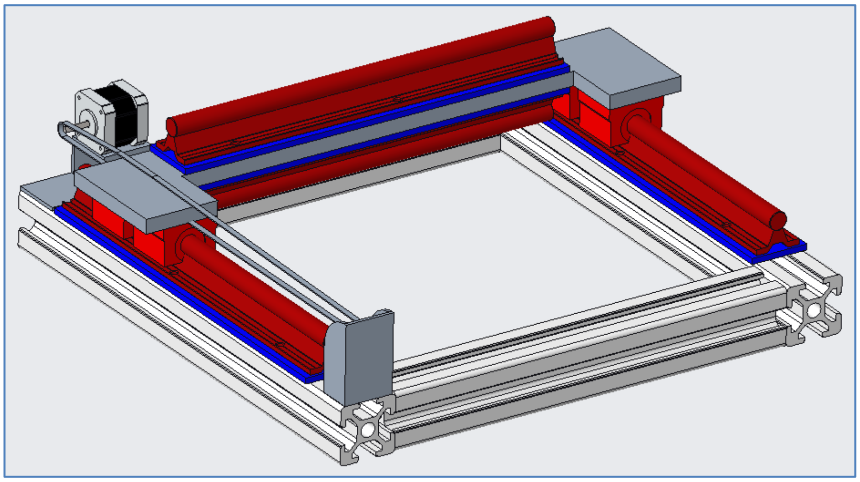

Figure 16 Y-axis sub assembly

3.3.4.4 Z-axis assembly

On this axis, the print bed of the printer is mounted. Unlike the X-axis and Y-axis whose movement are restricted to just sliding back and forth at one defined height, the movement along of Z-axis is defined to lift the print bed up and down by 0.1mm. End stops are used on 3D printers frame to set the starting position of the Z-axis. When the printer homes, the end stop is triggered, which signals the printer that the Z-axis is at its lowest point. This position is then set as the reference point for the Z-axis. Before printing, the printer will move the Z-axis up until it reaches the desired starting height, which is usually just above the build platform. This ensures that the printer starts printing at a consistent height and that the print adheres properly to the build platform. Then as the printing progresses, the bed moves down by 0.1mm.

The above schematic displays the Z-axis assembly, which include two stepper motors, two lead screws assembled at the end of stepper motors, four sliding guides, four sliding contact bearing (8mm), a print bed and an end stops limiter. The rotational motion of the motor is translated to linear motion with the help of a lead screw and lead screw nut.

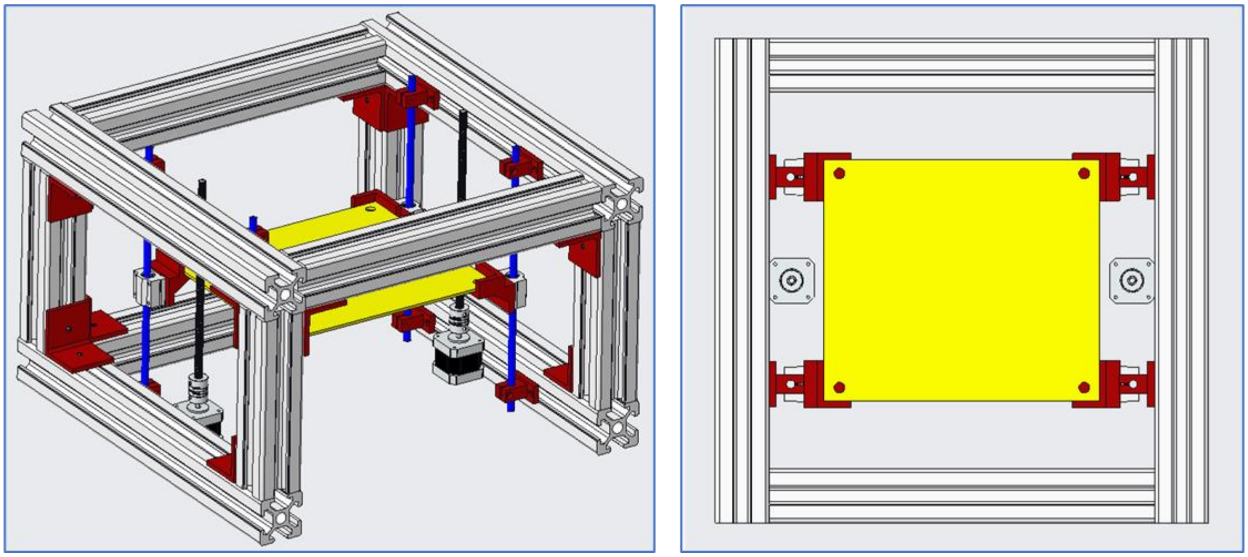

Figure 17 Z-axis sub assembly

3.3.5 Design assembly

The general design of the 3D printing machine required numerous iterations due to the need for synchronous integration of new parts and systems into existing parts and systems. Figure 19 illustrates the final assembly of the printing machine.

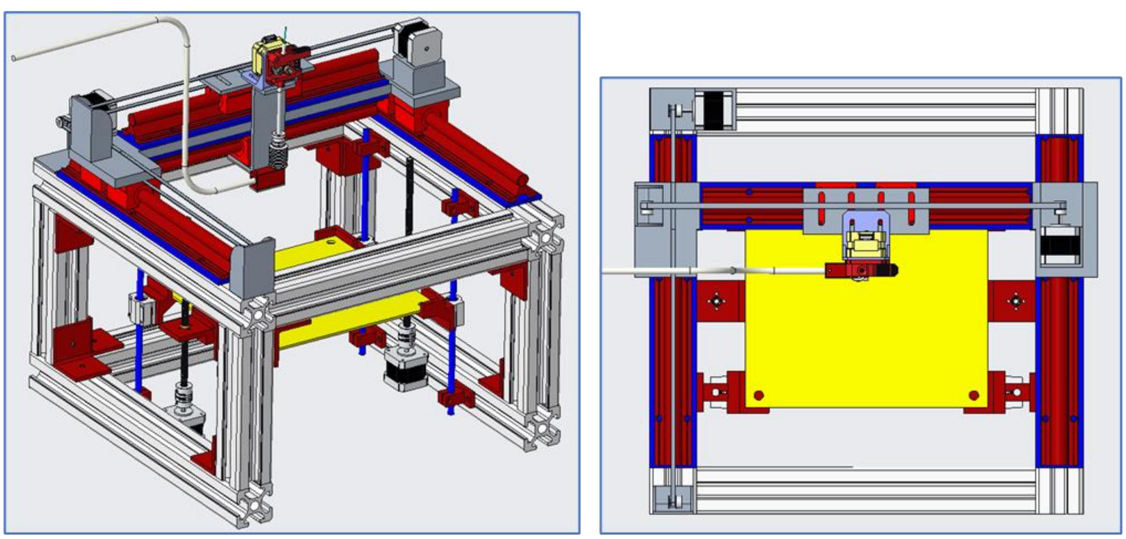

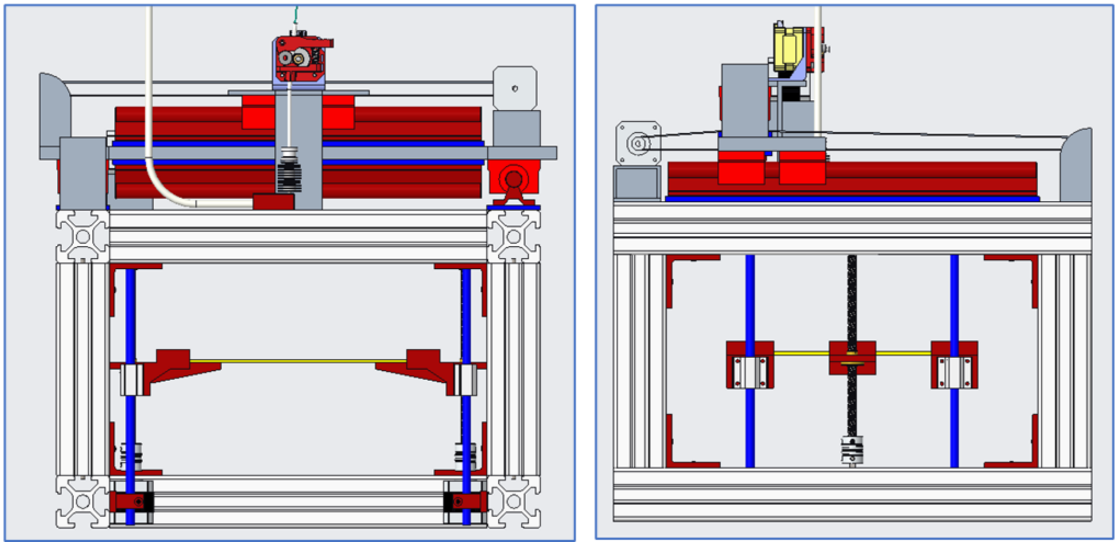

Figure 18   Final assembly CAD representation

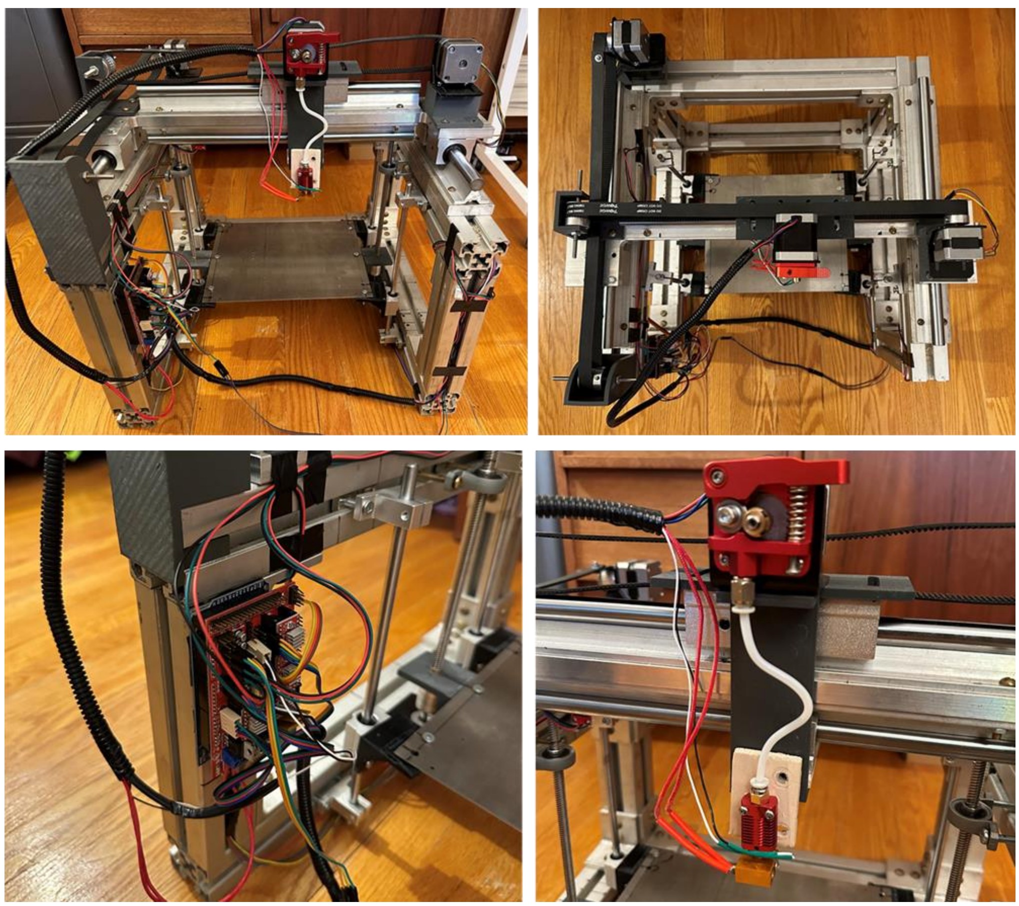

Figure 19   Final assembly representation

3.3.6 Electronic components

The electronic components of the printer are termed the 'brain' of a machine. It is the communication link between programmed signals and functional output. Electronic components are used for controlling the stepper motors, calculating the trajectories, altering the temperatures and translating the G-codes. An overview of the electronic nomenclature is showcased in figure 20 for the designed 3D printer.

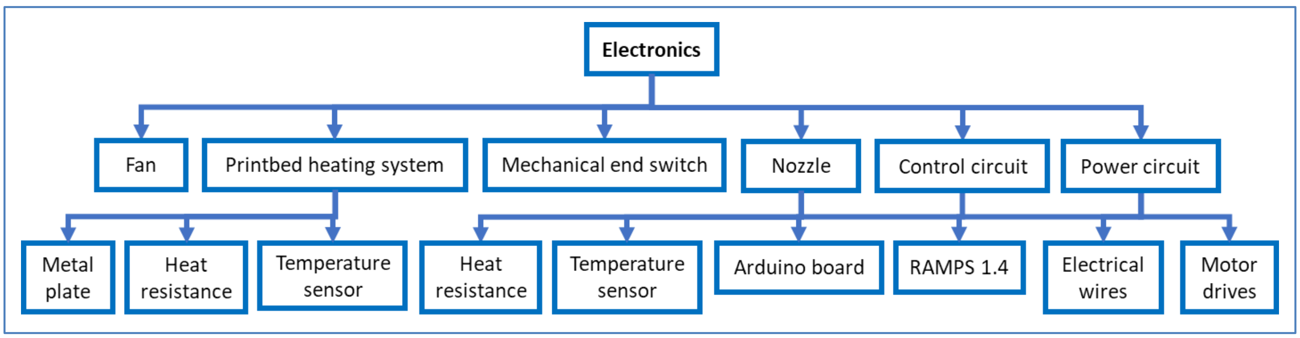

Figure 20 Electronics nomenclature for 3D printer

3.3.6.1 Stepper motors

A DC stepper motor NEMA 17, bipolar 12V 0.48A is used in the 3D printing machine. All the motors were recovered from the old model. The design of the motor includes a stationary part called a stator, which are circular coils, and the moving part is called as rotor, which is a magnet. The NEMA 17 stepper motors are precision motors and perform 1.8° per steps. Thus, a total of 200 steps in complete revolution is observed (360°/1.8° = 200). With a TR8x8-200mm lead screw, the platform will advance 8mm in one rotation. Thus, a minimum thickness of 0.04mm can be achieved with this stepper motor. For our thesis project, the layer thickness is set to 0.2mm.

3.3.6.2 Stepper motor drivers

A micro-stepping motor driver A4988 is used to translate easy movement of the stepper motors. These drives support full, half, quarter, eight, and sixteenth step modes. The function of the driver is to control current flowing through the stepper motor coils by regulating the voltage across a sense resistor in series with motor. The driver also determines the sequence in which the motor coils are energized to produce the motion. Finally, the A4988 drivers have built-in over temperature protection, which shuts down the driver if the temperature exceeds a certain threshold. A heatsink is installed on top of the drivers for better heat dissipation.

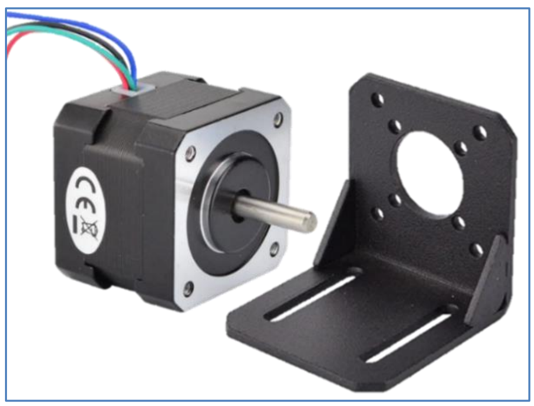

Figure 21 NEMA 17 stepper motor with mounting bracket

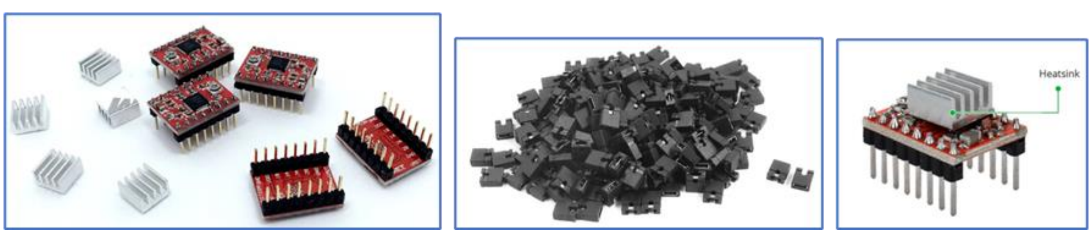

Figure 22 Stepper motor driver A4988 with jumper wires and heatsink [82]

3.3.6.3 End stops

These are the sensors used to limit the travel distance of the motors on the respective axes. So, three end stops were installed on each axis. The operation of the end stops is similar to a push button. On activating the switch, the signals are sent to the motor to at once stop. The end stops are used to identify the home positions (0,0,0) of the X, Y and Z-axes.

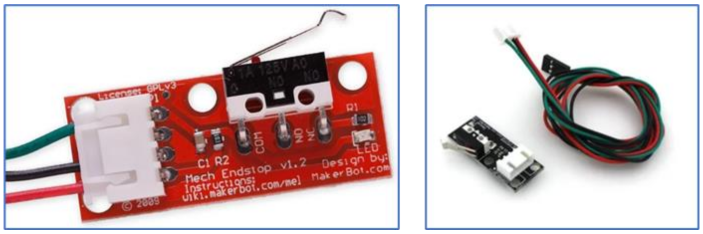

Figure 23 End stop switch with three wire terminal [82]

3.3.6.4 Microprocessor / Microcontroller board

A controller board is installed in the printer to control the different electronic components. The Arduino Mega 2560 board is used. This is an ATmega2560-based microcontroller with 54 digital I/O pins. Connecting the controller to the PC through a USB cable powers it. It also supports a variety of shields and motherboards to excel in diverse operations.

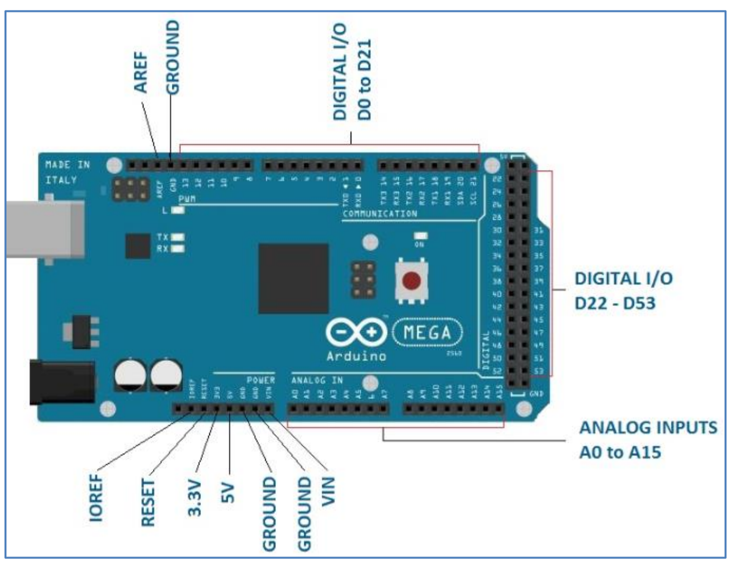

Figure 24 Arduino Mega 2560 with pin description [83]

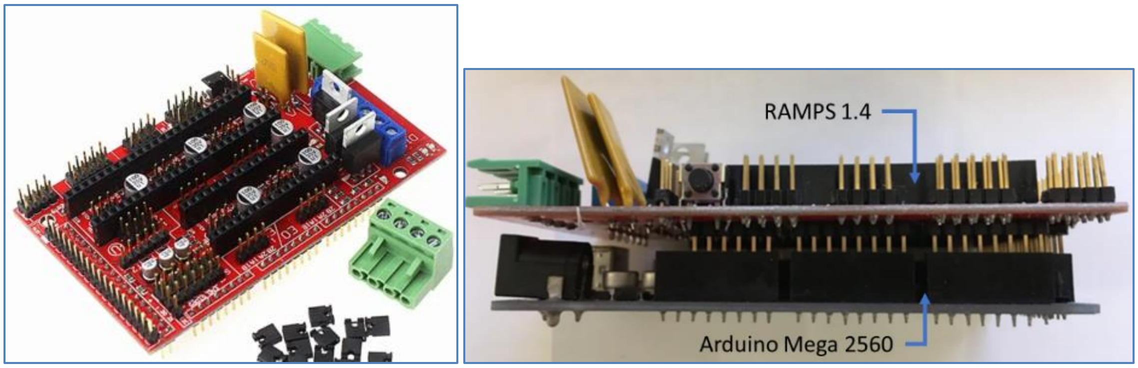

Figure 25 RAMPS 1.4 over Arduino Mega 2560 board [82]

3.3.6.5 Motherboard

RepRap Arduino Mega Polulu Shield or RAMPS is a board that serves as the interface between the Arduino Mega and the electronic components. The RAMPS board aids in the translation of information from computer program code to digital signals for electronic components. The RAMPS 1.4 version is used in the design.

3.3.6.6 Power unit supply

To power the five motors, its drivers and the mother board RAMPS 1.4, a power supply of 12V 5A is required. This will be an external source of power unit. Though the goal of the project is to create 3D prints without electricity on lunar surface, this small amount of power can be generated using solar panels.

Figure 26 External power supply unit of 12V-5A

3.3.7 Electronic circuitry assembly

For the printer machine to perform efficiently and correctly, all the electronic components should be configured effectively. The following figure 27 illustrates the wiring diagram for RAMPS 1.4 describing which electronic part wire should be connected to where on the board. This board is then connected to the Arduino Mega 2560.

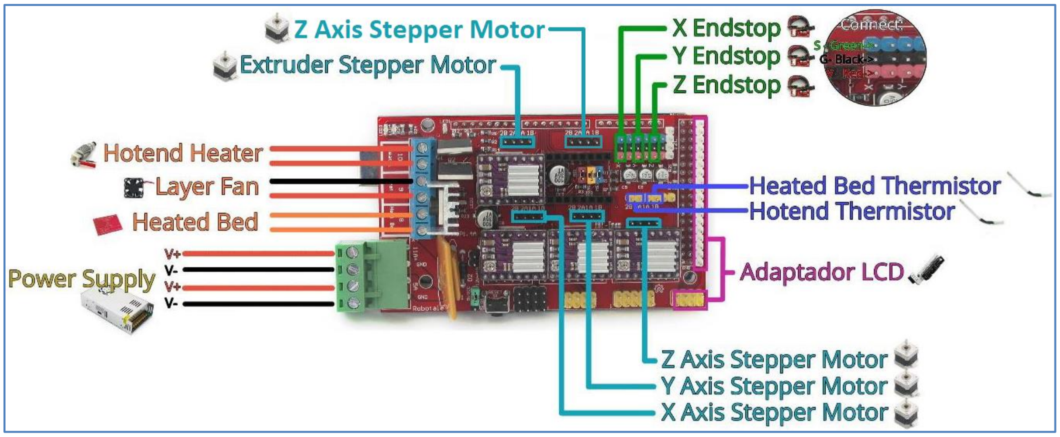

Figure 27 RAMPS 1.4 pin assembly configuration [84]

3.3.7.1 Stepper motors

The X and Y-axis stepper motor connections are mentioned in figure 28. The connection order must be in the same order as the RAMPS have defined them in this specific manner. The X-axis means the motor on the printer that will travel from left to right and the Y-axis means the motor will travel from front to back. The connections can be reorganized but similar changes should be made to the program code. For the Z-axis, there are two slots for motor input. However, for our design, we used one of the slots for the Z-axis motor. The reason is that the stepper motor driver A4988 for the Z-axis is not able to sustain the load of two motors. Since there are a total of 5 slots for motor connections on RAMPS 1.4, we will use the vacant slot for the other Z-axis motor.

Remember, the two Z-axis motors need to be synchronous. These constraints can be successfully made in the program code.

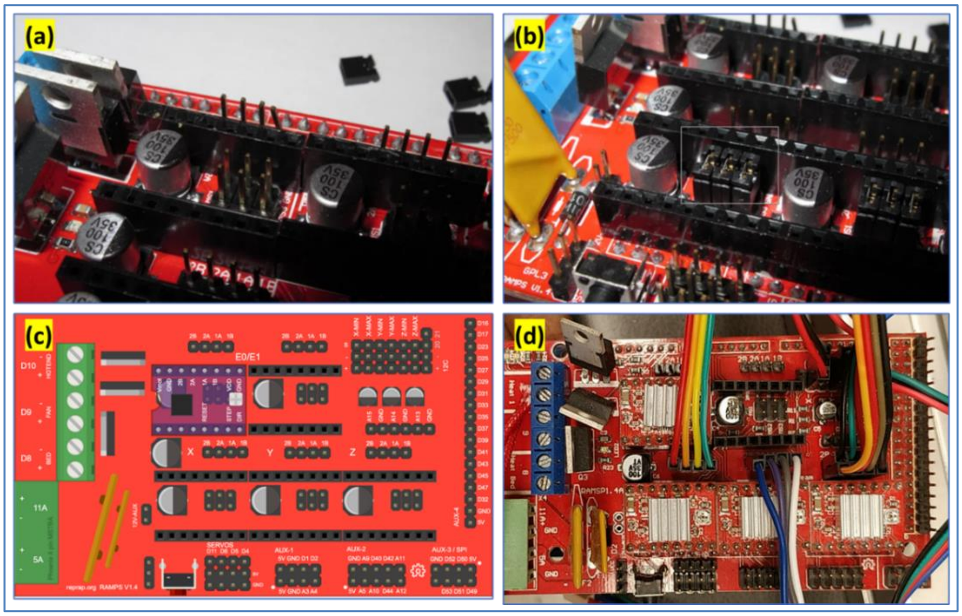

Figure 28 (a) Slot for jumper wires (b) Jumper wires installed (c) Driver A4988 installed over jumper wires (d) Final arrangement with everything assembled [85]

The following steps are involved in connecting the stepper motor drivers and the motor pins. 1) Connect the internally marked pins with three jumper wires (small black clips). This will ensure the stepper motor will have 1/16th micro stepping. Each driver will have three jumpers. 2) Insert the driver in the designated slot. There is also a small potentiometer (screw) on the top. Always position the potentiometer away from the power supply connection as shown in the image. 3) Insert the motor pins in the slot present next to the driver. There are four pins – 1B, 1A, 2A and 2B. Ensure correct motor wires are connected to the pins. An incorrect connection will distort the rotation of the motor and will not spin effectively. The wire colors on the motor vary on different motors. So the general thumb rule to follow is to measure the resistance between the pairs of wire until you find the lowest resistance pair. This pair will be your first and last wire. The direction of the motor rotation will be decided on this pairs connection and can be reversed by interchanging the respective positions.

3.3.7.2 End stops

The RAMPS 1.4 board comes with six settings for end stops. You can configure as needed and use three end stops for each axis. The pin arrangements of the RAMPS are depicted in Figure 29. The pins highlighted are the respective minimum limit pins i.e., X-min, Y-min, and Z-min. It also consists of maximum position limits for situation were

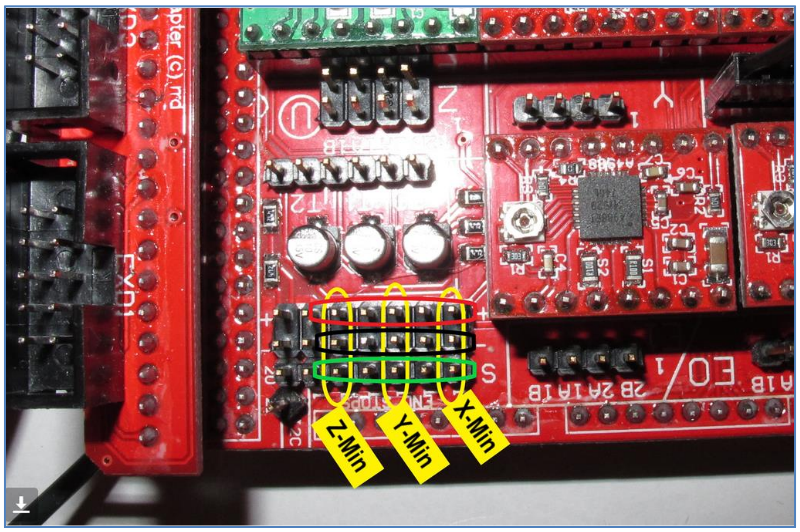

Figure 29 End stop pin connection guide on RAMPS 1.4 [82]

you do not want your bed to go beyond the distance. For example, if you want to restrict your bed from traveling beyond 100mm, set the max limit as 100mm. The minimal positions pin configuration aids in determining the home position of the bed and print head, i.e., the print head's beginning point on the bed (0,0,0 on the coordinate system). Figure 29 depicts the orientation of pin implantation. To make the switch operate, the connection must be done in the same manner.

3.3.8 3D printing software configuration

With the help of a few operating software's, the 3D printer can be configured effectively to perform the required tasks. The process flow of the software side of the 3D printing process is mentioned in figure 30.

3.3.8.1 3D model

The use of CREO 7.0 was made to create the desired 3D model. The model was simple and only used to demonstrate the printing capability of the machine as highlighted in figure 31.

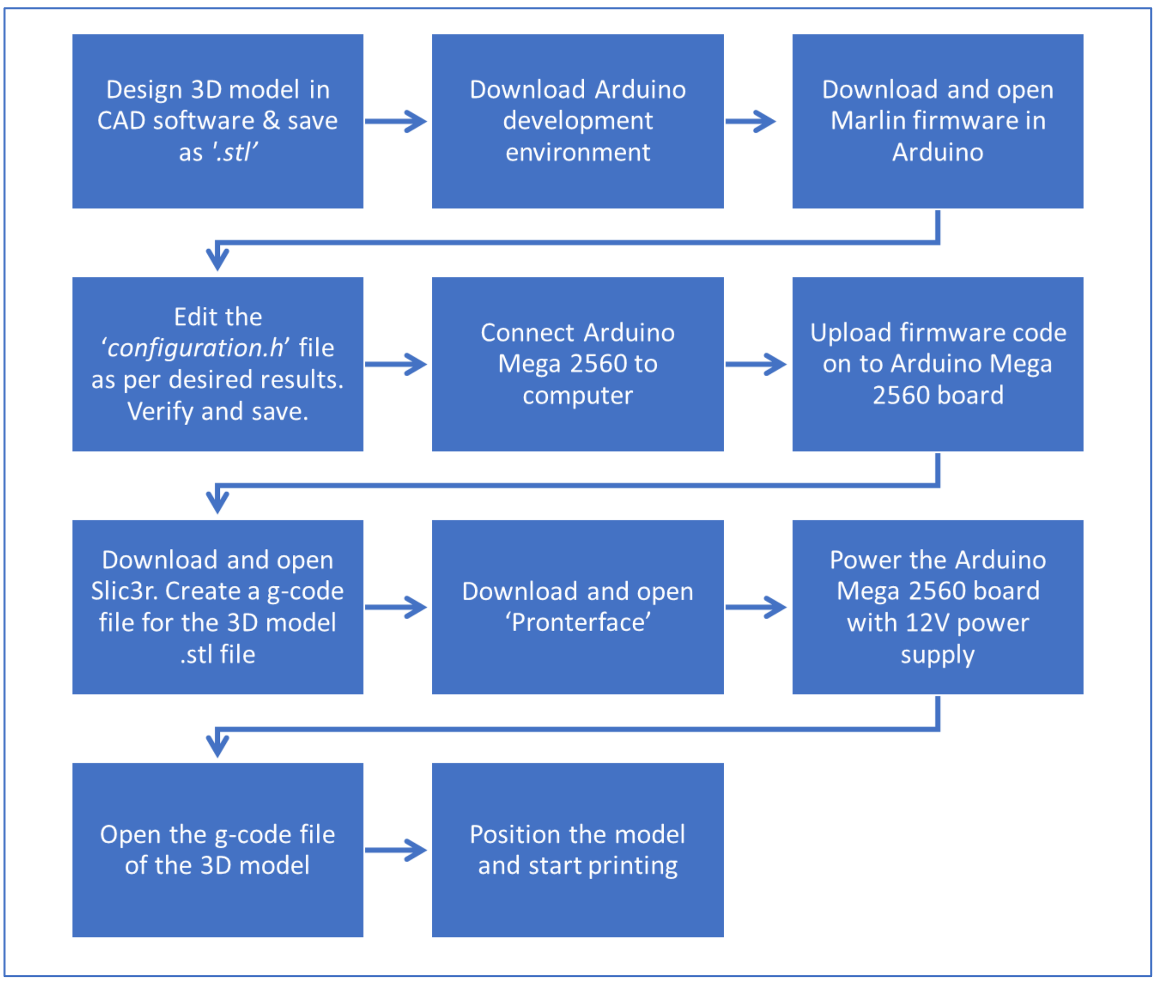

Figure 30 Flow chart for 3D printing process

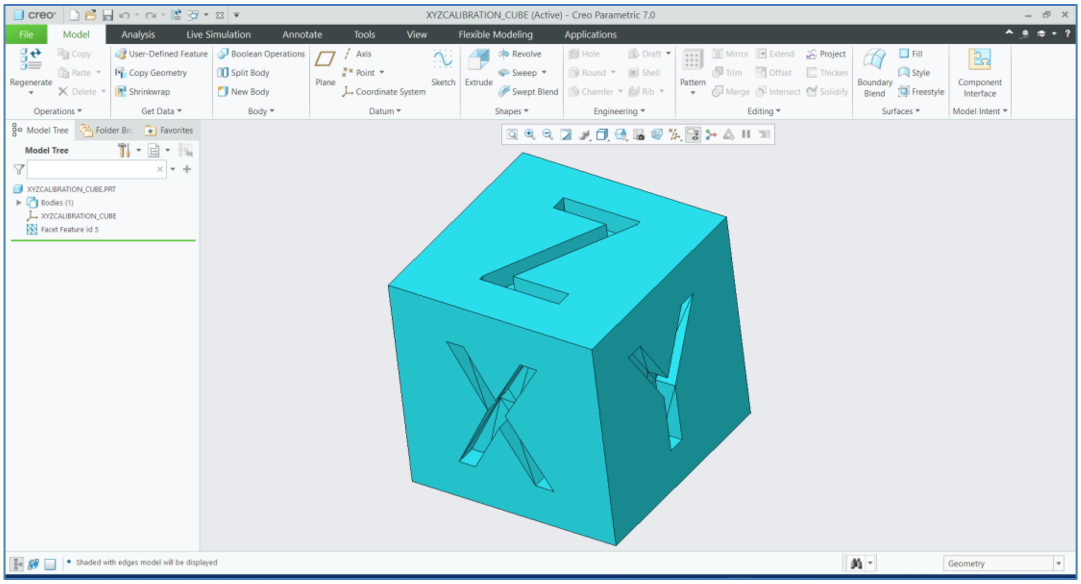

Figure 31 CAD model in .stl from CREO 7 software

3.3.8.2 Arduino development environment

The Arduino Integrated Development Environment - or Arduino Software (IDE) - contains a text editor for writing code, a message area, a text console, a toolbar with buttons for common functions and a series of menus. It connects to the Arduino hardware to upload applications and communicate with them. Install the 'Arduino AVR Boards' package driver as the Arduino Mega 2560 board is utilized in the project [86].

3.3.8.3 Marlin firmware

Marlin is an open-source firmware for the RepRap family of replicating rapid prototypes. Marlin is free and open-source software released under the GPLv3. Marlin 2.1.1 is the latest open-source firmware offered by the manufacturing community. Marlin firmware is reliable, precise and delivers outstanding print quality while keeping full control of the process [87]. Since the Marlin firmware is for standard 3D printing size, we must customize a few commands in the code so that it accommodates the changes. Following are the changes needed to be updated in the code under ‘Configuration.h’ tab

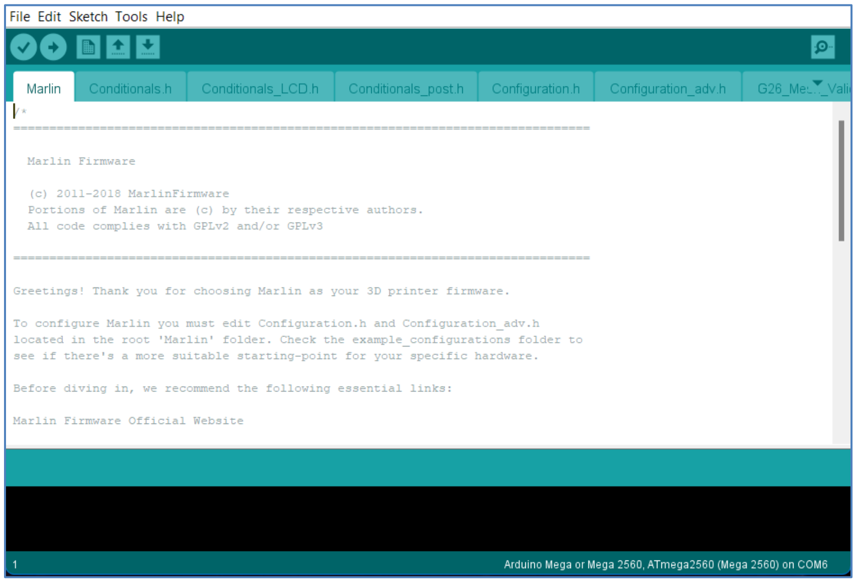

Figure 32 Interface of Arduino development environment

(a) <u>Line #126 – rate at which information is transferred into communication channel</u>

#define BAUDRATE 250000

(b) <u>Line #139 – Machine name</u>

//#define CUSTOM_MACHINE_NAME "RG-Thesis"

(c) <u>Line 510 – End stop settings</u>

#define USE_XMIN_PLUG

#define USE_YMIN_PLUG

#define USE_ZMIN_PLUG … (Remove the // to make the statement active)

(d) <u>Line 531 – End stop status</u>

#define X_MIN_ENDSTOP_INVERTING true

#define Y_MIN_ENDSTOP_INVERTING true

#define Z_MIN_ENDSTOP_INVERTING true

(e) <u>Line 553 – Stepper drivers</u>

#define X_DRIVER_TYPE A4988

#define Y_DRIVER_TYPE A4988

#define Z_DRIVER_TYPE A4988

#define E0_DRIVER_TYPE A4988

#define E1_DRIVER_TYPE A4988   … (Remove the // to make the statement active)

(f) <u>Line 879 – Size of print bed</u>

#define X_BED_SIZE 100

#define Y_BED_SIZE 100

(g) <u>Line 883 – Travel limits after homing, corresponding to end stops</u>

#define X_MIN_POS 0

#define Y_MIN_POS 0

#define Z_MIN_POS 0

#define X_MAX_POS X_BED_SIZE

#define Y_MAX_POS Y_BED_SIZE

#define Z_MAX_POS 200

Following are the changes needed to be updated in the code under ‘Configuration_adv.h’ tab

(a) <u>Line 325 – Z axis dual stepper motor</u>

#define Z_DUAL_STEPPER_DRIVERS … (Remove the // to make the statement active)

Verify the code with the above-mentioned modifications. Make sure the Arduino is connected to the computer using the USB cable before verifying and uploading the code on the board.

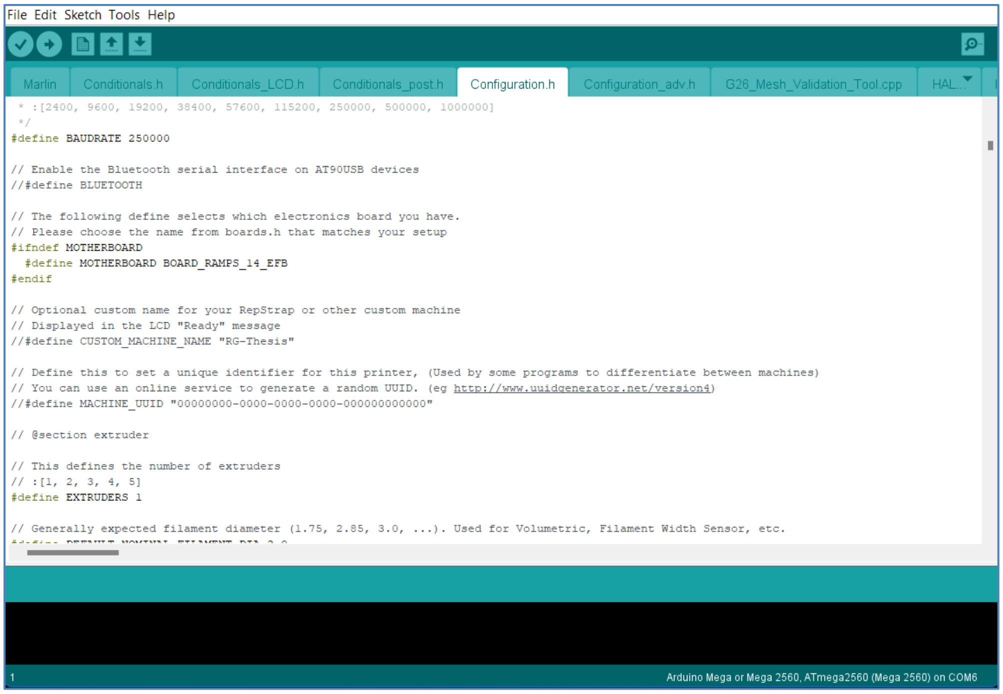

Figure 33   Interface of ADE with Marlin 2.1.1 firmware

3.3.8.4 Slic3r

Slic3r is a tool used to convert a 3D model into printing instructions for your 3D printer. It cuts the model into horizontal slices (layers), generates toolpaths to fill them and calculates the amount of material to be extruded. Slic3r project is also developed within the RepRap community. Some of the features also available with the tool are G-code generation, conversion between STL-OBJ-AMF-POV formats, auto-repair of manifold meshes, etc. [88]. The "Manifold Mesh" feature is used to check whether a 3D model is "watertight" or "manifold". A manifold mesh is a mesh that has no holes or gaps in its surface and is "water-tight" in the sense that it can hold water without leaking. If the model has any non-manifold features, such as holes, overlapping surfaces, or self-intersecting geometry, it can cause issues during slicing and printing. Slicer software for 3D printing transforms a set of inputs into a format of G-codes that the 3D printer can comprehend and optimize. The slicer receives all the data for a 3D printer, including material parameters,

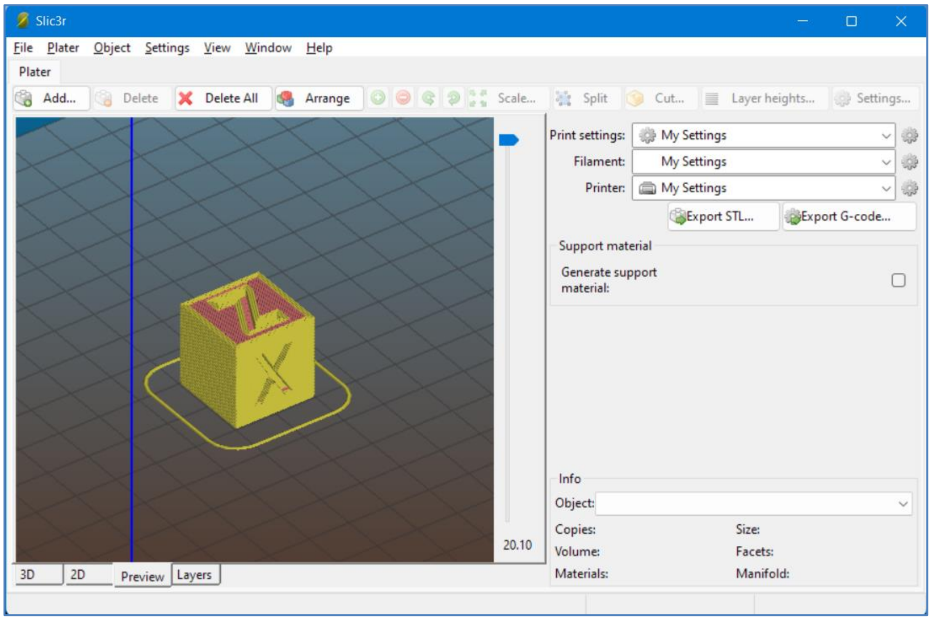

Figure 34 Interface of Slic3r software

layer heights, and extrusion types. The slicer then imports the digital model. The developed model can be represented in a variety of file formats, .STL in our case, but may vary depending on the CAD software used. The app also offers scaling and alignment settings. The models can be manufactured in smaller or larger sizes because of these characteristics. The slicer is now prepared to calculate and separate the digital component into 2D layers.

3.3.8.5 Pronterface

Pronterface is free, open-sourced software licensed under the GNU (General Public License-version 3). Pronterface is a fully complete GUI host with numerous options such as temperature gauges or graphs, full calibration controls or lightweight ones for everyday use, 2D or 3D viewer, tabbed or single window interface, and many more [89]. The program has a basic-looking design with bare minimum graphics. At this point, there are a few setup and configuration tasks to finish. First, select the port to which the printer is connected. On Windows, this will look like COM3. Next, examine the communication speed. The recommended setting is normally 250000, but different printers may require different settings. Click on connect to confirm that Pronterface and 3D printer are interacting. Next, the core controls and issue G-code commands will be available for usage. Few of the features and functions from the Pronterface software are provided below:

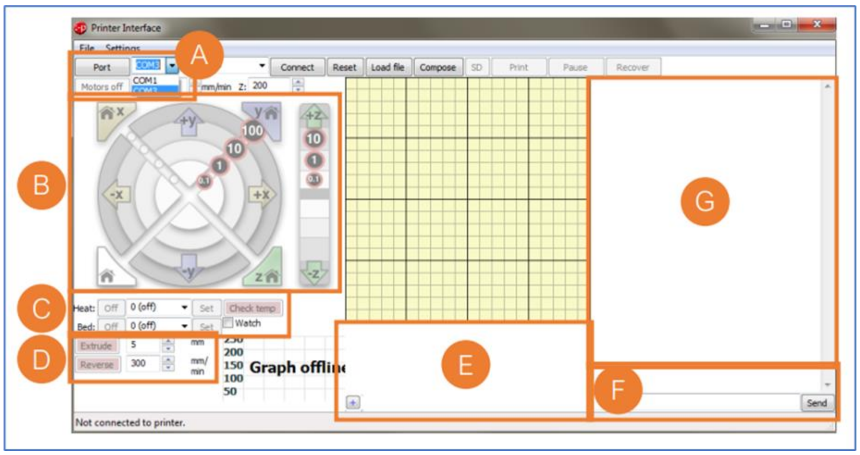

Legends	Function stamp
A	Port selection
B	X,Y, Z control panel
C	Heater control
D	Extruder control
E	Custom button area
F	Command line
G	Command window

Figure 35 Interface of Pronterface software

Chapter 4: Fresnel lens, Optic fiber, and the test setup

To focus and concentrate the solar radiation on to the optical fiber, the Fresnel lens was used. The lens takes in a large area of sunlight and directs it towards a spot by bending and focusing the light rays. The principle is similar to using a magnifying lens to focus the sun rays to start a fire. The Fresnel lens consist of a series of grooves etched into plastic. They are generally thin, lightweight, and available in a variety of sizes ranging from small to large. Assorted sizes are available due to their excellent sunlight gathering ability, which aids various applications in many different fields.

The Fresnel lens reduces the amount of material required compared to a conventional lens by dividing the lens into a set of concentric annular sections. An ideal Fresnel lens will have an infinite number of sections. In each section, the overall thickness decreases. This effectively separates the continuous surface of a typical lens into a group of identical curvatures separated by stepwise discontinuities. This allows the light to bend and follow a common focal length [90].

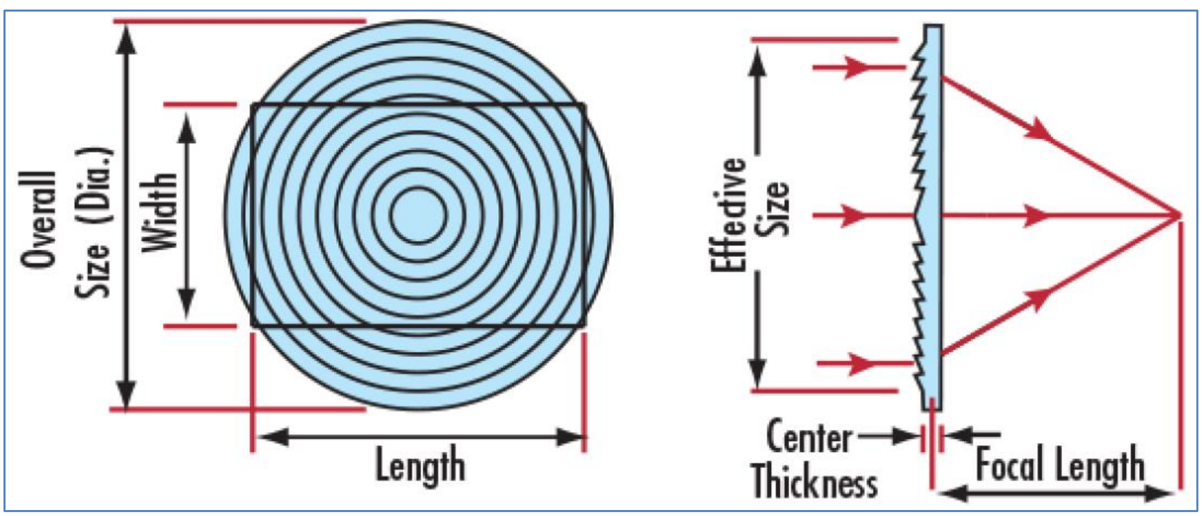

Figure 36 Schema representation of a Fresnel lens [91]

4.1 Fresnel lens specification

The selection of the Fresnel lens was based on the output temperature of the lens. For the research, in order to melt aluminium at 660°C, the lens should be able to generate temperatures in the region of 900°C. Also, it was important for the lens to be light-weight, have a small maximum power spot beam, be compact in size, have a shorter focal length, and have high-quality optics. For the project, two Fresnel lenses were utilized. The first lens (34 inches by 25 inches) was already available in the lab. However, the lens was in poor shape, with numerous scratches all over it. The lens was employed for the initial inspection, and it was discovered that the focal point of the lens was insufficiently powerful. The refractive index of lens #1 is 1.5 and it is made out of acrylic material. The following are the characteristics of the lens:

Size (in)	Beam	Beam size max power (in)	Focal length (in)	Weight (lb) without frame	Max temperature climb
34 x 25	Spot	0.3	27	2.86	1652°F

Table 4 34x25 Fresnel lens characteristics. Lens #1.

The lens was purchased from eBay in the year 2018 and was used in experiments to melt aluminum objects. For this lens, there was an existing frame in the lab with its respective stands. Modifications were made to the frame in order to accommodate the optical fiber cable.

The second Fresnel lens was purchased and imported from the green power science website hosted by Rojas Productions LLC from the USA. The lens was a 30" spot Fresnel lens in a white-water marine frame. The refractive index of lens #2 is also 1.5 and is made up of acrylic material too. The characteristics of the Fresnel lens listed by the manufacturer are as follows.

Figure 37 Old Fresnel lens with custom built frame

Size (in)	Beam	Beam size max power (in)	Focal length (in)	Weight (lb) with frame	Max temperature climb
21 x 21	Spot	0.4	25	5	1690°F

Table 5 21x21 Fresnel lens characteristics. Lens #2.

The Fresnel lens was assessed to boil 340 grams of water in approximately 102 seconds, flame wood in 0.1 seconds and melt zinc of 14 grams in 17 seconds just by holding it against the solar radiation [92]. The numerical aperture (NA) of the Fresnel lens can be calculated using the formula NA = $(n) * \sin\left(\frac{\theta}{2}\right)$, where (n) is the refractive index of the medium (air = 1) and θ is the aperture angle of the lens [93]. The aperture angle of a square Fresnel lens is given as $\theta = 2 * \ tan^{-1}\left(\frac{l}{2f}\right)$, where l is the length of one side of the lens and f is the focal length of the lens [94]. By solving the above two formulas, the Numerical Aperture for the #1 Fresnel lens is 0.62 and 0.38 for #2 Fresnel lens. It is necessary to understand that the NA of the lens should be small or equal to the NA of the optic fiber for efficient coupling of light into the fiber. If the NA of the lens is larger than the NA of the optic fiber, then not all of the light from the lens will be coupled into the fiber resulting in the losses [95].

Figure 38   New Fresnel lens with built frame

4.2 Lens frame design

The design specifications of the modified frame are displayed in Appendix C. A simple method was employed to hold the optical fiber at the focal length from the lens. Wood was used as it is easier to cut and drill holes compared to metal. Four arms in the 'L' shape were designed to hold the coupler in the center of the lens. The coupler was also

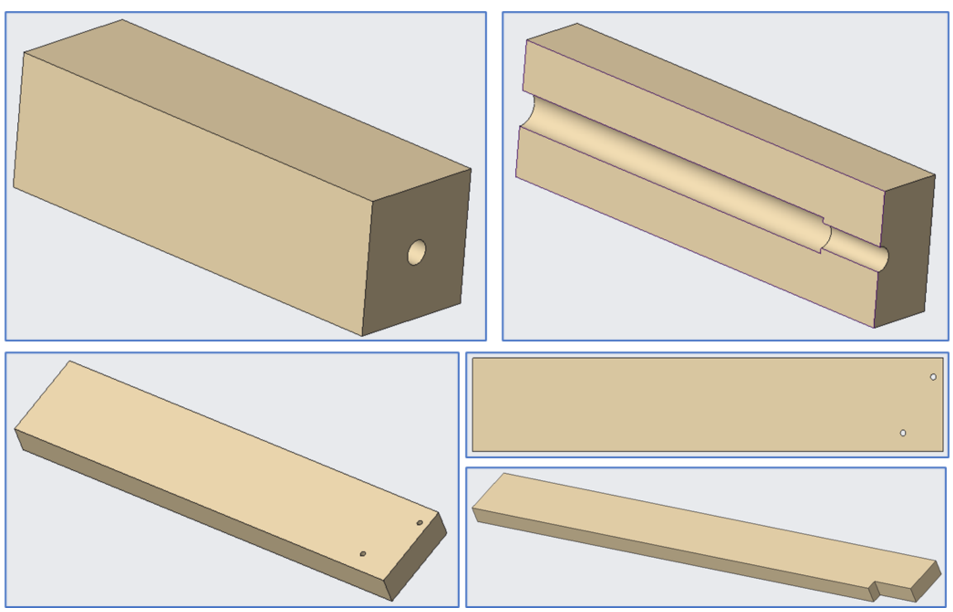

Figure 39   CAD model of lens frame

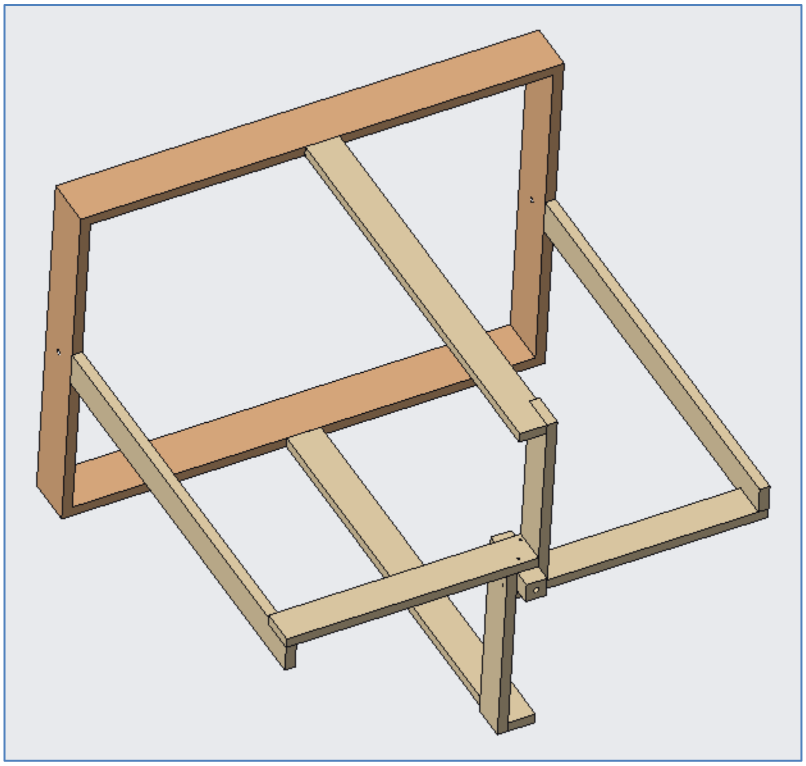

Figure 40 Manufactured lens frame components and assembled job.

manufactured out of wood and was used to hold the optical cable inside it. The design of the frame was completed using the CREO 7.0 design software, and the manufacturing was performed in the machine shop of the department. A total of nine wooden pieces were manufactured. Four support arms of a length of 30 inches, a width of 2.5 inches, and a thickness of 0.75 inches each were manufactured in the machine shop. Along with this, four cable supports, two of 18.43 inches length and two of 14 inches length, with the same width of 2.5 inches and thickness of 0.75 inches, were also cut out of wooden blocks. Finally, a square wooden block of 1.5 inches by 1.5 inches with a total length of 5 inches was cut to accommodate the optical fiber cable. Respective 0.39-inch (10mm) and 0.28-inch (7mm) holes were drilled to assemble the cable within the square wooden block. The frame was also designed in such a way that it will accommodate both lenses without any changes or alterations. The manufacturing drawings are presented in Appendix C. The frame was manually rotated in order to track the solar radiation and maintain maximum power output. An automated sun tracking system can be incorporated into future work. In order to utilize it, we need to first decide on the type of sun tracker: single axis (east to west) or dual axis (east to west and north to south). Then a suitable mechanical mechanism should be decided to control the position of the lens according to the sun, which can consist of motors, gears, belts, etc. The tracking mechanism will also require a microcontroller to program the tracking movement, like an Arduino or Raspberry Pi. Finally, the use of light sensors or GPS to detect the sun's position and feed the position information into the microcontroller.

4.3 Fiber optic cables

Fiber optic cables are an assembly similar to electrical cables but containing one or more optic fibers to carry or transfer light. The optical fiber cable uses the total internal reflection principle where the core is individually coated with plastic or metal layers and a protective cover over all the individual fibers. Due to the difference in refractive index between the two, optical fibers are made up of a core and a cladding layer that are chosen based on total internal reflection. Optic fibers are classified into two types: glass and plastic. They have significantly diverse properties and are used in vastly different applications. Plastic fibers are typically utilized in very short-range and consumer applications, whereas glass fibers are employed in medium (multi-mode) to long (single-mode) range telecommunications [96].

4.4 Optical cable specification

Since 1993, researchers have been working to develop solar thermal power systems for thermochemical material processing. The scope was to integrate a solar radiation

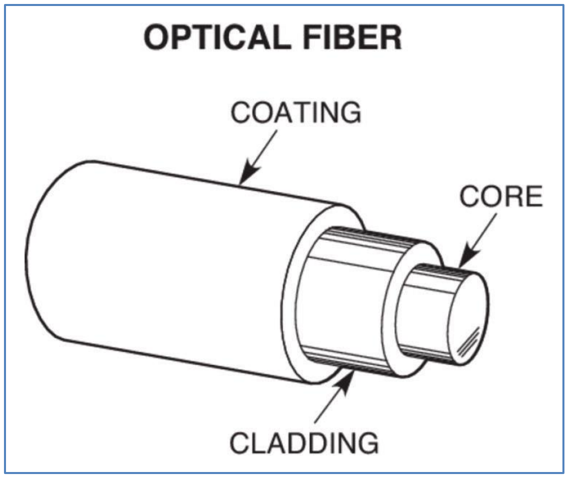

Figure 41   General optical fiber cable cross-sectional view [97]

concentrating array, which transfers the concentrated solar radiations to the optical waveguide transmission line. This transmission line would now have to supply carefully regulated solar radiation with minimal optical losses. From the research documents of Nakamura, Smith, and Benjamin [41], the optical fibers of interest to these applications are step-index and multimode fibers. The theory of optical fiber transmission is well developed and discussed by Snyder and Love [98]. The principle of total internal reflection (TIR) at the core-cladding boundary is utilized. The critical angle θ_c for TIR is characterized by the numerical aperture of the fiber:

$$\boxed{NA_f = n\, sin\theta_c = \sqrt{n_{co}^2 - n_{cl}^2}}$$

Where n_{co} and n_{cl} = refractive indices of the core and cladding; and n = refractive index of the medium in which the acceptance angle θ_c is measured. To achieve a large NA_f, n_{cl} must be significantly smaller than n_{co}. Commercially available cladding materials are fluorine doped fused silica (NA = 0.28), silicone (NA = 0.3-0.4) and hard polymer (NA = 0.37-0.48). To couple high concentration solar power into optical fiber thereby reducing the weight and cost of the solar power system, it is necessary to use optical fibers whose

NA is about 0.4 or higher [41]. Since the NA of the Fresnel lenses are 0.62 and 0.38, the selection of optical fibers with NA larger than that of the Fresnel lens is important to ensure maximum efficiency and minimum losses. Thus, we decided to go with hard polymer clad optical fiber.

The temperature measured out from the Fresnel lens focal spot is around 900°C, which indicated the operating temperatures of the optical fiber should also be high. The serviceable temperatures of the optical fibers are low approximately 350°C to 400°C and the buffer materials also fail to protect them from damage. Thus, the optical fibers should be very robust against chemical attacks and core to be fused with silica to sustain elevated temperature exposures. The serviceable temperature of the fibers gets limited due to the buffer materials where the polyimide's have melting temperatures of 385°C. If we remove the buffer, then the fiber can be used for hot temperature applications as fused silica has a high melting point (1600°C). The attenuation of optical fibers is routinely measured in dB/km and is defined as

$$\boxed{\alpha\left(\frac{dB}{km}\right) = \frac{10}{Lenght\ (in\ km)}\ log_{10}\left(\frac{Pin}{Pout}\right)}$$

The power of the light source is diminished during transmission through an optical fiber, which is known as attenuation. These include vibrational, electronic, and Rayleigh scattering absorptions. Given that they are material-dependent, these mechanisms are often referred to as intrinsic attenuations. These attenuations have a considerable impact on solar transmission, but they are frequently overridden by extrinsic attenuation. When water is added to the fiber core material during the fabrication process of synthetic fused silica, a significant amount of absorption loss occurs in the fiber. In the matrix, the water traces form -OH terminal groups. The -OH content of standard optical fibers is 1000ppm, which is considered exceedingly high for our application. As a result, where the grade has less than 5 ppm of -OH, a low -OH content optical fiber is preferred [41].

Figure 42 (L) Lumatec Optical fiber (R) Molex Polymicro Optical fiber

Manufacturer	**Lumatec**	Ceram Optec	**Molex**	Fiberguide industries
Product name	**Light guide series 380**	HWF 1000/1035 T	**Polymicro JTFLH1000**	Superguide SPCH1000
Core	**Quartz glass**	Pure silica	**Fused silica**	Fused silica
Cladding	**Aluminum sheet**	Hard polymer	**Hard polymer**	Hard polymer
Buffer	**Teflon**	Tefzel	**Tefzel**	Tefzel
Core diameter	**5mm**	1mm	**1mm**	1mm
NA	**0.59**	0.37	**0.37**	0.39
Operating temperature	**-5°C to +35°C**	-40°C to +150°C	**-65°C to +140°C**	-40°C to +200°C

Table 6 Comparison of optical fibers from various manufacturer

Table 6 exhibits the commercially available optical fibers investigated for the project. From the below selections, Lumatec Light guide series 380 and Molex Polymicro JTFLH1000 series were the optical fiber used for the project. Lumatec Light guide series

380 was sponsored by the Lumatec industries for the project. Whereas the Molex Polymicro JTFLH1000 optical fiber was purchased from a USA-based distributor for US$18.5/m. For project purposes, a total of 10m was ordered. The primary selection criteria of the optical fibers were core material, core diameter, numerical aperture, and operating temperature. The Light guide series from Lumatec was selected to be tested with the #1 Fresnel lens. Though the operating temperature of the fiber is only positive 35C, the bigger core diameter will help us to understand the function of light transfer and heat transfer. The operating spectrum wavelength ranged from ultraviolet to infrared spectrum. In order to transfer heat, the wavelength spectrum of infrared is important. As the wavelength increased from 700nm to 1000nm, the light transmission reduced from 75% to no light transmission. The Optic fiber from Molex -Polymicro was selected to perform the tests with the #2 Fresnel lens. The core of the fiber was fused silica with hard polymer cladding. The core diameter was 1mm with numerical aperture being 0.37±0.02. The operating wavelength spectrum of the optic fiber was stated from 450nm to 2100nm. Since the target is to operate the fiber optic in infrared wavelength spectrum i.e., 700nm to 1000nm. As per the manufacturers documents, the transmission of the Polymicro optic fiber increased from 90% at 700nm to 95% at 1000nm.

4.5 Test Sample Preparation

The optical fiber sample from Lumatec industries of Light guide series 380 was supplied in a ready-to-use state. Whereas the sample from Molex of Polymicro JTFLH1000 required preparation for tests. The fiber cable was 10m long. For the testing setup, the fiber was cut into 10 pieces of 0.5m each. Since the optical fibers were covered with the cladding and buffer, we needed to remove them in order for maximum operating temperature tolerance.

Figure 43 Test setup for Lumatec industries optic cable

This way, when all the 10 pieces of fibers are stacked together in a circular arrangement, the maximum diameter achieved is 3.95mm ≈ 4mm. The bundle of 10 optical fibers was secured together using heat-resistant tape.

Figure 43 shows how to set up Lumatec Industries' optic fiber with the Fresnel lens, whereas figure 46 shows how to set up Molex optic fiber with the Fresnel lens. The optic fibers were positioned in such a way that the incident beam will directly contact the fiber at the focus of the lens. Thus, the fiber tip was positioned 25 inches from the lens. The

Figure 44 Solar radiation focused on Lumatec industries optic cable.

frame was operated manually to align perpendicularly with the solar radiation. The complete setup was carried out in a private backyard with no participants present during the test procedure. Particular care was taken to make sure the lens was not left unattended at any time and always covered with a piece of cardboard when not in use.

Figure 45 Opposite end of Lumatec industries optic cable delivering light without heat

Figure 46 Test setup for Molex optic fiber

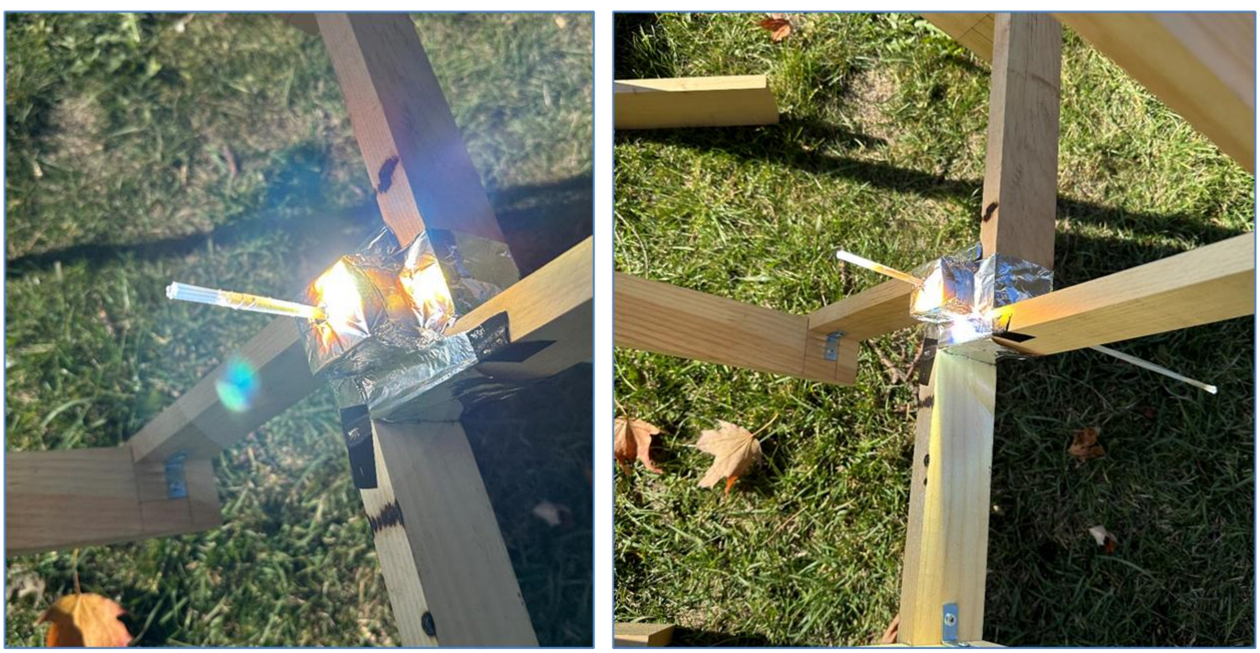

Figure 47 Solar radiation focused on Molex optic fiber

Figure 48 Opposite end of Molex Polymicro optic cable with max recorded temperature

The temperatures were measured using an infrared digital thermometer. The laser beam from the IR thermostat was utilized as a guiding point and was incident on the other end of the fiber's core area to record temperatures. The specification of the digital thermometer used is listed below:

Manufacturer	**Avantek dual laser infrared**
Model	TG-3Y
Temperature range	-50°C to +850°C
Temperature resolution	0.1°C
Emissivity	Adjustable from 0.10 to 1.00
Optimal resolution	D/S approx. 12:1

Since the distance to spot ratio of the thermometer is 12:1, in order to measure the temperature of a 5mm optic fiber bundle, the digital thermometer was held at an approx. distance of 60mm. The emissivity of the thermometer was set at 1.00 and a setting to hold the maximum recorded temperature for a period of 10 seconds was enabled. The emissivity of the optic fiber cable's core for Lumatec lightguide series is around 0.9 (typically for quartz glass), whereas the emissivity of the optic fiber's core for the Polymicro is around 0.9 to 0.95 (typically for fused silica). The surface of the fibers were cleaned with a soft cloth of debris and dust that could interfere with the readings. To ensure accuracy, multiple sets of readings were taken from different spots on the fiber end and the results were recorded. This will help account for any variations in temperature of the reflective surfaces.

Chapter 5: Results and Discussion

The tests were conducted during the summer season from June till October (Autumn). The average solar irradiance data for the respective months are given below in Table 7. The table is referenced from the Solar fundamentals of Solar energy course (MECH 5806-W). The solar irradiance values are in kW/m^2 around the world. It was evident from the previous records for Toronto that the months of June through August were

City	Jan	Feb	Mar	Apr	May	Jun	Jul	Aug	Sep	Oct	Nov	Dec
Birmingham, UK	0.65	1.18	2.00	3.47	4.35	4.53	4.42	3.87	2.67	1.48	0.83	0.45
Brisbane, AUS	6.35	5.71	4.81	3.70	2.90	2.43	2.90	3.61	4.93	5.45	6.33	6.32
Chicago, USA	1.84	2.64	3.52	4.57	5.71	6.33	6.13	5.42	4.23	3.03	1.83	1.45
Dublin, IRL	0.65	1.18	2.26	3.60	4.65	4.77	4.77	3.68	2.77	1.58	0.77	0.45
Glasgow, UK	0.45	1.04	1.94	3.40	4.48	4.70	4.35	3.48	2.33	1.26	0.60	0.32
Houston, USA	2.65	3.43	4.23	5.03	5.61	6.03	5.94	5.61	4.87	4.19	3.07	2.48
Johannesburg, SA	6.94	6.61	5.90	4.80	4.35	3.97	4.26	5.10	6.13	6.45	6.57	7.03
London, UK	0.65	1.21	2.26	3.43	4.45	4.87	4.58	4.00	2.93	1.68	0.87	0.48
Los Angeles, USA	2.84	3.64	4.77	6.07	6.45	6.67	7.29	6.71	5.37	4.16	3.13	2.61
Melbourne, AUS	7.13	6.54	4.94	3.20	2.13	1.93	2.00	2.71	3.87	5.26	6.10	6.68
New York, USA	1.87	2.71	3.74	4.73	5.68	6.00	5.84	5.39	4.33	3.19	1.87	1.48
Philadelphia, USA	1.94	2.75	3.81	4.80	5.55	6.10	5.94	5.42	4.37	3.23	2.13	1.68
Phoenix, USA	3.29	4.36	5.61	7.23	8.00	8.17	7.39	6.87	5.97	4.84	3.57	2.97
Sydney, AUS	6.03	5.54	4.23	3.07	2.61	2.33	2.55	3.55	4.63	5.87	6.50	6.13
Toronto, CAN	1.58	2.54	3.55	4.63	5.77	6.30	6.29	5.45	4.03	2.68	1.37	1.16
Vancouver, CAN	0.84	1.75	3.00	4.27	6.03	6.50	6.52	5.42	3.80	2.06	1.03	0.65

Table 7 Average monthly solar irradiance over the world (MECH 5806-W)

the peak summer months, followed by September and October. The incident solar irradiance onto the lens produced a high beam of light with a temperature in the region of 600°C. This was recorded by placing a sheet of aluminum in front of the lens at the focal length and measuring the temperature using the infrared laser digital thermometer. The input energy on the first Fresnel lens for the month of June can be calculated using the following when exposed for 15 minutes:

$\boxed{Input\ energy = Intensity\ x\ Area\ of\ lens\ x\ Time\ exposed}$, where intensity is the average solar irradiance per month in W/m^2 , area in m^2 and time in seconds. [99].

$$Input\ energy = 6.30x10^3 x\ (0.8636\ x\ 0.635)\ x\ 900$$

$$Input\ energy = 3109348.62\ Joule = 3.1\text{MJoule}$$

Similarly, the output energy can be calculated by considering the transmission efficiency of the fiber and the fiber end losses [95].

$$Output\ energy = \begin{pmatrix} input\ energy\ x\ transmission\ efficiency\ x\ fiber\ end\ losses \\ x\ total\ loss\ over\ length \end{pmatrix},$$

where transmission efficiencies are obtained from the manufacturers datasheet at 700nm wavelength. The attenuation coefficient of the Lumatec lightguide fiber optic is absent since the cable can only be manufactured up to 30m in lengths (consider 1). Whereas the coefficient of attenuation for the Molex Polymicro is 5dB/km as per the manufacturers datasheet. The total loss over length is given as attenuation coefficient times the length of fiber. As the length is 0.5m and attenuation coefficient is 5dB/km, the total loss over length is 0.0025dB. This when converted to ratio using total loss over length = 10^(-loss in dB/10) is 0.99996875. Fiber end reflection losses occur when light passes through the end of an optical fiber and is either reflected or absorbed resulting in a reduction in output power. The formula is:

$\boxed{Fiber\ end\ face\ losses = \left(\frac{n1 - n2}{n1 + n2}\right)^2}$, where n1 is the refractive index of core and n2 is the refractive index of the medium (air) [100]. The refractive index of core for Lumatec lightguide fiber optic is 1.54 and the refractive index of core for Polymicro cable is 1.55. Thus, the fiber end-face losses for Lumatec lightguide are 4.5% and similarly, fiber end-face losses for Polymicro cable are 4.65%. Thus, output energy for the month of June at 700nm wavelength is:

$$Output\ energy = 3109348.62\ x\ 0.7\ x\ 0.045 = 97944.48153 = 0.098\text{MJoule}$$

Similarly, for the following months the Input and output energy from the lens is as follows:

Input energy	Joules	MJ	Power (watt)
June	3109349	3.109	3454.83
July	3104413	3.104	3449.34
August	2689833	2.690	2988.70
September	1988996	1.989	2209.99
October	1322707	1.323	1469.67

Output energy	Joules	MJ	Power (watt)
June	97944.5	0.098	108.82
July	97789.0	0.098	108.65
August	84729.7	0.085	94.14
September	62653.4	0.063	69.61
October	41665.3	0.042	46.29

Table 8 34x25 inch #1 Fresnel lens input and output energy

Power is calculated simply by dividing the energy by time. The same approach is taken for the #2 Fresnel lens and the following table 9, depicts the input and output energies for the month of September and October.

$$\boxed{Input\ energy = Intensity\ x\ Area\ of\ lens\ x\ Time\ exposed}$$

$$Input\ energy = 4.03x10^3\ x\ (0.285)\ x\ 900$$

$$Input\ energy = 1031939.532\ Joule = 1.03\text{Mjoule}$$

Similarly, the output energy of the lens can be calculated using

$$\boxed{Output\ energy = Input\ energy\ x\ transmission\ efficiency\ x\ fiber\ end\ losses}$$

$$Output\ energy = 1031939.532\ x\ 0.95\ x\ 0.046$$

$$Output\ energy = 45585.93\ Joule = 0.0456\text{Mjoule}$$

Input energy	Joules	MJ	Power (watt)
September	1031939.5	1.032	1146.60
October	686252.59	0.686	762.50

Output energy	Joules	MJ	Power (watt)
September	45585.9	0.0456	50.65
October	30315.2	0.0303	33.68

Table 9 34x25 inch #1 Fresnel lens input and output energy

Table 10 indicates the Lumatec optic fiber is delivering very less heat/temperature at the output end compared to the incident heat/temperature. The fiber was able to transfer light from one end to the other but failed to carry the heat. The average temperature recorded is 18.8°C.

Table 11 indicates the Molex Polymicro optic fiber results. The fiber was received towards mid of September and thus the experiments are conducted for the last two months. The incident heat/temperature received at the other end of the fiber is significantly more than the Lumatec optic fiber. The temperature is still not enough to melt aluminum or silicone. The max temperature recorded on the infrared thermometer is 104.7°C, which is highlighted in Figure 48.

Month	Test iteration - 1	Test iteration - 2	Test iteration - 3
June	18.1	19.4	15.6
July	23.5	18.1	22.2
August	23.6	20.3	21.4
September	16.2	16.7	16.1
October	15.9	16.8	18.2

Table 10 Lumatec industries optic fiber temperature outputs

Month	Test iteration - 1	Test iteration - 2	Test iteration - 3	Test iteration - 4	Test iteration - 5
September	53.2	71.7	104.7	86.2	82.9
October	74.7	94.3	78.3	53.5	51.1

Table 11 Molex Polymicro optic fiber temperature outputs

It is observed that the temperatures are not constant, and a lot of fluctuations in temperature readings are experienced. Possible reasons can be the distance between the thermometer and the target is not constant. An IR (infrared) thermometer, also known as a non-contact thermometer, works by detecting the amount of thermal radiation emitted by an object. This radiation is in the form of infrared light and can be detected by the IR thermometer. The thermometer contains a lens that focuses the infrared radiation onto a detector, usually a pyroelectric sensor. The detector then converts the infrared radiation into an electrical signal, which is processed by the thermometer's electronics to calculate the temperature of the object. Additionally, the breeze or airflow can also affect the IR thermometer readings since the data was collected in an open environment. Finally, the thermometer may not be calibrated properly. When the temperature is measured at the opposite end of the optic fibers, it was expected to record a higher temperature in the region of 400°C to 500°C since the temperature of the heat energy concentrated from the Fresnel lens were recorded in the region of 600°C to 650°C but this was not the case. This can be due to the larger core diameter of the Lumatec optic fiber to transfer heat from one end to another. This allowed the heat to be dispersed or absorbed by the fiber. Another possible explanation is that the core diameter of the Molex Polymicro optic fiber was tiny and effective at carrying heat energy. Since the core was small, the heat-carrying capacity was reduced, but absorption was limited. By adding more fibers to the bundle, the heat carrying capacity can be improved. The initial approach involved using an IR thermometer to assess the temperature of the light emerging from the optic fiber. However, this method yielded somewhat imprecise results. To gain a more comprehensive understanding of the energy being emitted by the fiber, a direct measurement of the energy was deemed necessary. Thus, the incorporation of a silicon pyranometer is being proposed for future developments, as it would enable accurate quantification of the energy exiting the opposite end of the fiber optic. This adjustment would lead to more reliable and meaningful data for our research. Another improvement in recording the test results can be made by assembling the heat block at the end of the fiber cables and recording the rise in temperature of the heat block. Moreover, the number of lenses can also be increased to amplify more heat temperature. The heat energy obtained from one lens and one bundle can be coupled to a number of similar lenses and bundles to increase the heat energy output. The emissivity of the fiber optics were 0.9 (Lumatec lightguide) and 0.9-0.95 (Molex Polymicro) but the infrared laser digital thermometer's emissivity was set to 1.00. This should have been matched with the emissivity's of the optic fiber for more accurate temperature measurements. Additionally, the usage of more sensitive and accurate temperature measurement systems must be defined within the framework. To achieve maximum output, the solar radiation should be exactly perpendicular to the lens. The sun moves 15° every 1 hour. Thus, a sun tracker system incorporated in the design of the frame can accurately track the lens and sun relation for maximum output. The output can also be maximized by setting the experiment when the sky is clear and sunny causing longer and strong exposure to solar radiation. The presence of air as a medium may affect the heat transfer rate.

There were also a few differences from the experimental setup designed and utilized by Kato and Nakamura [41] for their tests. First, the use of 27 inches parabolic concentrating mirrors with a numerical aperture within that of optical fiber. The concentrator is made out of nickel substrate. Second, the optical fiber was 1.2mm in diameter with 10m in length. A total of 55 fibers were bundled to form 1 cable. As such, 7 cables were utilized in his arrangement. A total of 385 optic fibers were present when all of the fibers from all the cables were combined. For our setup, we utilized 1mm diameter optic fiber with a length of 0.5m. As such a bundle of 10 optic fibers was combined. Third, quartz glass concentrators were installed on the tip of the optic fibers. This acts as micro reflector cones to funnel the solar radiation into individual fibers. Quartz glass is utilized since it can transmit a wide range of wavelengths ranging from visible to near-infrared light. The reflectors can be shaped and positioned to optimize the amount of light captured and to direct the light onto the fiber at the correct angle for maximum efficiency. Four, solar tracking of sun sensors and two-axis trackers with an accuracy of 0.04° was utilized. Finally, a water-cooling system was incorporated to cool the temperatures of the optic fibers as the operating temperatures were only 120°C. The basic principle is to circulate cool water through a network of tubes or channels that are in contact with the fiber optic cables or devices, thereby dissipating the heat generated by the system. The process involves circulating water through a closed loop system that includes a pump, heat exchanger, and coolant reservoir. The water absorbs the heat generated by the fiber optic cables as it passes through the heat exchanger and is then cooled by the coolant reservoir before being recirculated through the system. According to my research and understanding, there is a potential presence of a heating source within the Kato and Nakamura setup, which was not explained by the authors in their reports.

The successful heat transfer from the optic fiber was not achieved, consequently hindering the ability to test the printer with printed parts. Based on the parameter set in Arduino firmware data, design features and electrical component parameters, the build volume was 100mm (X-axis) x 100mm (Y-axis) x 50mm (Z-axis). The micro-stepping for the Z-axis was set to move 0.1mm per step. This means that the printer can achieve a vertical resolution of 0.1mm, as it can move the build platform down by this distance in each step. This can be increased to 0.4mm for faster printing results but would decrease print accuracy and finish. The extruder nozzle size is 0.4mm. This also means that the printer can achieve a horizontal resolution of 0.4mm in both the X and Y directions, as it can lay down lines of material with this width. The print bed's temperature can be controlled to improve adhesion and prevent warping based on the raw material being used. It is controlled by a thermal diode capable of producing a maximum of 60°C.

Chapter 6: Conclusion and future work

Different approaches to the problem description of the project can be explored for future work. One possibility is eliminating the optic fiber as a conduit for transporting thermal energy and directly focusing sunlight from the Fresnel lens onto the 3D printing material. This concept was developed and presented by Markus Kayser in Moroccan deserts [59], where he successfully demonstrated solar sintering on Earth, creating rough but solid glass structures. Another possibility is replacing the optic fiber with heat-conducting materials, such as copper wire or high-temperature heat pipes, which can transfer heat energy from one end to another. Copper is a good conductor of heat, absorbs heat quickly, and maintains heat energy. This heat-carrying and holding capability can be utilized to increase the temperature within the heat block and eventually melt the 3D printing material. Similarly, heat-conductive high-temperature pipes can be employed as a substitute for optical fiber [104].

The contributions of this thesis are multi-fold. Firstly, it presents a novel approach to 3D printing on the lunar surface by utilizing solar radiation to melt and print materials, based on the hypothesis that a selective solar sinterer/melter for high-fidelity 3D printing of aluminum metal may be based on solar concentrator coupling to fiber-optic for heat transmission to any bounded location of a 2D plane. This research can potentially reduce dependency on traditional energy sources like electricity, which is required in most conventional 3D printing systems. The use of solar radiation can help to eliminate the need for electricity, making the system more sustainable and cost-effective in the long run. Secondly, the development of a 3D printing system that can operate on the lunar surface can have significant implications for in-situ resource utilization (ISRU) on the moon. The system can potentially enable the production of structures and equipment on-site, reducing the need for transportation of materials from Earth. Thirdly, the study of optical fibers' characteristics, including total internal reflection and core-cladding boundary, can contribute to the development of more efficient and effective 3D printing systems that utilize optical waveguide systems and their potential applications in future missions on the lunar surface. Based on the experimental data from the setup, it was observed that the solar radiation concentrated through a Fresnel lens generated temperatures in the range of 600°C to 650°C, depending on the size and shape of the lens. The optic fibers transfer infrared wavelengths or heat energy from one end to another when solar radiation is focused onto one face. The losses in the optic fibers could affect the total heat energy transferred at the other end. However, it was observed from the research that the solar radiation concentrated by the Fresnel lens was not able to transfer the radiation through the optic fiber from one end to another. The molten aluminum extrusion process is not feasible due to its high melting temperature and thermal conductivity. Therefore, other 3D printing technologies such as SLS or SLM would be better suited for aluminum extrusion as they use a powder bed fusion process that can melt metal powders and create parts.

In conclusion, the theory of 3D printing metals on the lunar surface with the help of solar energy is not feasible with the knowledge obtained through the research. The findings may be closer to the lunar environment, as it lacks atmospheric conditions, but results can always be recreated with minimal benchmarking settings. Varying seasons will also play a vital role in the successful completion of the project, as clear and strong solar irradiations are critical to any improvements and advancements in the project. Although the project could not achieve potential results, the idea of making this a reality is promising for future machines and advanced technology for space exploration. This will also certainly evolve the self-replicating machine technology, which is considered to be a valuable tool for space exploration.

Appendices

Appendix A : Literature review

A.1 Self-replicating machine:

A self-replicating machine is a type of autonomous robot that is capable of reproducing itself autonomously using raw materials found in the environment, thus exhibiting self-replication in a way analogous to that found in nature [101]. The concept of self-replicating machines has been advanced and examined by Homer Jacobson [102], John von Neumann [103], Konrad Zuse [104] and in more recent times by K. Eric Drexler in his book on nanotechnology, Engines of Creation [105] and by Robert Freitas and Ralph Merkle [106] in their review 'Kinematic Self-Replicating Machines', which provided the first comprehensive analysis of the entire replicator design space.

The future development of such technology is an integral part of several plans involving the mining of Moons and asteroid belts for ore and other materials, the creation of lunar factories, and even the construction of solar power satellites in space. The von Neumann probe is one theoretical example of such a machine. Von Neumann also worked on what he called the universal constructor [107], a self-replicating machine that would be able to evolve and which he formalized in a cellular automata environment. The primary limitation of the 3D printing technology resides in its serial in nature. This has prevented technology from evolving beyond functions. An important inspiration was the development of open source RepRap (replicating rapid prototypers) [48]. The RepRap is based on plastic FDM for complex construction geometries. Currently, RepRap can only replicate plastic parts, which comprises of simple structural design.

A.2 Aluminum reduction from regolith using the FFC process

Near closed loop lunar industrial ecology (emboldened materials are pure metal oxides for direct reduction using the FFC process.

Lunar Ilmenite

$Fe^0 + H_2O \rightarrow$ ferrofluidic sealing

$FeTiO_3 + H_2 \rightarrow \mathbf{TiO_2} + H_2O + Fe$

$2H_2O \rightarrow 2H_2 + O_2$

$2Fe + 1.5O_2 \rightarrow Fe_2O_3/Fe_2O_3.CoO$ - ferrite magnets

$3Fe_2O_3 + H_2 \leftrightarrow Fe_3O_4 + H_2O)$ – formation of magnetite at 350-750°C/1-2 kbar

$4Fe_2O_3 + Fe \leftrightarrow 3Fe_3O_4$)

Nickel-Iron Meteorites

W inclusions → Thermionic cathodic material

Mond process:

$W(CO)_6 \leftrightarrow 6CO + W$

$Fe(CO)_5 \leftrightarrow 5CO + Fe$ (175°C/100 bar) → Tool steel

$Ni(CO)_4 \leftrightarrow 4CO + Ni$ (55°C/1 bar) → Electrical steel

$Co_2(CO)_8 \leftrightarrow 8CO + 2Co$ (150°C/35 bar) → Permalloy

Alloy	Ni	Co	Si	C	W
Tool steel				2%	9-18%
Electrical steel			3%		
Permalloy	80%				
Kovar	29%	17%	0.2%	0.01%	

S catalyst

$4FeS + 7O_2 \rightarrow \mathbf{2Fe_2O_3} + 4SO_2$

(Troilite) $SO_2 + H_2S \rightarrow 3S + H_2O$

$FeSe + Na_2CO_3 + 1.5O_2 \rightarrow \mathbf{FeO} + Na_2SeO_3 + CO_2$ at 650°C

KNO_3 catalyst $Na_2SeO_3 + H_2SO_4 \rightarrow Na_2O + H_2SO_4 + Se \rightarrow$ photosensitive Se

$Na_2O + H_2O \rightarrow 2NaOH$

$NaOH + HCl \rightarrow NaCl + H_2O$

Lunar Orthoclase

$3KAlSi_3O_8 + 2HCl + 12H_2O \rightarrow KAl_3Si_3O_{10}(OH)_2 + 6H_4SiO_4 + 2KCl$

orthoclase illite silicic acid (soluble silica)

$2KAl_3Si_3O_{10}(OH)_2 + 2HCl + 3H_2O \rightarrow 3Al_2Si_2O_5(OH)_4 + 2KCl$

kaolinite

$[2KAlSi_3O_8 + 2HCl + 2H_2O \rightarrow Al_2Si_2O_5(OH)_4 + 2KCl + \mathbf{SiO_2} + H_2O]$

$KCl + NaNO_3 \rightarrow NaCl + KNO_3$

$2KCl + Na_2SO_4 \rightarrow 2NaCl + K_2SO_4$

Lunar Olivine

$3Fe_2SiO_4 + 2H_2O \rightarrow 2Fe_3O_4 + 3\mathbf{SiO_2} + 2H_2O$ → magnetite for hard magnets

fayalite magnetite

$Mg_2SiO_4 + 4H_2O \rightarrow \mathbf{2MgO} + \mathbf{SiO_2} + 4H_2O$ → 3D Shaping binder

forsterite $MgO + HCl \rightarrow MgCl_2 + H_2O$ → 3D Shaping binder

Lunar Anorthite

$CaAl_2Si_2O_8 + 4C \rightarrow CO + \mathbf{CaO} + \mathbf{Al_2O_3} + 2Si$ at 1650°C → CaO cathode coatings

$CaO + H_2O \rightarrow Ca(OH)_2$

$Ca(OH)_2 + CO_2 \rightarrow CaCO_3 + H_2O$

$CaAl_2SiO_8 + 8HCl + 2H_2O \rightarrow CaCl_2 + 2AlCl_3.6H_2O + \mathbf{SiO_2}$ → fused silica glass + FFC electrolyte

$AlCl_3.6H_2O \rightarrow Al(OH)_3 + 3HCl + H_2O$ at 100°C

$2Al(OH)_3 \rightarrow \mathbf{Al_2O_3} + 3H_2O$ at 400°C $\rightarrow 2Al + Fe_2O_3 \rightarrow 2Fe + Al_2O_3$ (thermite)

AlNiCo hard magnets

<u>Lunar Pyroxene</u> Al solar sail

$Ca(Fe,Al)Si_2O_6 + HCl + H_2O \rightarrow Ca_{0.33}(Al)_2(Si_4O_{10})(OH)_2.nH_2O + H_4SiO_4 + CaCl_2 + Fe(OH)_3$

Augite montmorillonite silicic acid iron hydroxide

<u>Lunar Volatiles</u>

$CO + 0.5\ O_2 \rightarrow CO_2$

$CO_2 + 4H_2 \xrightarrow{\text{Ni catalyst}} CH_4 + 2H_2O$ at 300°C (Sabatier reaction)

$CH_4 + H_2O \xrightarrow[\text{Ni catalyst}]{850^\circ C} CO + 3H_2 \xrightarrow[Al_2O_3]{250^\circ C} CH_3OH$

$CH_3OH + HCl \xrightarrow[Al_2O_3]{350^\circ C} CH_3Cl + H_2O$

$CH_3Cl + Si \xrightarrow{370^\circ C} (CH_3)_2SiCl_2 \xrightarrow{+nH_2O} ((CH_3)_2SiO)_n + 2nHCl \rightarrow$ silicone plastics/oils

$N_2 + 3H_2 \xrightarrow{\text{Fe on } CaO+SiO_2+Al_2O_3} 2NH_3$ (Haber-Bosch process)

$4NH_3 + 5O_2 \xrightarrow{\text{WC on Ni}} 4NO + 6H_2O$

$3NO + H_2O \rightarrow 2HNO_3 + NO$ (Ostwald process)

$2SO_2 + O_2 \leftrightarrow 2SO_3$ (low temp)

$SO_3 + H_2O \rightarrow H_2SO_4$

<u>Salt of the Earth</u>

$2NaCl + CaCO_3 \leftrightarrow Na_2CO_3 + CaCl_2$ (Solvay process) → FFC electrolyte

$Na_2CO_3 + SiO_2(i) \xrightarrow{350^\circ C/150\ MPa} Na_2SiO_3 + CO_2$ → piezoelectric quartz crystal growth (40-80 days)

$CaCO_3 \xrightarrow{1000\text{-}1100^\circ C} \mathbf{CaO} + CO_2$ (calcination)

$NaCl(s) + HNO_3(g) \rightarrow HCl(g) + NaNO_3(s)$ → recycling reagents

$2NaCl(s) + H_2SO_4(g) \rightarrow 2HCl(g) + Na_2SO_4(s)$

<u>Metalysis FFC Process ($CaCl_2$ electrolyte)</u>

$MO_x + xCa \rightarrow M + xCaO \rightarrow M + xCa + \frac{1}{2}xO_2$ where M=Fe, Ti, Al, Mg, Si, etc

$CO + 0.5\ O_2 \rightarrow CO_2$

$CO_2 + 4H_2 \xrightarrow{\text{Ni catalyst}} CH_4 + 2H_2O$ at 300°C (Sabatier reaction) $\rightarrow CH_4 \rightarrow C + 2H_2$ at 1400°C → FFC anode regeneration

Appendix B : 3D printer assembly parts and electronic components

B.1 Print head design considerations:

The print head nozzle of the printing machine is used to eject aluminum through. The extruding tip of the nozzle used is a standard 0.6mm available in the market and is made out of hardened-steel. For this project, there are two different print head nozzle assemblies used. One is for extruding aluminum infused polymer if the raw material are pellets and the second is designed if the raw material is filament (1.75mm diameter). The aluminum pellets from the Virtual Foundry melts above 205°C temperature. Figures 49 and 50 illustrates the two print head nozzle designs. Both are custom designed to accommodate the necessary aspects of the optical fiber cable. Figure 49 shows the print head design for aluminum infused polymer pellets. The design involves a plunger and outer shell made out of SS303 respectively. The process is similar to plastic injection molding where the pellets are heated, melted, and pushed down the shell tube. The hopper is located above the heat block where the entry for optic cable is positioned. The pellets are fed into the hopper, which then melts and gets pushed towards the heat block by screw mechanism created by a rotating stepper motor. The manufacturer recommended temperatures in the range of 200°C-230°C for the pellets to melt. An external source of electrical power is supplied to raise the temperature of the hopper using a solar panel of 1m^2 area which will generate a power of 273.2 watts. This is calculated considering the average solar radiation on moon is about 1366W/m^2 per hour with an efficiency of 20% of solar panel [108].

$$Power{=}solar\ panel\ area\ x\ sunlight\ intensity\ x\ efficiency$$

$$power = 1m^2\ x\ 1366\frac{w}{m^2}\ x\ 20\% \quad = 273.2\text{ W}$$

A Nichrome wire is wound around the hopper shell in two areas. These two areas represent the two zones on the hopper shell, top barrel, and bottom barrel. A 24V solar panel will generate a current of 11.25A since the power is 273.2W. The heat energy generated by nichrome wire at 5A current for 15min at 0.1Ω is 2750 joules ($Q = I^2Rt$, where Q = heat energy, I = current, R = resistance and t = time in seconds). This heat energy will generate a temperature of 250°C for the top barrel (Q = mass x specific heat capacity x temperature diff.). Similarly, by reducing the current to 4.3A, temperature of 150°C is achieved for the bottom barrel. The top barrel is exposed to ambient air temperature and thus the temperature required is high. The temperature decreases at the bottom barrel to maintain a consistent temperature for the molten material so that it flows properly and produces high quality parts. Solar panels are a good source of energy on the moon. However, the efficiency of solar panels are about 15-20%. They degrade over time. The effective reduce with accumulation of dust on surface panels and they need energy storage equipment. Finally, another source is required to convert power into heat energy. Whereas in Fresnel lens the energy conversion to heat is direct.

To calculate the pressure required to move molten aluminum through a tube, we can use the Darcy-Weisbach equation [109]:

$$\boxed{\Delta P = f * (L/D) * (\rho * V^\wedge 2 / 2)}$$

where ΔP = pressure drop, f = Darcy friction factor (which depends on Reynolds number and the roughness of the pipe), L = length of the pipe, D = diameter of the pipe, ρ = density of molten aluminum, V = velocity of molten aluminum, We can estimate the density of molten aluminum at 660°C using the following equation: $\rho = \rho 0 / (1 - \beta * \Delta T)$.

where ρ0 = density at 20°C (which is 2.70 g/cm^3 for aluminum), β = thermal expansion coefficient of aluminum (which is 0.0000235 per °C), ΔT = temperature difference (in °C), from 20°C to the desired temperature, ρ = 2.70 / (1 - 0.0000235 * (660 - 20)) = 2.10 g/cm^3.

a) Converting g/cm^3 to lb/in^3: ρ = 2.10 g/cm^3 * 0.0361273 lb/in^3/g/cm^3 = 0.07595 lb/in^3

b) Converting 60 mm/s to in/s, V = 60 mm/s / 25.4 mm/in = 2.36in/s

Now we can calculate the Reynolds number: $Re = (\rho * V * D) / \mu$, where μ is the dynamic viscosity of molten aluminum at 660°C. According to literature [110], μ is around 0.08 lb-s/in^2.

Re = (0.07595 lb/in^3 * 0.394 in/s * 1 in) / 0.08 lb-s/in^2 = 2.23

Assuming the pipe is smooth, we can estimate the Darcy friction factor using the following equation: f = 64 / Re

f = 64 / 0.373 = 28.7

Now we can calculate the pressure drop:

$\Delta P = f * (L/D) * (\rho * V^2 / 2)$

$\Delta P = 28.7 * (4\ in / 1\ in) * (0.07595\ lb/in^3 * (2.36\ in/s)^2 / 2) = 3.98\ lb/in^2$

Therefore, the pressure required to move molten aluminum through the shell with a flow rate of 60 mm/s is approximately 3.98 lb/in^2 (PSI). The recommended flow rate is suggested in the manufacturer's datasheet (Appendix B.7). The datasheet also mentions the sintering temperature to be around 550°C for a 90% metal part.

The pressure created by the linear screw motion due to the rotational motion by stepper motor is given by [111]:

$$\boxed{Pressure = \frac{(Torque\ x\ Efficiency)}{(Screw\ pitch\ x\ Screw\ diameter)}}$$

Where efficiency of the NEMA 23 motor is considered to be 90% and the stated torque of the motor is 963 oz-in (6.8 N-m). The screw pitch of the plunger is 0.35 inch (0.00889 m) and diameter of the plunger is 1 inch (0.0254 m).

$$Pressure = (6.8\ x\ 0.9)/\ (0.00889\ x\ 0.0254)$$

$$Pressure = 27{,}580\ N/m^2 =\ 4\ \mathrm{lb/in^2}\ \text{(PSI)}$$

Thus, the pressure exerted by the rotational motion of motor is more than the required pressure for the molten aluminum to flow. There are a few advantages of pellets over filament: Cost effectiveness-pellets are typically less expensive on a per pound basis. Customizable-pellets can be mixed and matched to create custom colors or materials allowing more versatility in 3D printing. Less waste-pellets generate less waste than filaments since they are not pre-spooled. Higher print quality- Pellets can produce higher quality prints with better layer adhesion and smoother finishes due to the ability to control the temperature and viscosity of the melted plastic more precisely.

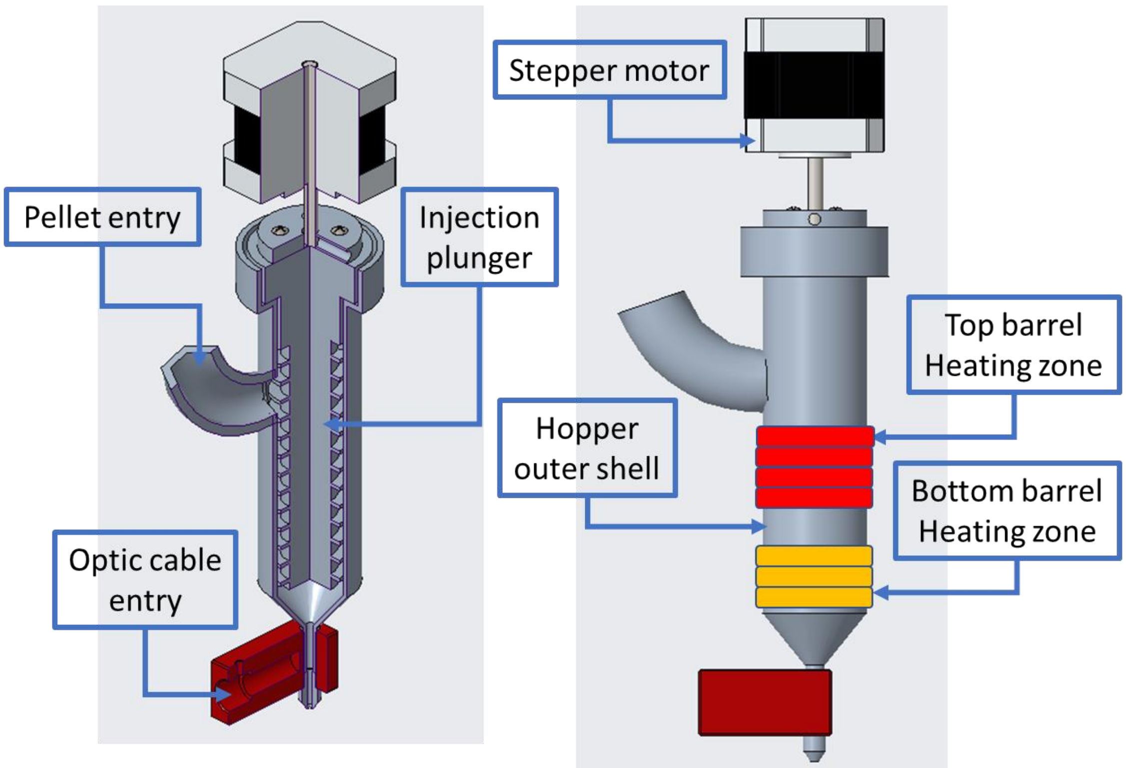

Figure 49 Print head nozzle design for pallets

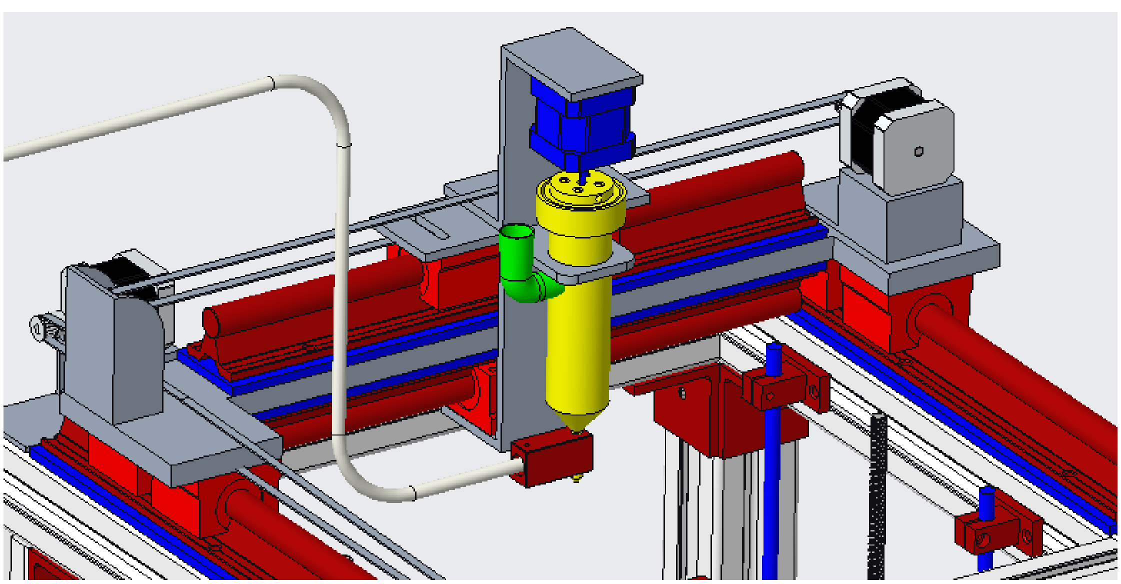

Figure 50 Print head nozzle design for pallets

Figure 50 depicts the print head design for the aluminum infused polymer filament. The design of this module is simple and remarkably similar to print heads available in the market called Bowden extruders. A motor and gear drives the filament through a Bowden tube and fed into the heat block. The heat block is manufactured out of silver (melting point of 961.8°C). This design allows for greater precision in filament feeding and can reduce the weight of the print head. Bowden extruders are considered with a view to reduce the contact between the hot end and the extrusion gear mechanism. With Bowden extruder, the

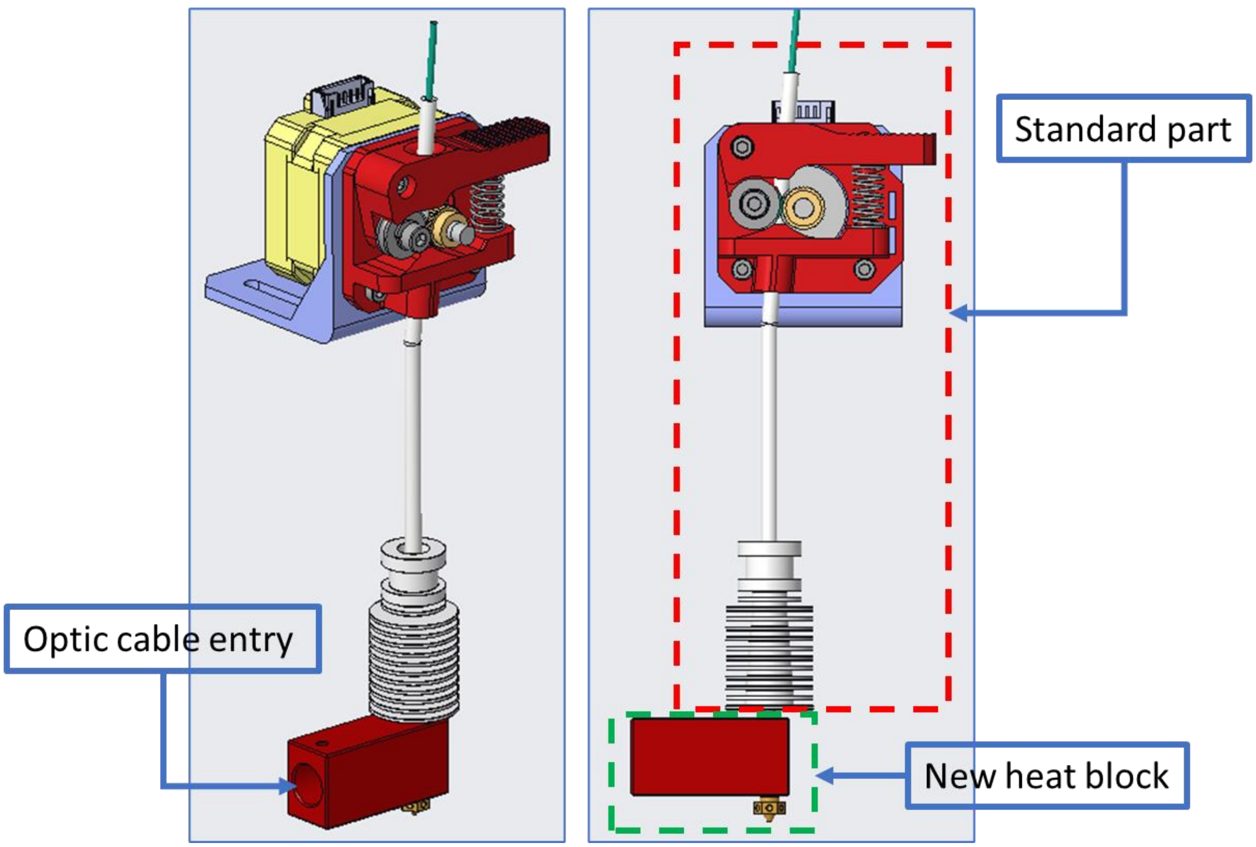

Figure 51 Print head nozzle design for filament

placement of the gear drives controlling the extrusion becomes less of a concern. The extruding gears can be placed anywhere on the frame and the nozzle is connected with the Bowden tube which carries the filament. Bowden extruders require more retraction distance than direct drive extruders because the distance between the extruders and hot end is greater and this causes more compression and decompression of the filament inside the filament [112]. This design is not suitable for flexible materials due to the increased amount of compression inside the Bowden tube. Bowden extruders provide high precision and speed but requires careful calibration. Since the design of the hot end block may vary depending upon the optic waveguide, it was decided to consider the Bowden extruder setup for more flexibility in future upgrades. As seen in figure 50, the top half of the assembly is standard (within red dotted lines) and will feed the filament into the heat block. The new heat block will accommodate the optical fiber cable which will melt the filament for extrusion.

Silver tends to have relatively high thermal conductivity which means it can absorb and transfer heat relatively well. However, It also has low emissivity of 0.02 to 0.05 which means that it tends to reflect more heat than it absorbs. This can be controlled by altering the surface finish. A rough and matte surface tends to absorb more heat and has a higher absorptivity and can increase up to 0.5 emissivity. At higher temperatures, the emissivity can also increase due to increased surface oxidation or roughening.

B.2 Stepper motor bracket for X, Y axis - drawing

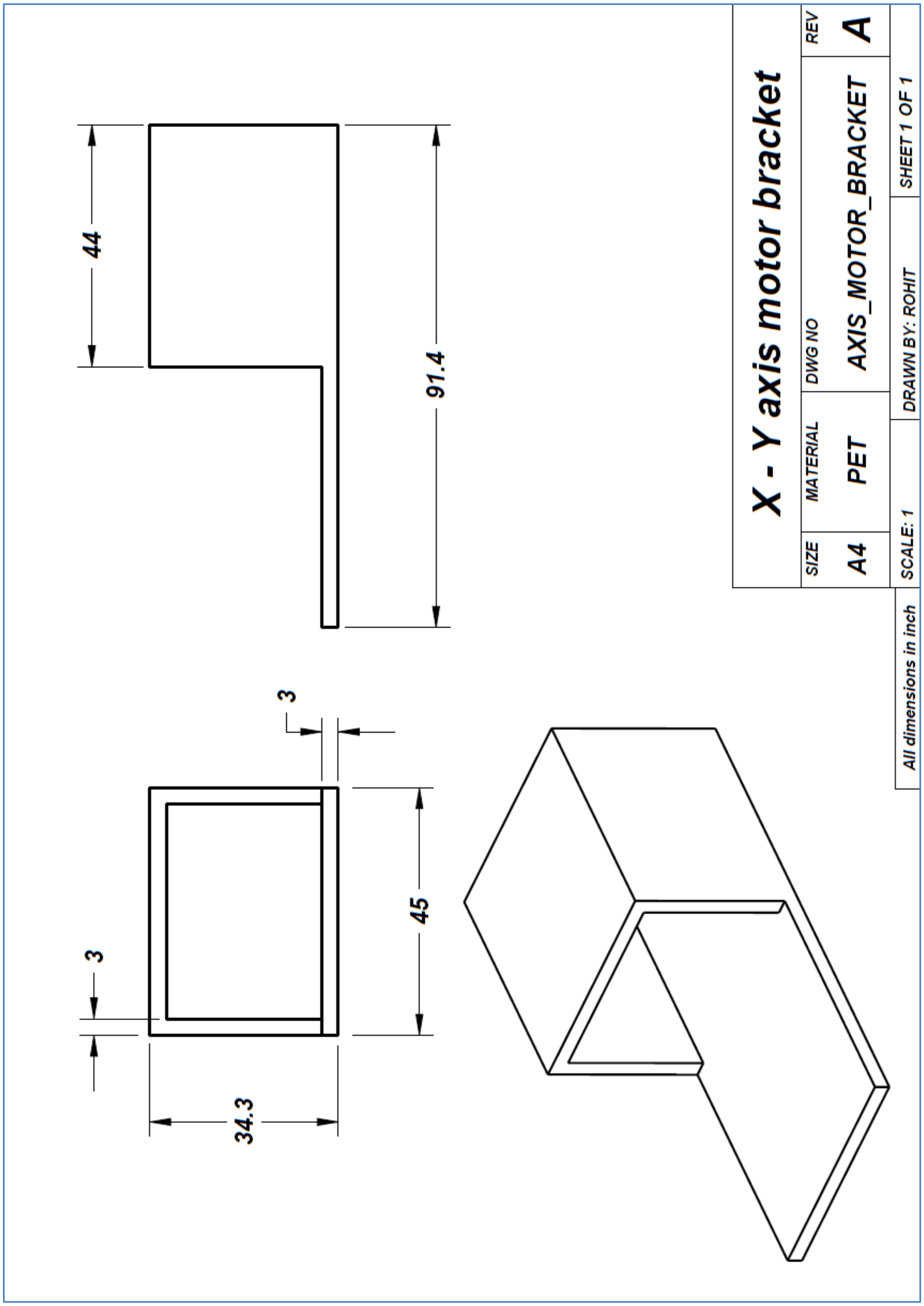

B.3 Printbed support - drawing

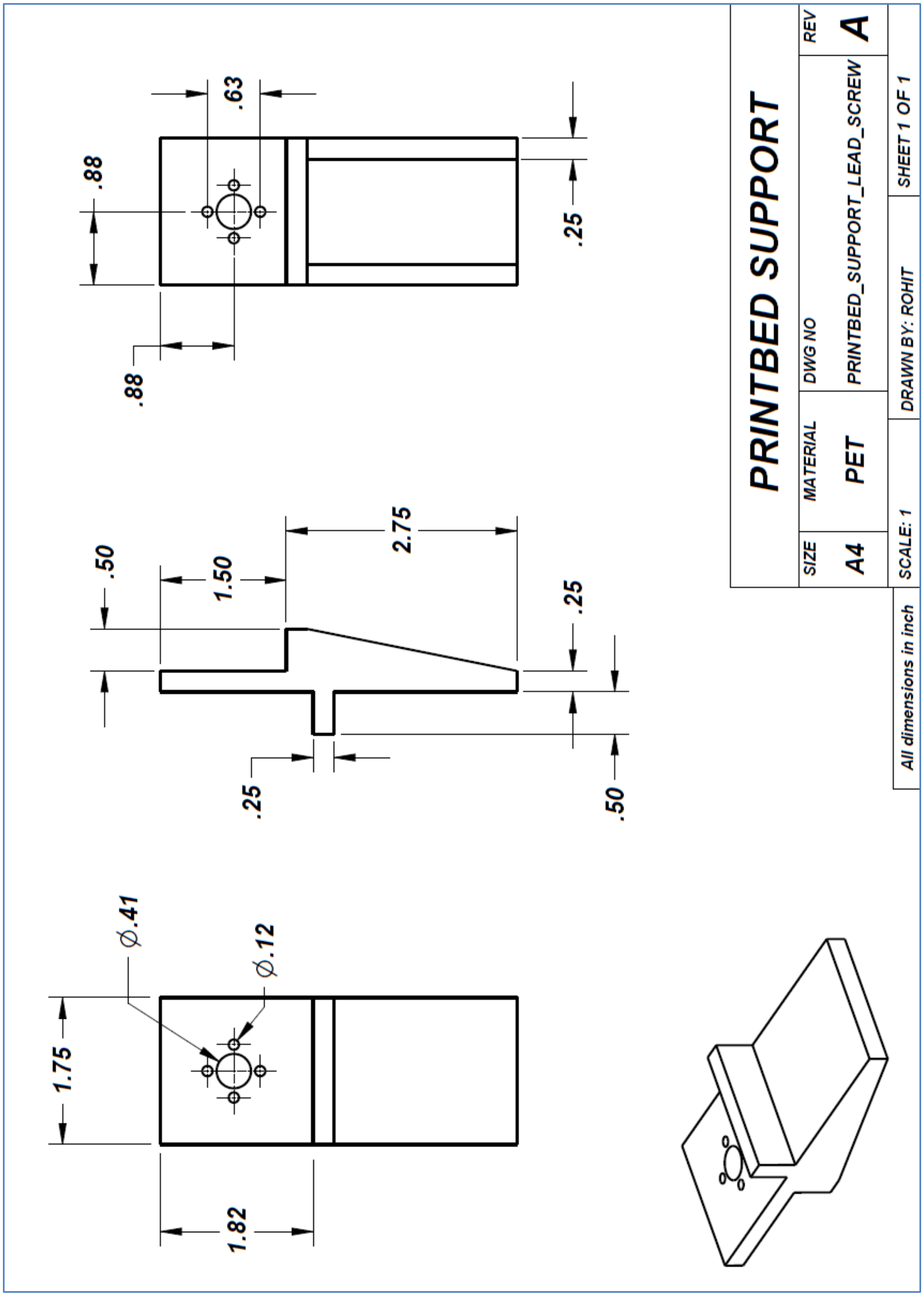

B.4 Extruder nozzle support bracket - drawing

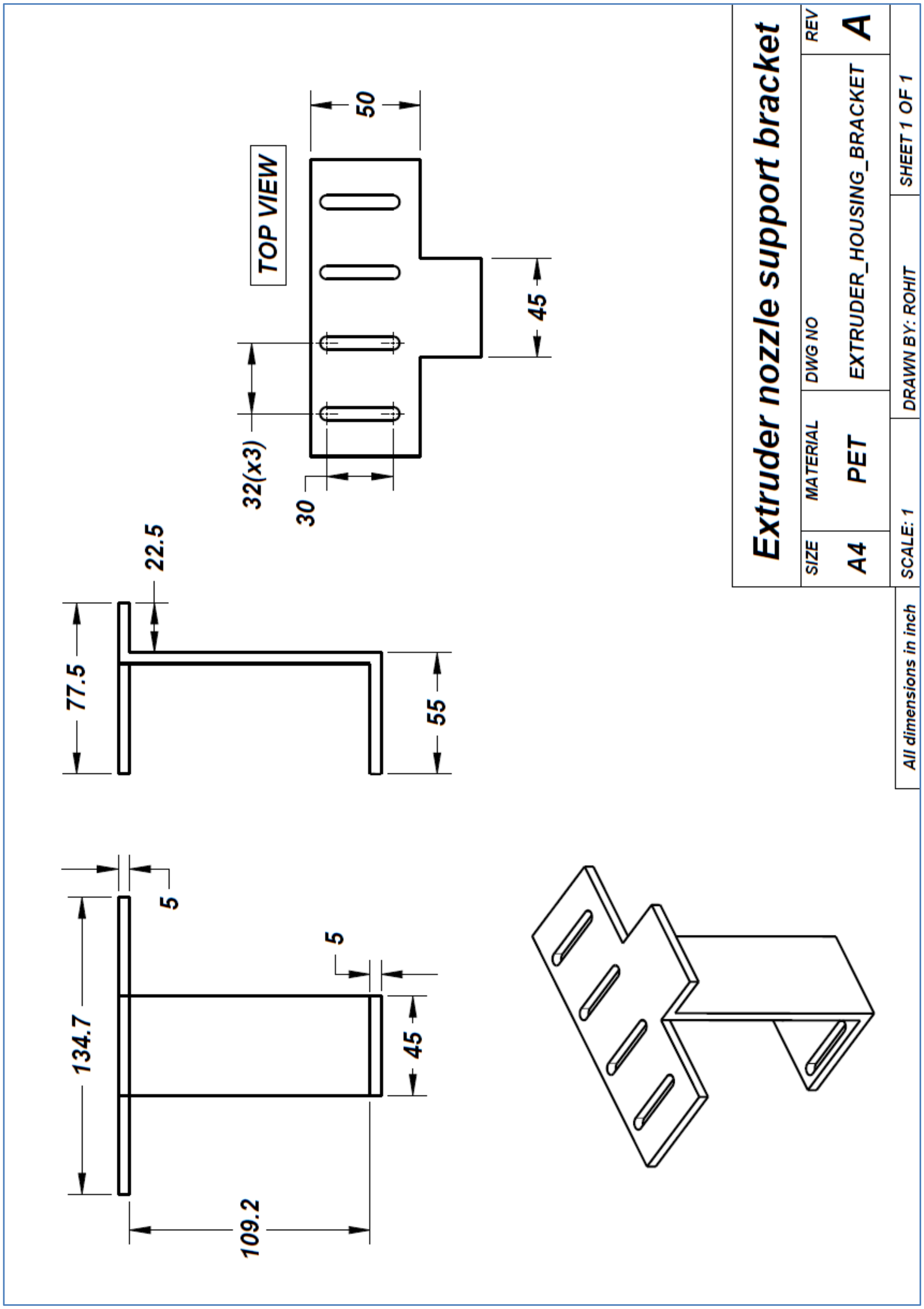

B.5 Print head nozzle for pellet-based input - drawing

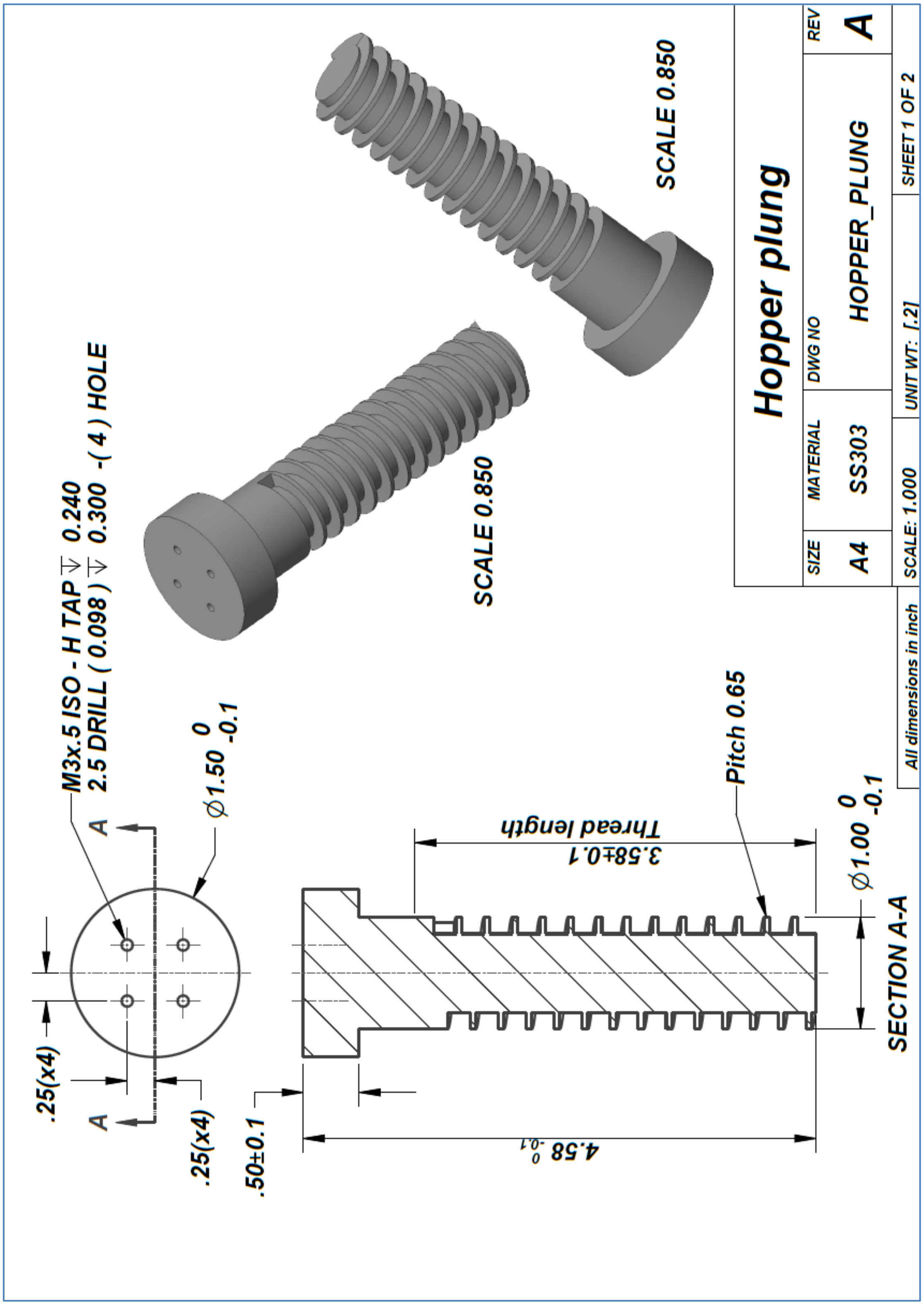

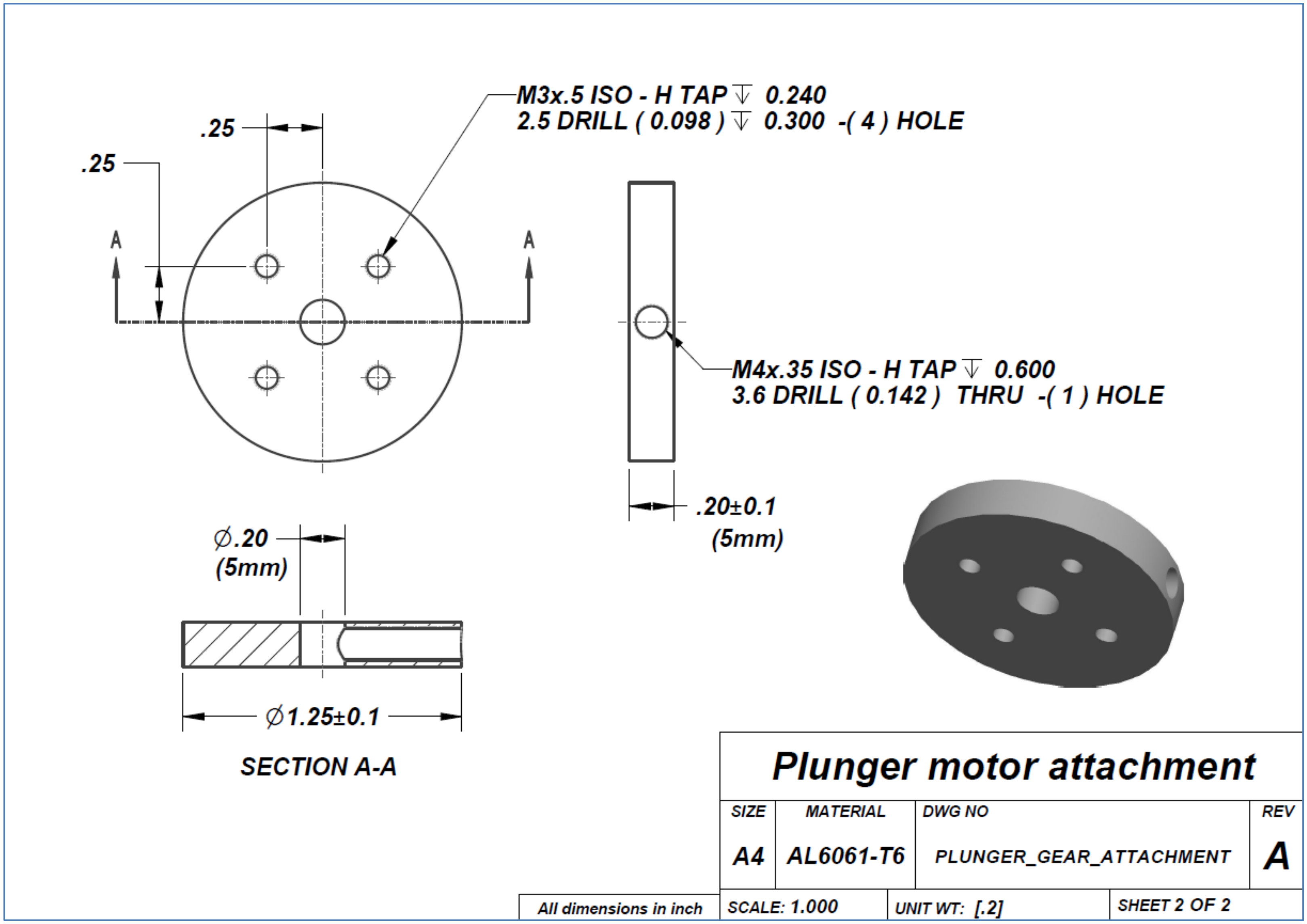
M3x.5 ISO - H TAP ↧ 0.240
2.5 DRILL (0.098) ↧ 0.300 -(4) HOLE
.25
.25
A
A
M4x.35 ISO - H TAP ↧ 0.600
3.6 DRILL (0.142) THRU -(1) HOLE
.20±0.1
(5mm)
∅.20
(5mm)
∅1.25±0.1
SECTION A-A
Plunger motor attachment
SIZE
A4
MATERIAL
AL6061-T6
DWG NO
PLUNGER_GEAR_ATTACHMENT
REV
A
All dimensions in inch
SCALE: 1.000
UNIT WT: [.2]
SHEET 2 OF 2

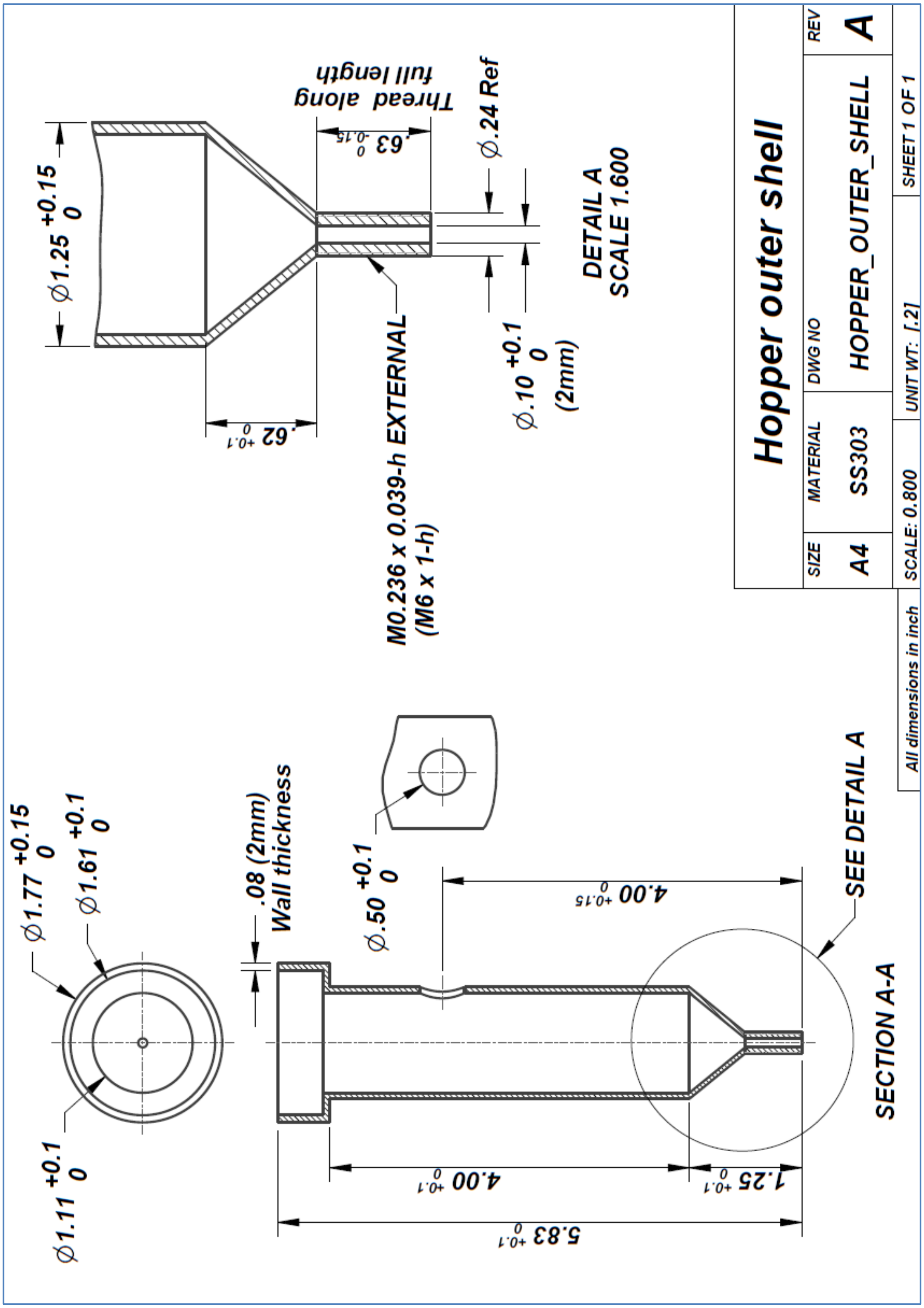

Ø1.77 +0.15 0
Ø1.61 +0.1 0
Ø1.11 +0.1 0
.08 (2mm)
Wall thickness
Ø.50 +0.1 0
4.00 +0.15 0
4.00 +0.1 0
1.25 +0.1 0
5.83 +0.1 0
SEE DETAIL A
SECTION A-A
Ø1.25 +0.15 0
.63 0 -0.15
Thread along
full length
Ø.24 Ref
.62 +0.1 0
M0.236 x 0.039-h EXTERNAL
(M6 x 1-h)
Ø.10 +0.1 0
(2mm)
DETAIL A
SCALE 1.600
Hopper outer shell
SIZE
A4
MATERIAL
SS303
DWG NO
HOPPER_OUTER_SHELL
REV
A
SCALE: 0.800
UNIT WT: [2]
SHEET 1 OF 1
All dimensions in inch

B.6 Print head nozzle for filament-based input - drawing

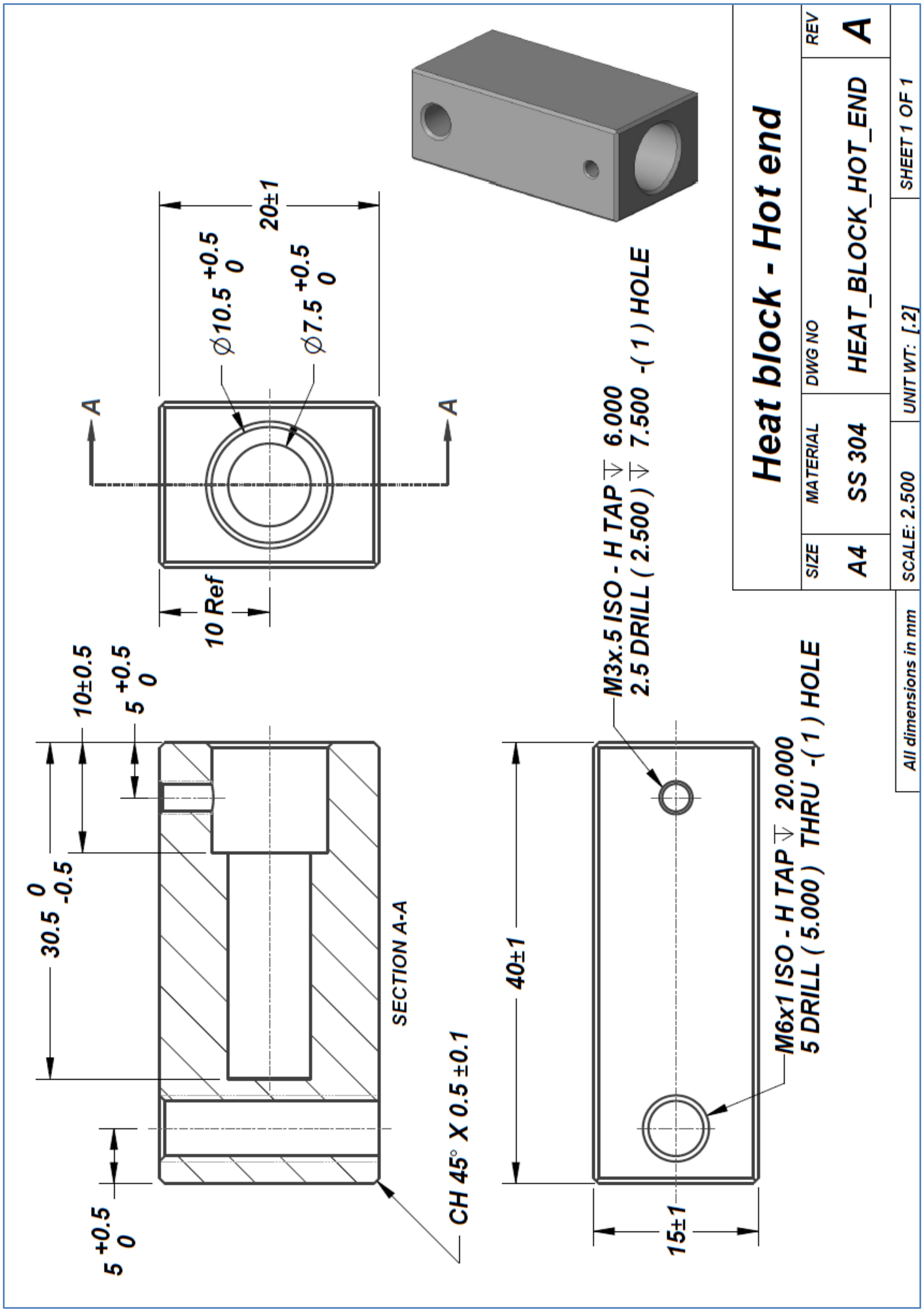

B.7 Technical data sheet for Al6061 filament

The Virtual Foundry

TECHNICAL DATA SHEET
Aluminum 6061 Filamet™

Page 1 of 1

SECTION 1 - TYPICAL MATERIAL PROPERTIES

Physical Properties	Unit	Value
Density	g/cc	1.50 - 1.54
Humidity Absorption	%	No information available
Tensile Strength	MPa	No information available
Tensile Elongation	%	No information available
Flexural Strength	MPa	No information available
Flexural Modulus	GPa	No information available
Izod Impact Strength	kJ/m^2	No information available

SECTION 2 - FILAMENT SPECIFICATION

Nominal Diameter	Diameter Tolerance	Ovality
1.75mm	± 0.05	≥ 95%
2.85mm	± 0.05	≥ 95%

Net Filament Weight	Metal Content
1000 / 500 / 250 grams	60% - 65%

SECTION 3 - GUIDELINE FOR PRINT SETTINGS

Advised Printing Temperature	205 - 235°C
Advised Build Plate Temperature	40 - 50°C
Build Plate Surface Type	Glass / PEI / G10 / Powder Coated Spring Steel
Build Plate Preparation	Glue Stick (on glass) Blue Painter's Tape (on PEI/G10) - Nothing needed for Powder Coated Spring Steel
Print Cooling	None Required
Advised Printing Speed	60mm/sec (3600mm/min)
Nooze Size/Type	0.6mm / Hardened Steel

SECTION 4 - ADDITIONAL INFORMATION

Sintering Temperature: 555°C (1031°F)

This filament is abrasive and will wear standard brass nozzles fast. The Virtual Foundry, Inc recommends a hardened steel nozzle. A Filawarmer is not required for this filament.

DISCLAIMER: The product and technical information provided in this datasheet is correct to the best of The Virtual Foundry, Inc's knowledge. The information given is provided as a guidance for good use, handling and processing and is not to be considered as a quality specification. The information only relates to the specific product and the material properties.

B.8 NEMA 17 stepper motor datasheet

Quick Reference

NEMA size 17 1.8° 2-phase stepper motor

Schneider Electric

Notes and Warnings

Installation, configuration and maintenance must be carried out by qualified technicians only. You must have detailed information to be able to carry out this work.

- Unexpected dangers may be encountered when working with this product!
- Incorrect use may destroy this product and connected components!

For more information, go to www.imshome.com

Specifications

1.5 Amp motors		Single length	Double length	Triple length
Part number		M-1713-1.5 • *(1)*	M-1715-1.5• *(1)*	M-1719-1.5• *(1)*
Holding torque	oz-in	32	60	75
	N-cm	23	42	53
Detent torque	oz-in	1.7	2.1	3.5
	N-cm	1.2	1.5	2.5
Rotor inertia	oz-in-sec²	0.000538	0.0008037	0.0011562
	kg-cm²	0.038	0.057	0.082
Weight	oz	7.4	8.1	12.7
	grams	210	230	360
Phase current	amps	1.5	1.5	1.5
Phase resistance	ohms	1.3	2.1	2.0
Phase inductance	mH	2.1	5.0	3.85

(1) Indicate S for single-shaft or D for double-shaft. Example M-1713-1.5S

Mechanical Specifications

Dimensions in inches (mm)

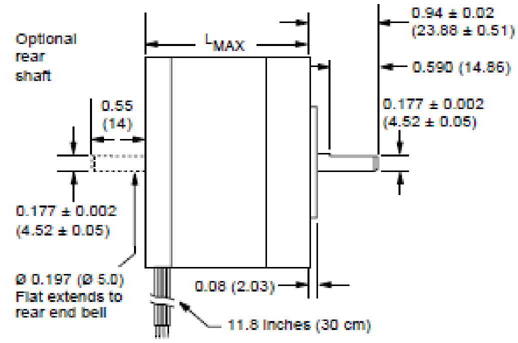

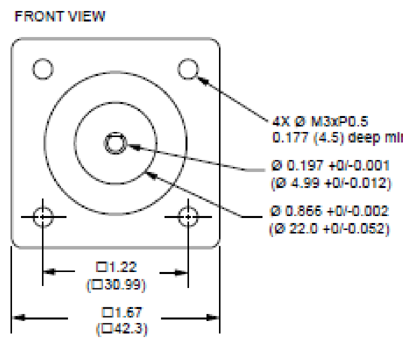

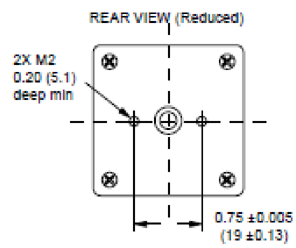

Motor stack length inches (mm)	Single	Double	Triple
LMAX	1.34 (34.0)	1.57 (40)	1.89 (48)

B.9 NEMA 23 stepper motor datasheet

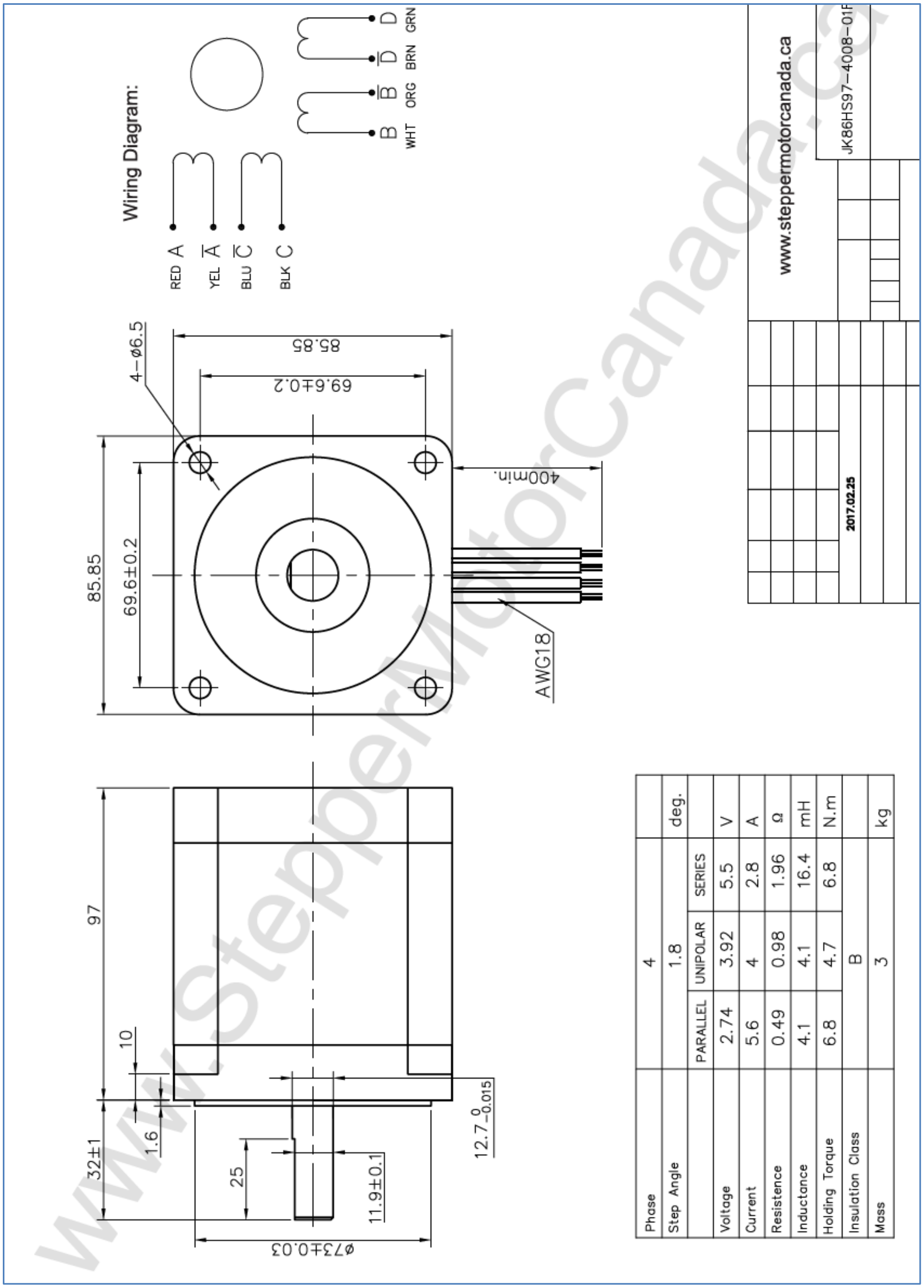

Phase	4			
Step Angle	1.8			deg.
	PARALLEL	UNIPOLAR	SERIES	
Voltage	2.74	3.92	5.5	V
Current	5.6	4	2.8	A
Resistence	0.49	0.98	1.96	Ω
Inductance	4.1	4.1	16.4	mH
Holding Torque	6.8	4.7	6.8	N.m
Insulation Class	B			
Mass	3			kg

B.10 Mechanical end stop switch datasheet

TECHNICAL SPECIFICATION

LED	Green
Power	5V
Signal pin V (no hit)	5V
Signal pin V (hit)	0V

MAJOR FEATURES

- Compatible with Megatronics v3.0, Minitronics v1.1 and RAMPS
- Small design that integrates easiliy into you printer
- High quality 2-layer PCB
- Long durable end stop

CONNECTORS

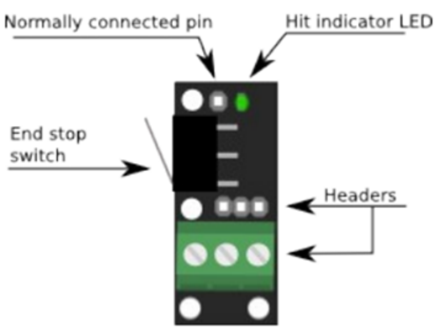

Name	**Description**
Headers	Headers (3 pin and screw terminal) to connect the end stop to the RepRap electronics. 1. S(ignal) 2. GND 3. 5V
NC	Normally connected pin (GND if endstop not hit, floating if hit)

BOARD DIMENSIONS

Dimensions: 16mmx40mmx15mm

List of M3 holes (measured from the bottom left):
2.5, 2.5
2.5, 17.5
2.5, 37.5
13.5, 2.5

B.11 Arduino Mega 2560 datasheet

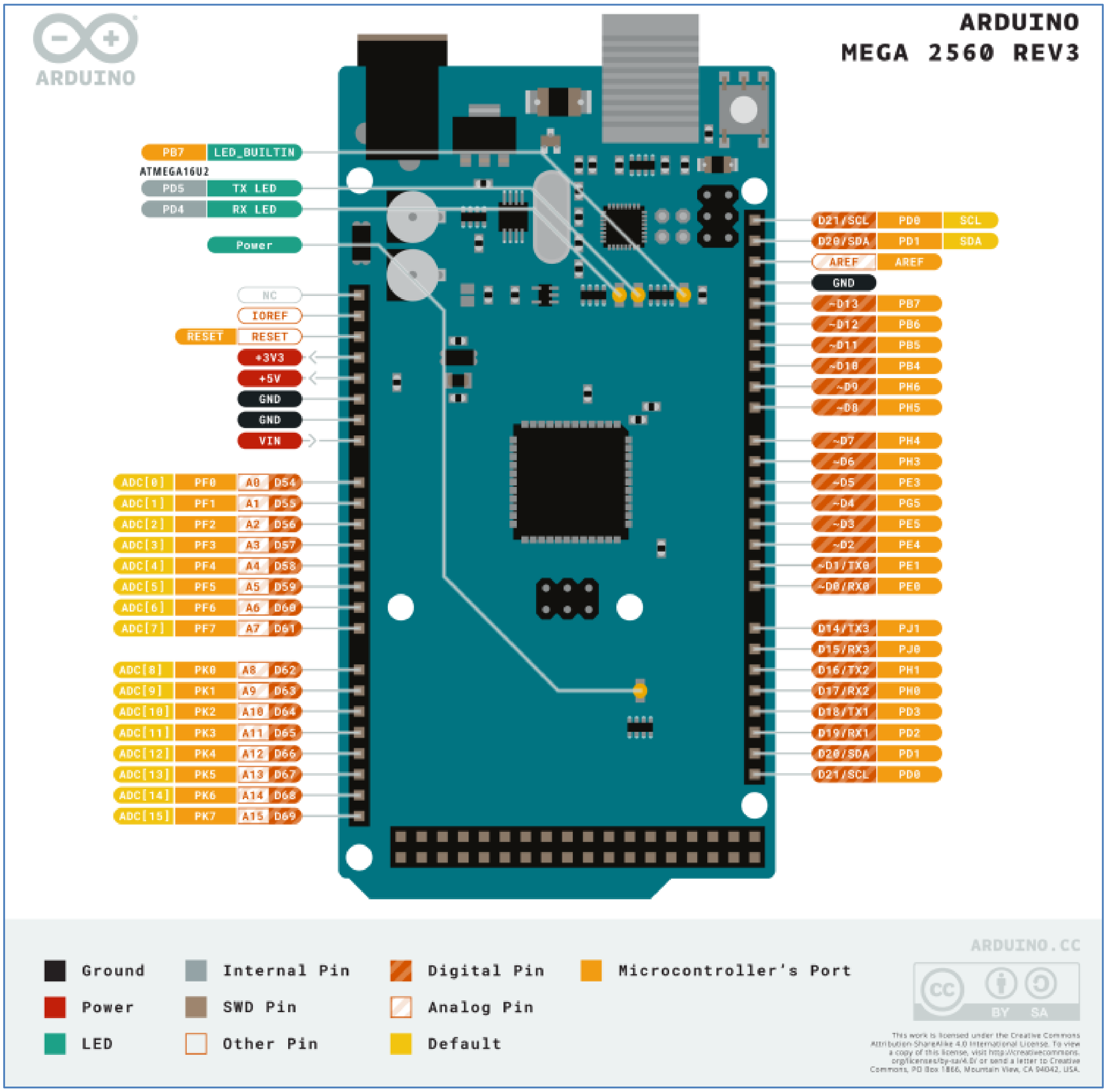

2.1 Recommended Operating Conditions

Symbol	Description	Min	Max
TOP	Operating temperature:	-40 °C	85 °C

2.2 Power Consumption

Symbol	Description	Min	Typ	Max	Unit
PWRIN	Input supply from power jack		TBC		mW
USB VCC	Input supply from USB		TBC		mW
VIN	Input from VIN pad		TBC		mW

B.12 RAMPS v1.4 datasheet

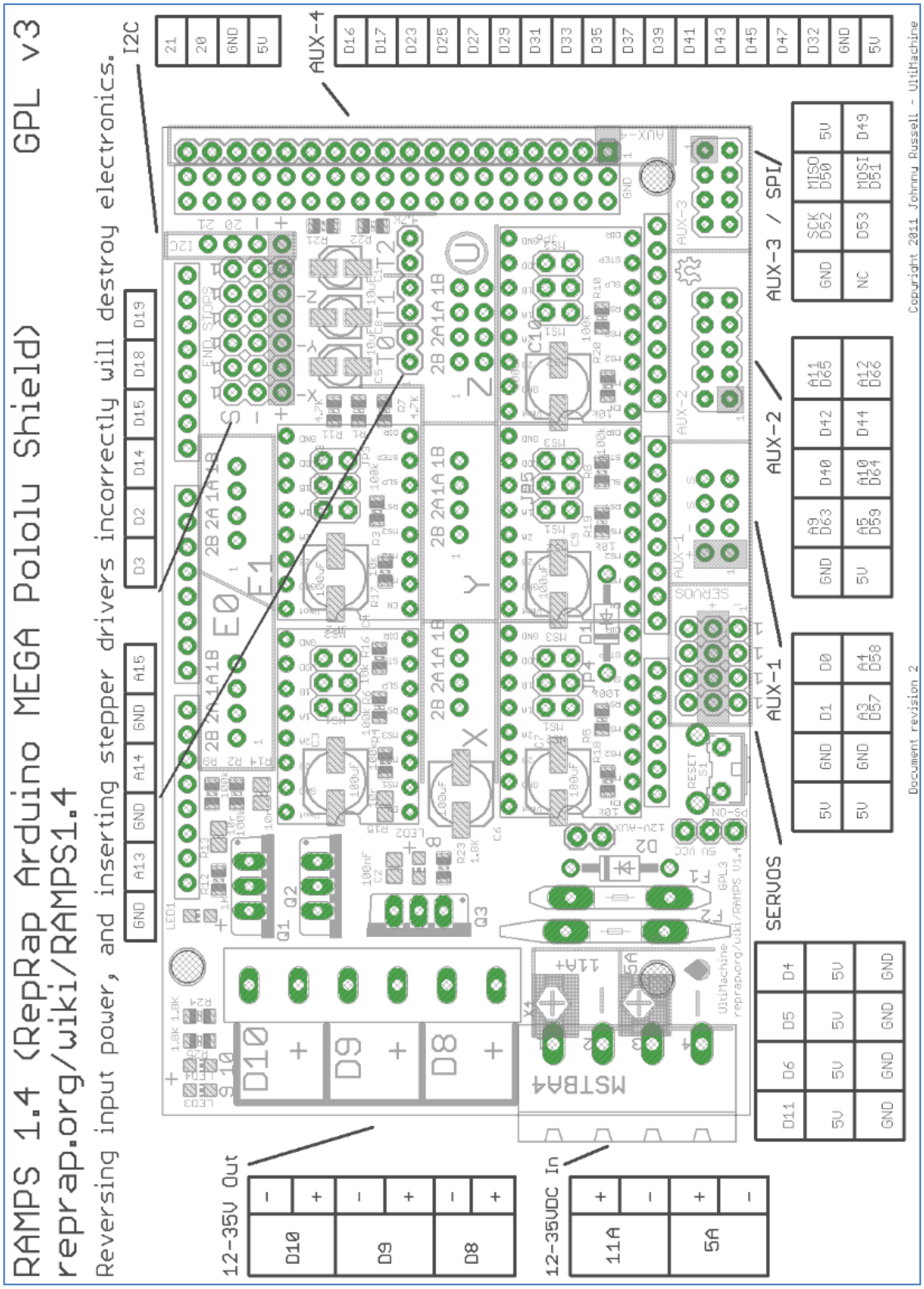

Appendix C : Frame production drawings

C.1 Frame manufacturing drawing

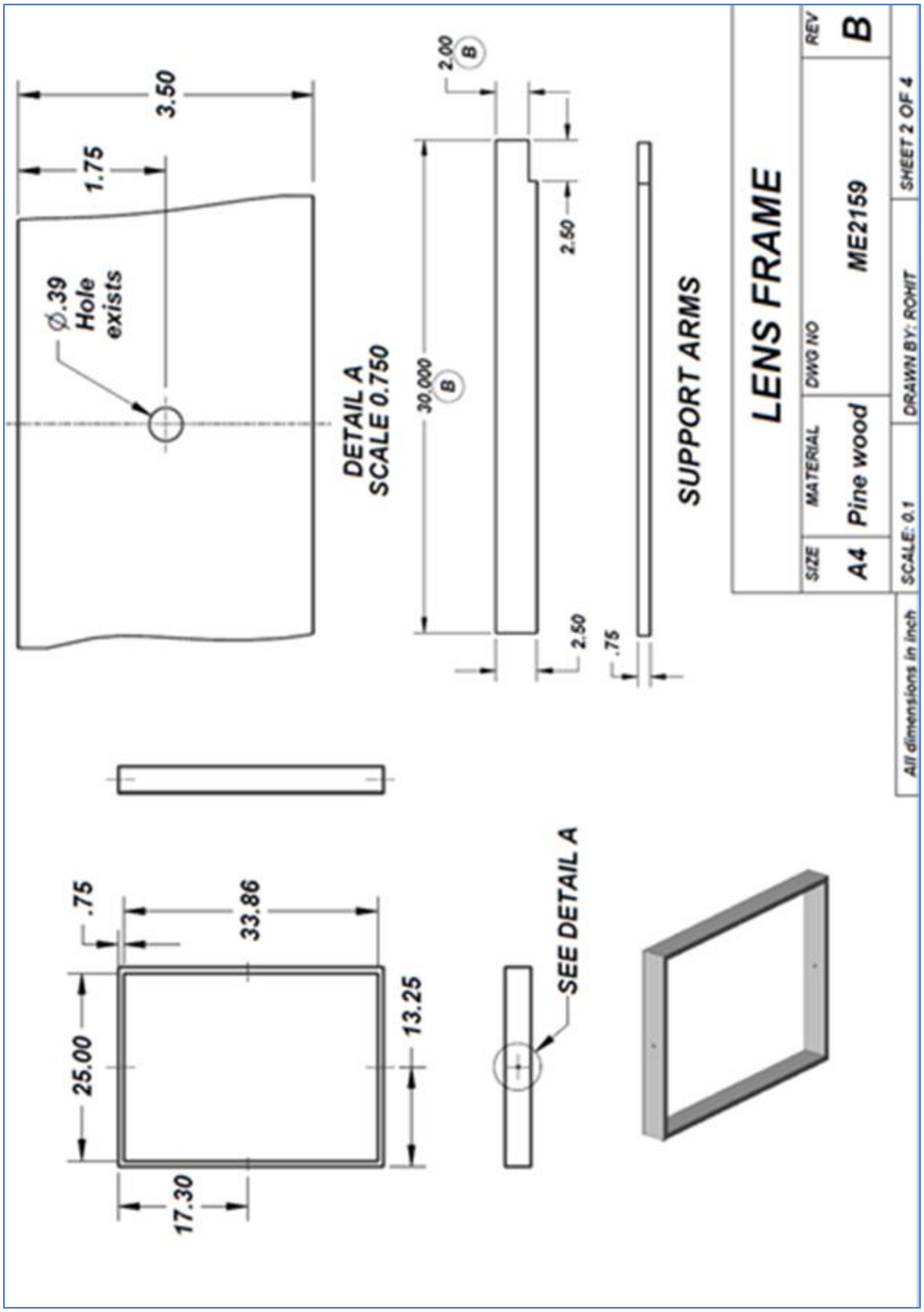

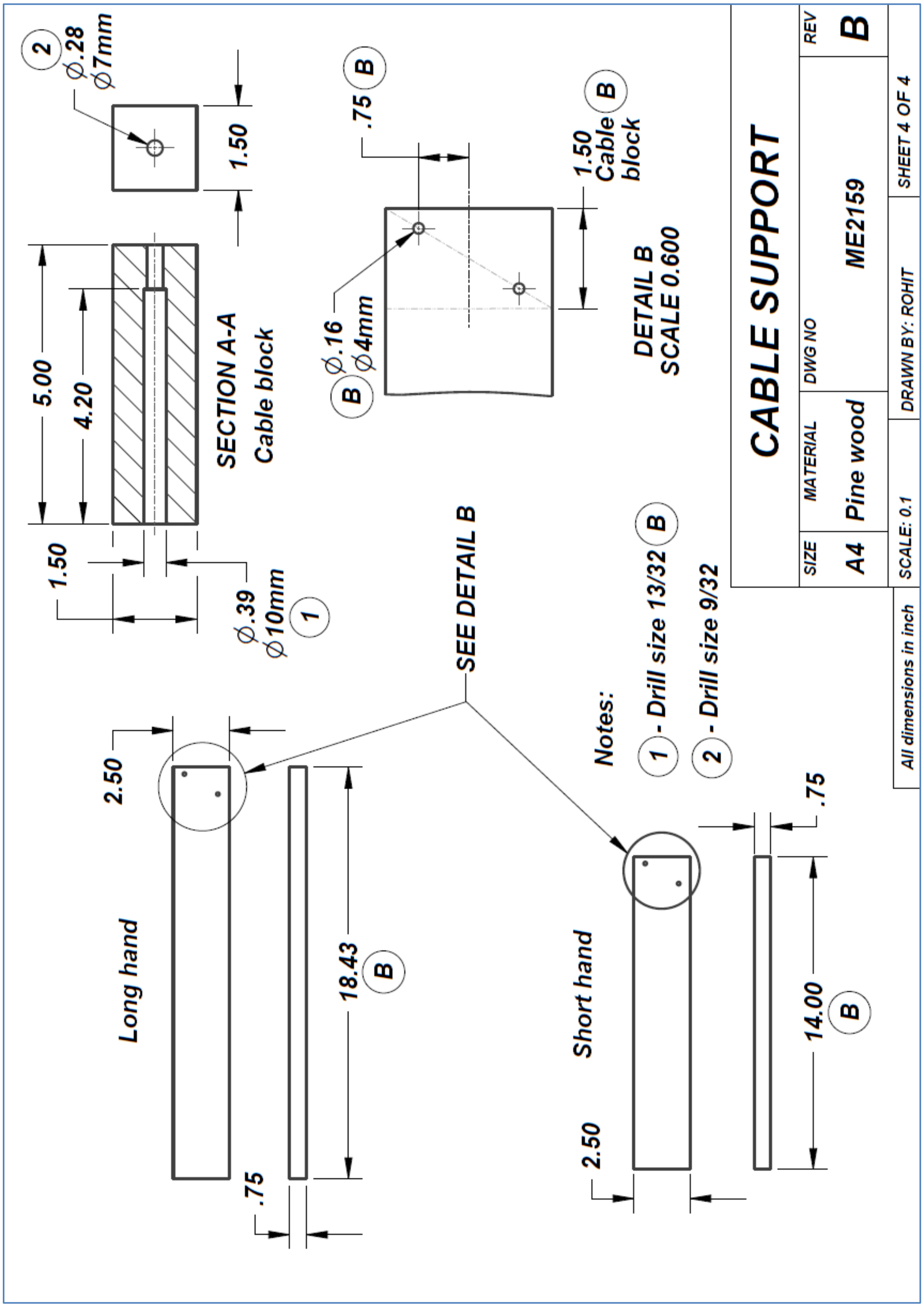
CABLE SUPPORT
SIZE A4
MATERIAL Pine wood
DWG NO ME2159
REV B
SCALE: 0.1
DRAWN BY: ROHIT
SHEET 4 OF 4
All dimensions in inch
SECTION A-A
Cable block
DETAIL B
SCALE 0.600
SEE DETAIL B
Long hand
Short hand
Notes:
1 - Drill size 13/32
2 - Drill size 9/32
Ø.39
Ø10mm
Ø.28
Ø7mm
Ø.16
Ø4mm
1.50 Cable block
5.00
4.20
1.50
.75
2.50
18.43
14.00

Appendix D : Optical fiber datasheets

D.1 Lumatec lightguide 380 series datasheet

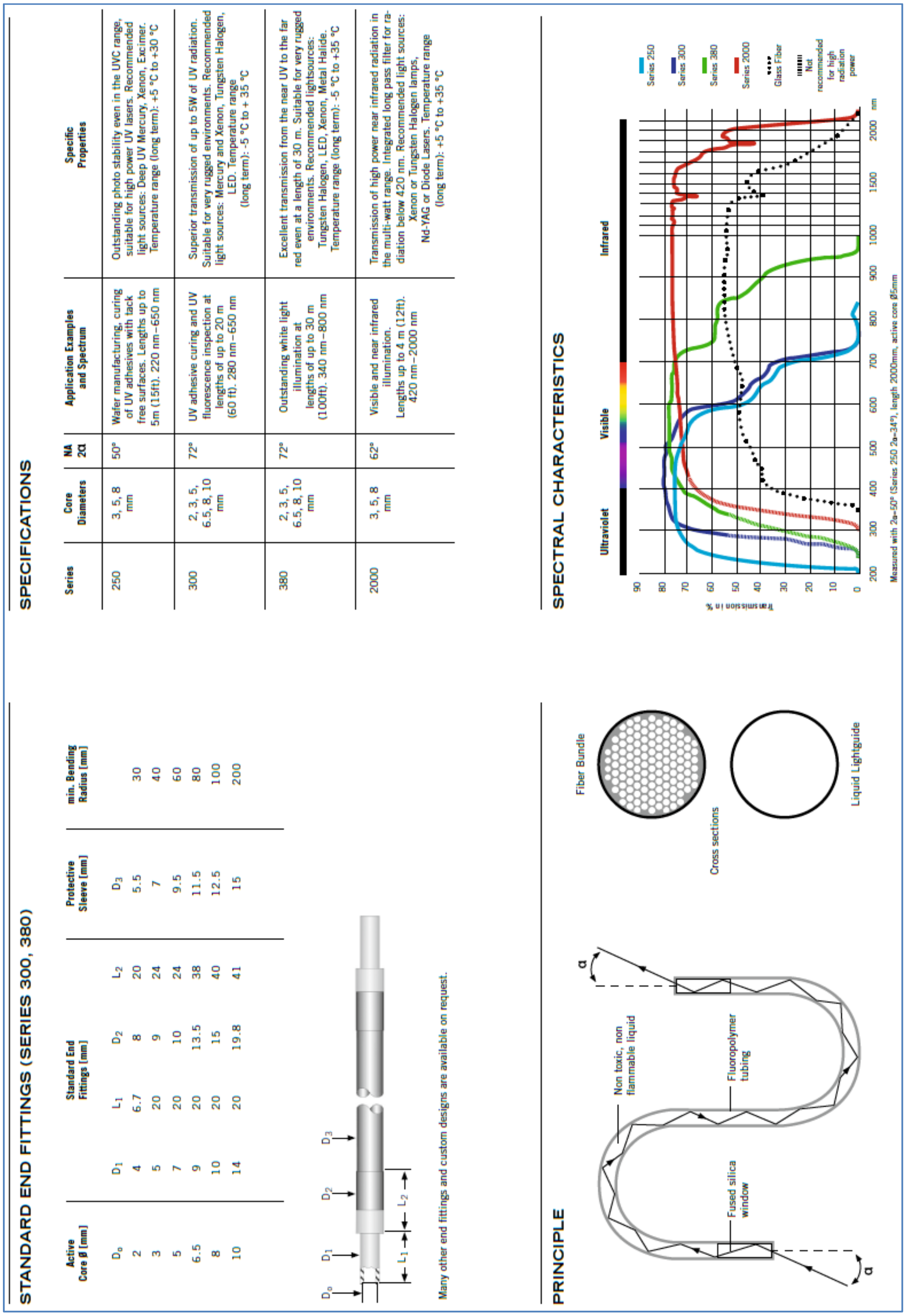

STANDARD END FITTINGS (SERIES 300, 380)

Active Core Ø [mm]	Standard End Fittings [mm]				Protective Sleeve [mm]	min. Bending Radius [mm]
D_o	D_1	L_1	D_2	L_2	D_3	
2	4	6.7	8	20	5.5	30
3	5	20	9	24	7	40
5	7	20	10	24	9.5	60
6.5	9	20	13.5	38	11.5	80
8	10	20	15	40	12.5	100
10	14	20	19.8	41	15	200

Many other end fittings and custom designs are available on request.

SPECIFICATIONS

Series	Core Diameters	NA 2α	Application Examples and Spectrum	Specific Properties
250	3, 5, 8 mm	50°	Wafer manufacturing, curing of UV adhesives with tack free surfaces. Lengths up to 5m (15ft). 220 nm–650 nm	Outstanding photo stability even in the UVC range, suitable for high power UV lasers. Recommended light sources: Deep UV Mercury, Xenon, Excimer. Temperature range (long term): +5 °C to +30 °C
300	2, 3, 5, 6.5, 8, 10 mm	72°	UV adhesive curing and UV fluorescence inspection at lengths of up to 20 m (60 ft). 280 nm–650 nm	Superior transmission of up to 5W of UV radiation. Suitable for very rugged environments. Recommended light sources: Mercury and Xenon, Tungsten Halogen, LED. Temperature range (long term): -5 °C to + 35 °C
380	2, 3, 5, 6.5, 8, 10 mm	72°	Outstanding white light illumination at lengths of up to 30 m (100ft). 340 nm–800 nm	Excellent transmission from the near UV to the far red even at a length of 30 m. Suitable for very rugged environments. Recommended lightsources: Tungsten Halogen, LED, Xenon, Metal Halide. Temperature range (long term): -5 °C to +35 °C
2000	3, 5, 8 mm	62°	Visible and near infrared illumination. Lengths up to 4 m (12ft). 420 nm–2000 nm	Transmission of high power near infrared radiation in the multi-watt range. Integrated long pass filter for radiation below 420 nm. Recommended light sources: Xenon or Tungsten Halogen lamps, Nd-YAG or Diode Lasers. Temperature range (long term): +5 °C to +35 °C

PRINCIPLE

SPECTRAL CHARACTERISTICS

Measured with 2α=50° (Series 250 2α=34°), length 2000mm, active core Ø5mm

D.2 Molex Polymicro JTFHL datasheet

molex

Low -OH Core
Hard Cladding
High NA

Polymicro SILICA/HARD POLYMER CLAD Optical Fiber JTFLH

CHARACTERISTICS

Step index

Numerical aperture: 0.37 ± 0.02

Low-OH core, PolyClad® hard polymer clad

Low-OH core for Vis-NIR transmission

Sterilizable and bio-compatible – USP class VI*

Standard buffer: Tefzel®

Custom buffer: Acrylate, Nylon, Hytrel®

Operating temperature: –65 to +140°C

0.48NA available with Tefzel®

High–OH and custom sizes available

Typical Attenuation

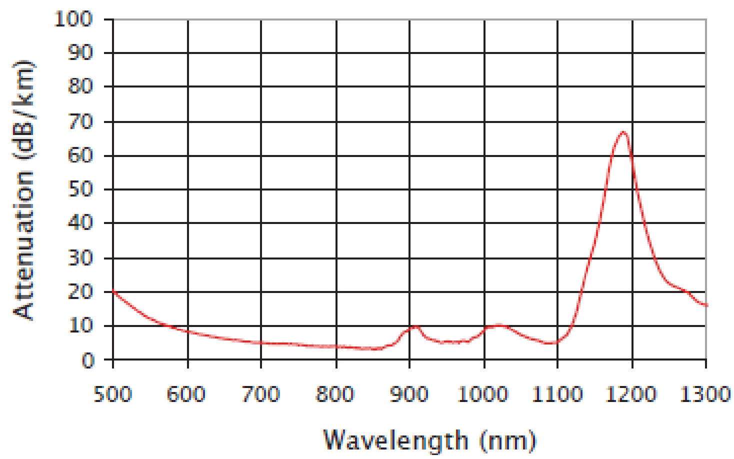

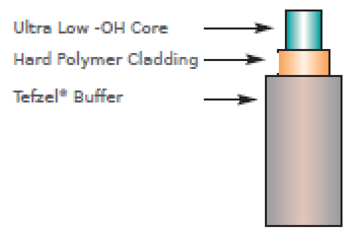

* The end manufacturer is responsible for bio-compatibility and sterilization testing and validation studies.
Tefzel® and Hytrel® are registered trademarks of DuPont Corporation.

Specifications

JTFLH – TEFZEL® BUFFER

Product Descriptor	Core (µm)	Clad (µm)	Buffer (µm)	Short-term Bend Radius (mm)	Long-term Bend Radius (mm)
JTFLH200230500	200 ± 4	230 +0/-10	500 ± 30	20	25
JTFLH300330650	300 ± 6	330 +5/-10	650 ± 30	30	35
JTFLH400430730	400 ± 8	430 +5/-10	730 ± 30	40	50
JTFLH6006301040	600 ± 10	630 +5/-10	1040 ± 30	50	75
JTFLH8008301040	800 ± 10	830 ± 10	1040 ± 30	75	100
JTFLH100010351400	1000 ± 15	1035 ± 15	1400 ± 50	90	120

Note: The items listed in this table are standard configurations and sizes. Other configurations may be available on request.

Bibliography or References

[1] A. Ellery, “Sustainable in-situ resource utilization on the moon,” *Planet. Space Sci.*, vol. 184, p. 104870, May 2020, doi: 10.1016/j.pss.2020.104870.

[2] G. Sanders, “Human Mission Architectures and Approaches and Concepts for Incorporating In Situ Resource Utilization (ISRU),” *Graduate Seminar Series – SSERVI CLASS*, Jan. 16, 2017. https://sciences.ucf.edu/class/wp-content/uploads/sites/23/2017/01/ISRU-Human-Mission-Architectures-and-ApproachesV1.pdf (accessed Oct. 17, 2022).

[3] G. B. Sanders, “NASA In-Situ Resource Utilization (ISRU) Capability Roadmap Final Report May 19, 2005,” p. 49, 2005.

[4] G. Heiken, D. Vaniman, and B. M. French, Eds., *Lunar sourcebook: a user’s guide to the moon*. Cambridge [England] ; New York: Cambridge University Press, 1991.

[5] I. Kuznetsov *et al.*, “Lunar Dust: Properties and Investigation Techniques,” *Sol. Syst. Res.*, vol. 51, pp. 611–622, Dec. 2017, doi: 10.1134/S0038094617070097.

[6] N. E. B. Zellner, “Lunar Impact Glasses: Probing the Moon’s Surface and Constraining its Impact History,” *J. Geophys. Res. Planets*, vol. 124, no. 11, pp. 2686–2702, Nov. 2019, doi: 10.1029/2019JE006050.

[7] G. J. Taylor, L. M. V. Martel, P. G. Lucey, J. J. Gillis-Davis, D. F. Blake, and P. Sarrazin, “Modal analyses of lunar soils by quantitative X-ray diffraction analysis,” *Geochim. Cosmochim. Acta*, vol. 266, pp. 17–28, Dec. 2019, doi: 10.1016/j.gca.2019.07.046.

[8] A.-L. Paul, S. M. Elardo, and R. Ferl, “Plants grown in Apollo lunar regolith present stress-associated transcriptomes that inform prospects for lunar exploration,” *Commun. Biol.*, vol. 5, no. 1, p. 382, Dec. 2022, doi: 10.1038/s42003-022-03334-8.

[9] W. D. Carrier, “Lunar soil grain size distribution,” *The Moon*, vol. 6, no. 3–4, pp. 250–263, 1973, doi: 10.1007/BF00562206.

[10] “The Chemical Composition of Lunar Soil | Some Meteorite Information | Washington University in St. Louis.” https://sites.wustl.edu/meteoritesite/items/the-chemical-composition-of-lunar-soil/#Si (accessed Nov. 21, 2022).

[11] J. J. Papike, S. B. Simon, and J. C. Laul, “The lunar regolith: Chemistry, mineralogy, and petrology,” *Rev. Geophys.*, vol. 20, no. 4, p. 761, 1982, doi: 10.1029/RG020i004p00761.

[12] S. B. Simon, J. J. Papike, and J. C. Laul, “The lunar regolith: comparative studies of the Apollo and Luna sites. Petrology of soils from Apollo 17, Luna 16, 20, and 24.,” *Lunar Planet. Sci. Conf. Proc.*, vol. 12, pp. 371–388, Jan. 1982.

[13] “Lunar Dust Composition; And the problems it could create,” *The Indian Wire*, Jun. 25, 2021. https://www.theindianwire.com/space/watch-the-dust-lunar-dust-is-next-big-thing-on-nasas-highest-minds-for-returning-to-moon-315856/ (accessed Nov. 21, 2022).

[14] “Lunar Geology: Minerals on the Moon,” Aug. 01, 2019. https://web.archive.org/web/20190801201700/https://www.permanent.com/lunar-geology-minerals.html (accessed Nov. 21, 2022).

[15] A. S. Kiran Kumar and A. Roy Chowdhury, “Terrain mapping camera for Chandrayaan-1,” *J. Earth Syst. Sci.*, vol. 114, no. 6, pp. 717–720, Dec. 2005, doi: 10.1007/BF02715955.

[16] “Moon Impact Probe.” https://web.archive.org/web/20120224055618/http://www.isro.gov.in/Chandrayaan/htmls/mip.htm (accessed Nov. 23, 2022).

[17] Y. Kumar, “The Moon Impact Probe on Chandrayaan-1,” *Curr. Sci.*, vol. 96, pp. 540–543, Feb. 2009.

[18] M. A. Guruprasad *et al.*, “First detection of surface water on the Moon by Chandrayaan-1’s Moon Mineralogy Mapper (M3),” *Science*, vol. 326, no. 5952, pp. 568–572, 2009.

[19] W. C. Feldman, S. Maurice, A. B. Binder, B. L. Barraclough, R. C. Elphic, and D. J. Lawrence, “Fluxes of Fast and Epithermal Neutrons from Lunar Prospector: Evidence for Water Ice at the Lunar Poles,” *Science*, vol. 281, no. 5382, pp. 1496–1500, Sep. 1998, doi: 10.1126/science.281.5382.1496.

[20] I. G. Mitrofanov *et al.*, “Lunar Exploration Neutron Detector for the NASA Lunar Reconnaissance Orbiter,” *Space Sci. Rev.*, vol. 150, no. 1–4, pp. 183–207, Jan. 2010, doi: 10.1007/s11214-009-9608-4.

[21] D. A. Paige *et al.*, “Diviner Lunar Radiometer Observations of Cold Traps in the Moon’s South Polar Region,” *Science*, vol. 330, no. 6003, pp. 479–482, Oct. 2010, doi: 10.1126/science.1187726.

[22] P. van Susante, “Exploration, Conveying, Mining Cycles and Mining Requirements,” p. 118.

[23] E. G. Kelly and D. J. Spottiswood, *Introduction to mineral processing*. New York: Wiley, 1982.

[24] R. Balasubramaniam, U. Hegde, and S. Gokoglu, “Determination of Chemical Kinetic Rate Constants of a Model for Carbothermal Processing of Lunar Regolith Simulant Using Methane,” in *47th AIAA Aerospace Sciences Meeting including The New Horizons Forum and Aerospace Exposition*, Orlando, Florida: American Institute of Aeronautics and Astronautics, Jan. 2009. doi: 10.2514/6.2009-1390.

[25] R. Balasubramaniam, S. Gokoglu, and U. Hegde, “The reduction of lunar regolith by carbothermal processing using methane,” *Int. J. Miner. Process.*, vol. 96, no. 1–4, pp. 54–61, Sep. 2010, doi: 10.1016/j.minpro.2010.06.001.

[26] D. McKay and C. Allen, “Hydrogen reduction of lunar materials for oxygen extraction on the moon,” in *34th Aerospace Sciences Meeting and Exhibit*, Reno,NV,U.S.A.: American Institute of Aeronautics and Astronautics, Jan. 1996. doi: 10.2514/6.1996-488.

[27] U. Hegde, R. Balasubramaniam, S. Gokoglu, and M. S. El-Genk, “Analysis of Thermal and Reaction Times for Hydrogen Reduction of Lunar Regolith,” in *AIP Conference Proceedings*, Albuquerque (New Mexico): AIP, 2008, pp. 195–202. doi: 10.1063/1.2844967.

[28] R. Gustafson, B. White, and M. Fidler, “Demonstrating Lunar Oxygen Production with the Carbothermal Regolith Reduction Process,” in *47th AIAA Aerospace Sciences Meeting including The New Horizons Forum and Aerospace Exposition*, Orlando, Florida: American Institute of Aeronautics and Astronautics, Jan. 2009. doi: 10.2514/6.2009-663.

[29] K. A. Lee, L. Oryshchyn, A. Paz, M. Reddington, and T. M. Simon, “The ROxygen Project: Outpost-Scale Lunar Oxygen Production System Development at Johnson Space Center,” *J. Aerosp. Eng.*, vol. 26, no. 1, pp. 67–73, Jan. 2013, doi: 10.1061/(ASCE)AS.1943-5525.0000230.

[30] L. Sibille *et al.*, “Recent Advances in Scale-Up Development of Molten Regolith Electrolysis for Oxygen Production in Support of a Lunar Base,” in *47th AIAA Aerospace Sciences Meeting including The New Horizons Forum and Aerospace Exposition*, Orlando, Florida: American Institute of Aeronautics and Astronautics, Jan. 2009. doi: 10.2514/6.2009-659.

[31] A. A. Ellery, P. Lowing, P. Wanjara, M. Kirby, I. Mellor, and G. Doughty, “FFC CAMBRIDGE PROCESS AND METALLIC 3D PRINTING FOR DEEP IN-SITU RESOURCE UTILISATION – A MATCH MADE ON THE MOON,” *Th Int. Astronaut. Congr.*.

[32] “Circumferential lunar utilities,” in *The Moon*, New York, NY: Praxis, 2007, pp. 117–129. doi: 10.1007/978-0-387-73982-3_7.

[33] A. Ellery, “Generating and storing power on the moon using in situ resources,” *Proc. Inst. Mech. Eng. Part G J. Aerosp. Eng.*, vol. 236, no. 6, pp. 1045–1063, May 2022, doi: 10.1177/09544100211029433.

[34] A. Ignatiev, A. Freundlich, M. Duke, and S. Rosenberg, “New Architecture for Space Solar Power Systems: Fabrication of Silicon Solar Cells Using In-Situ Resources.” Space Vacuum Epitaxy Center, University of Houston and NASA Commercial Space Center, Jun. 2000. [Online]. Available: http://www.niac.usra.edu/files/library/meetings/annual/jun00/433Ignatiev.pdf

[35] M. Khamooshi, H. Salati, F. Egelioglu, A. Hooshyar Faghiri, J. Tarabishi, and S. Babadi, "A Review of Solar Photovoltaic Concentrators," *Int. J. Photoenergy*, vol. 2014, pp. 1–17, 2014, doi: 10.1155/2014/958521.

[36] A. Antonini, M. Stefancich, J. Coventry, and A. Parretta, "Modelling of Compound Parabolic Concentrators for Photovoltaic Applications," *Int. J. Opt. Appl.*, vol. 3, no. 4, pp. 40–52, Aug. 2013, doi: 10.5923/j.optics.20130304.02.

[37] F. L. Lansing and J. Dorman, *High-efficiency solar concentrator*, vol. 1. 1980. Accessed: Nov. 22, 2022. [Online]. Available: https://ui.adsabs.harvard.edu/abs/1980seip.conf..392L

[38] F. J. DiSalvo, "Thermoelectric Cooling and Power Generation," *Science*, vol. 285, no. 5428, pp. 703–706, Jul. 1999, doi: 10.1126/science.285.5428.703.

[39] G. M. Gryaznov *et al.*, "Thermoemission reactor-converters for nuclear power units in outer space," *Sov. At. Energy*, vol. 66, no. 6, pp. 414–418, Jun. 1989, doi: 10.1007/BF01123508.

[40] T. Nakamura and C. L. Senior, "Solar Thermal Power for Lunar Materials Processing," *J. Aerosp. Eng.*, vol. 21, no. 2, pp. 91–101, 2008, doi: 10.1061/(ASCE)0893-1321(2008)21:2(91).

[41] T. Nakamura, B. K. Smith, and B. R. Irvin, "Optical Waveguide Solar Power System for Material Processing in Space," *J. Aerosp. Eng.*, vol. 28, no. 1, p. 04014051, Jan. 2015, doi: 10.1061/(ASCE)AS.1943-5525.0000294.

[42] Hintze Paul E. and Quintana Stephanie, "Building a Lunar or Martian Launch Pad with In Situ Materials: Recent Laboratory and Field Studies," *J. Aerosp. Eng.*, vol. 26, no. 1, pp. 134–142, Jan. 2013, doi: 10.1061/(ASCE)AS.1943-5525.0000205.

[43] T. Nakamura, J. A. Case, and C. L. Senior, “Optical Waveguide Solar Energy System for Lunar Materials Processing,” in *Engineering, Construction, and Operations in Space V*, Albuquerque, New Mexico, United States: American Society of Civil Engineers, Jul. 1996, pp. 783–790. doi: 10.1061/40177(207)106.

[44] “The Solar Sinter by Markus Kayser,” *Dezeen*, Jun. 28, 2011. https://www.dezeen.com/2011/06/28/the-solar-sinter-by-markus-kayser/ (accessed Dec. 01, 2022).

[45] “Solar Sinter,” *Kayser Works*. https://kayserworks.com/798817030644 (accessed Dec. 01, 2022).

[46] C. A. McLemore, B. Systems, and E. Edmunson, “IN SITU MANUFACTURING IS A NECESSARY PART OF ANY PLANETARY ARCHITECTURE. J.,” p. 2.

[47] M. Snyder, J. Dunn, and E. Gonzalez, “The Effects of Microgravity on Extrusion Based Additive Manufacturing,” in *AIAA SPACE 2013 Conference and Exposition*, San Diego, CA: American Institute of Aeronautics and Astronautics, Sep. 2013. doi: 10.2514/6.2013-5439.

[48] R. Jones *et al.*, “RepRap - the replicating rapid prototyper,” *Robotica*, vol. 29, pp. 177–191, Jan. 2011, doi: 10.1017/S026357471000069X.

[49] “What is SLA 3D printing?,” *Hubs*. https://www.hubs.com/knowledge-base/what-is-sla-3d-printing/ (accessed Nov. 23, 2022).

[50] S. Lekurwale, T. Karanwad, and S. Banerjee, “Selective laser sintering (SLS) of 3D printlets using a 3D printer comprised of IR/red-diode laser,” *Ann. 3D Print. Med.*, vol. 6, p. 100054, Jun. 2022, doi: 10.1016/j.stlm.2022.100054.

[51] "What is FDM (fused deposition modeling) 3D printing?," *Hubs*. https://www.hubs.com/knowledge-base/what-is-fdm-3d-printing/ (accessed Nov. 23, 2022).

[52] "All About Multi Jet Modeling (MJM) 3D Printing." https://www.thomasnet.com/articles/custom-manufacturing-fabricating/all-about-multi-jet-modeling-mjm-3d-printing/ (accessed Nov. 23, 2022).

[53] "The 7 categories of Additive Manufacturing | Additive Manufacturing Research Group | Loughborough University." https://www.lboro.ac.uk/research/amrg/about/the7categoriesofadditivemanufacturing/ (accessed Nov. 23, 2022).

[54] "History of Stratasys, Inc. – FundingUniverse." http://www.fundinguniverse.com/company-histories/stratasys-inc-history/ (accessed Nov. 23, 2022).

[55] M. Li and J. Liu, "Design of Cartesian-Style 3D Printer," in *2020 IEEE 3rd International Conference on Information Technology and Computer Application Engineering (ITCAE)*, 2020, pp. 185–189. doi: 10.1109/ITCAE49818.2020.9193973.

[56] P. Klein and J. Cooper, "The design and implementation of a delta-style 3D printer," *Int. J. Rapid Manuf.*, vol. 6, no. 3, pp. 166–185, 2016, doi: 10.1504/IJRAPIDM.2016.078235.

[57] J. Zhang, Y. Chen, Q. Wang, and C. Chen, "A Polar Coordinate Based G-Code Generation Method for Printing Spherical Objects with FDM 3D Printer," *J. Comput. Des. Eng.*, vol. 8, no. 2, pp. 198–206, 2021, doi: 10.1016/j.jcde.2020.09.002.

[58] P. Faulhaber, A. Herkommer, and D. Drummer, "Design and characterization of a CoreXY 3D-printer," *Procedia CIRP*, vol. 84, pp. 427–432, 2019, doi: 10.1016/j.procir.2019.02.037.

[59] Y. Xu, L. Feng, Y. Liu, and X. Lai, "Design and implementation of a 3D printing SCARA robot," in *2018 IEEE International Conference on Robotics and Biomimetics (ROBIO)*, 2018, pp. 516–521. doi: 10.1109/ROBIO.2018.8665038.

[60] "What is Fused Deposition Modeling (FDM), its uses and characteristics," *Engineering Product Design*. https://engineeringproductdesign.com/knowledge-base/fused-deposition-modeling/ (accessed Oct. 18, 2022).

[61] "All About Selective Laser Melting 3D Printing." https://www.thomasnet.com/articles/custom-manufacturing-fabricating/selective-laser-melting-3d-printing/ (accessed Oct. 18, 2022).

[62] D. Ratna, "Properties and processing of thermoset resin," in *Recent Advances and Applications of Thermoset Resins*, Elsevier, 2022, pp. 173–292. doi: 10.1016/B978-0-323-85664-5.00003-X.

[63] T. Prater, N. Werkheiser, F. Ledbetter, D. Timucin, K. Wheeler, and M. Snyder, "3D Printing in Zero G Technology Demonstration Mission: complete experimental results and summary of related material modeling efforts," *Int. J. Adv. Manuf. Technol.*, vol. 101, no. 1–4, pp. 391–417, Mar. 2019, doi: 10.1007/s00170-018-2827-7.

[64] "An experiment in 3D printing in zero gravity - Make Parts Fast." https://www.makepartsfast.com/an-experiment-in-3d-printing-in-zero-gravity/ (accessed Nov. 23, 2022).

[65] “Impression 3D pour l’espace - applications et avantages,” *Aniwaa*. https://www.aniwaa.fr/guide/imprimantes-3d/industrie-spatiale-et-impression-3d/ (accessed Oct. 18, 2022).

[66] M. I. Space, “Additive Manufacturing Facility: 3D Printing The Future in Space,” *Made In Space*, Mar. 20, 2019. https://medium.com/made-in-space/additive-manufacturing-facility-3d-printing-the-future-in-space-a800fccecdf3 (accessed Nov. 23, 2022).

[67] J. K. Gans *et al.*, “Development of the Additive Manufacturing Facility for the International Space Station,” in *50th International Conference on Environmental Systems*, 2019.

[68] N. Leach, Ed., *Digital cities*. in Architectural design Profile, no. 200 = 79,4 [d. Gesamtw.]. Chichester: Wiley, 2009.

[69] “Contour Crafting Corporation | Construction 3D Printing | California,” *CC Corp*. https://www.contourcrafting.com (accessed Jan. 09, 2023).

[70] G. Cesaretti, E. Dini, X. De Kestelier, V. Colla, and L. Pambaguian, “Building components for an outpost on the Lunar soil by means of a novel 3D printing technology,” *Acta Astronaut.*, vol. 93, pp. 430–450, Jan. 2014, doi: 10.1016/j.actaastro.2013.07.034.

[71] B. Khoshnevis and R. Dutton, “Innovative Rapid Prototyping Process Makes Large Sized, Smooth Surfaced Complex Shapes in a Wide Variety of Materials,” *Mater. Technol.*, vol. 13, no. 2, pp. 53–56, Jan. 1998, doi: 10.1080/10667857.1998.11752766.

[72] “Moon base.” https://d-shape.com/Prodotti/moon-base/ (accessed Jan. 09, 2023).

[73] K. M. Mekid and A. M. A. Haidar, “Stepper motor error analysis and correction techniques,” *IEEE Trans. Instrum. Meas.*, vol. 55, no. 3, pp. 1040–1046, 2006, doi: 10.1109/TIM.2006.874178.

[74] S. R. Singh and V. Verma, “Error Analysis of Stepper Motors in Positioning Applications,” in *2017 2nd International Conference on Computing and Communications Technologies (ICCCT)*, IEEE, 2017, pp. 178–182. doi: 10.1109/ICCCT2.2017.8358355.

[75] “Aluminum 6061 Filamet™ | Metal 3D Print,” *The Virtual Foundry*. https://shop.thevirtualfoundry.com/en-ca/products/aluminum-6061-filamet (accessed Apr. 20, 2023).

[76] D. A. Kring and G. Ryder, “Iron on the Moon: A Review,” *Planet. Space Sci.*, vol. 57, no. 5–6, pp. 548–564, 2009.

[77] P. Bland, N. Artemieva, G. Collins, W. Bottke, D. Bussey, and K. Joy, “Asteroids on the Moon: Projectile survival during low velocity impacts,” in *39th Lunar & Planetary Science Conference*, 2008.

[78] A. Ellery, “Leveraging in situ resources for lunar base construction,” *Can. J. Civ. Eng.*, vol. 49, no. 5, pp. 657–674, May 2022, doi: 10.1139/cjce-2021-0098.

[79] H. Nakajima, P. Dijkstra, and K. Loos, “The Recent Developments in Biobased Polymers toward General and Engineering Applications: Polymers that are Upgraded from Biodegradable Polymers, Analogous to Petroleum-Derived Polymers, and Newly Developed,” *Polymers*, vol. 9, no. 12, p. 523, Oct. 2017, doi: 10.3390/polym9100523.

[80] Y. Wang, W. Wang, Z. Zhang, L. Xu, and P. Li, “Study of the glass transition temperature and the mechanical properties of PET/modified silica nanocomposite by

molecular dynamics simulation," *Eur. Polym. J.*, vol. 75, pp. 36–45, Feb. 2016, doi: 10.1016/j.eurpolymj.2015.11.038.

[81] G. R. Lima, W. F. Monteiro, B. O. Toledo, R. A. Ligabue, and R. M. C. Santana, "Titanate Nanotubes Modified With Zinc and Its Application in Post-Consumer PET Depolymerization," *Macromol. Symp.*, vol. 383, no. 1, p. 1800008, Feb. 2019, doi: 10.1002/masy.201800008.

[82] Core3D, "Wiring 3D Printer RAMPS 1.4," *Instructables*. https://www.instructables.com/Wiring-3D-Printer-RAMPS-14/ (accessed Oct. 05, 2022).

[83] "Arduino Mega Tutorial - Pinout and Schematics. Mega 2560 Specifications," *Electronic Circuits and Diagrams-Electronic Projects and Design*, Feb. 08, 2018. https://www.circuitstoday.com/arduino-mega-pinout-schematics (accessed Oct. 05, 2022).

[84] "RAMPS 1.4 Connections." https://www.hta3d.com/en/blog/How-to-connect-ramps1.4 (accessed Oct. 05, 2022).

[85] "RAMPS 1.4 - RepRap." https://reprap.org/wiki/RAMPS_1.4 (accessed Oct. 06, 2022).

[86] "Arduino Integrated Development Environment (IDE) v1 | Arduino Documentation." https://docs.arduino.cc/software/ide-v1/tutorials/arduino-ide-v1-basics (accessed Oct. 06, 2022).

[87] jbrazio, "What is Marlin?," *Marlin Firmware*, Aug. 29, 2022. https://marlinfw.org/docs/basics/introduction.html (accessed Oct. 06, 2022).

[88] "Slic3r - About." https://slic3r.org/about/ (accessed Oct. 06, 2022).

[89] “Printrun: Pure Python 3d printing host software.” https://www.pronterface.com/ (accessed Oct. 06, 2022).

[90] “Fresnel lens,” *Wikipedia*. Aug. 01, 2022. Accessed: Oct. 06, 2022. [Online]. Available: https://en.wikipedia.org/w/index.php?title=Fresnel_lens&oldid=1101660743

[91] “Fresnel Lenses | Edmund Optics.” https://www.edmundoptics.com/f/fresnel-lenses/12434/ (accessed Oct. 06, 2022).

[92] “30" SPOT FRESNEL LENS.” https://greenpowerscience.com/FRESNELSHOP/white_fresnel_frame21x21.html (accessed Oct. 06, 2022).

[93] E. Hecht, *Optics*, 5th ed. Pearson Education Limited, 2017.

[94] F. Valdivieso-González, M. del Río-Vázquez, and C. Nájera-Rendón, “Design of a solar concentrator based on Fresnel lenses,” *Int. J. Photoenergy*, vol. 2013, 2013.

[95] J. C. Palais, *Fiber optic communications*, 5th ed. Upper Saddle River, N.J: Pearson/Prentice Hall, 2005.

[96] “Fiber-optic cable,” *Wikipedia*. Oct. 05, 2022. Accessed: Oct. 06, 2022. [Online]. Available: https://en.wikipedia.org/w/index.php?title=Fiber-optic_cable&oldid=1114283166

[97] M. Bahl, “Structured Light Fields in Optical Fibers,” 2019. doi: 10.5772/intechopen.85958.

[98] A. W. Snyder and J. D. Love, *Optical waveguide theory*. in Science paperbacks, no. 190. London ; New York: Chapman and Hall, 1983.

[99] M. Noman *et al.*, “An investigation of a solar cooker with parabolic trough concentrator,” *Case Stud. Therm. Eng.*, vol. 14, p. 100436, Sep. 2019, doi: 10.1016/j.csite.2019.100436.

[100] G. Keiser, *Optical Fiber Communications*, 4th ed. New York: McGraw-Hill Education, 2010.

[101] J. T. Schwartz, J. von Neumann, and A. W. Burks, “Theory of Self-Reproducing Automata,” *Math. Comput.*, vol. 21, no. 100, p. 745, Oct. 1967, doi: 10.2307/2005041.

[102] H. JACOBSON, “ON MODELS OF REPRODUCTION,” *Am. Sci.*, vol. 46, no. 3, pp. 255–284, 1958.

[103] P. Marchal, “John von Neumann: The Founding Father of Artificial Life,” *Artif. Life*, vol. 4, no. 3, pp. 229–235, Jul. 1998, doi: 10.1162/106454698568567.

[104] H. Böttiger and A. Rabenseifner, *Konrad Zuse: Erfinder, Unternehmer, Philosoph und Künstler*. Petersberg: Michael Imhof Verlag, 2011.

[105] K. E. Drexler, *Engines of creation: the coming era of nanotechnology*, 6. [print.]. in Anchor books. New York: Doubleday, 1990.

[106] R. A. Freitas and R. C. Merkle, *Kinematic self-replicating machines*. Georgetown, Tex: Landes Bioscience/Eurekah.com, 2004.

[107] J. G. Kemeny, “The Universal Constructor: *Theory of Self-Reproducing Automata* . John von Neumann. Edited by Arthur W. Burks. University of Illinois Press, Urbana, 1966. 408 pp., illus. $10.,” *Science*, vol. 157, no. 3785, pp. 180–180, Jul. 1967, doi: 10.1126/science.157.3785.180.a.

[108] J. A. Duffie and W. A. Beckman, *Solar Engineering of Thermal Processes: Duffie/Solar Engineering 4e*. Hoboken, NJ, USA: John Wiley & Sons, Inc., 2013. doi: 10.1002/9781118671603.

[109] F. M. White, *Fluid mechanics*, 7. ed. in McGraw-Hill Series in Mechanical Engineering. New York: McGraw-Hill, 2011.

[110] Y. A. Çengel and J. M. Cimbala, *Fluid mechanics: fundamentals and applications*, Third edition. New York: McGraw Hill, 2014.

[111] T. M. Hill, R. G. Wilhelm, and G. B. Hush, “Design of a fluid dispensing system,” in *Proceedings of the IEEE/RSJ International Conference on Intelligent Robots and Systems*, IEEE, 1997, pp. 975–980.

[112] M. Hoque, H. Kabir, and M. H. Jony, “DESIGN AND CONSTRUCTION OF A BOWDEN EXTRUDER FOR A FDM 3D PRINTER USES 1.75MM FILAMENT,” *Int. J. Tech. Res. Sci.*, vol. 3, no. VIII, Oct. 2018, doi: 10.30780/IJTRS.V3.I8.2018.010.